Low b-values Diffusion Weighted Imaging of the in vivo human heart

Stanislas Rapacchi

Low b-values Diffusion Weighted Imaging of the in vivo human heart

Dissertation for the degree of Philosophiæ Doctor

Stanislas RAPACCHI

2007-2010

Directed by:

- Pierre CROISILLE, MD PhD
- Denis GRENIER, PhD

With the collaboration of:

- Han WEN, PhD
- Vinay M. PAI, PhD

Using low diffusion-weighting values (b) DWI reduces DWI sensitivity to physiological motion but permits only the imaging of intravoxel incoherent motion (IVIM), which combines both water diffusion and perfusion. This work evaluates the context of low b-values DWI imaging of the human heart, proposes methodological contributions and then applies the developed techniques experimentally. Images acquisition is optimized on several parameters and an ideal time-window for robust cardiac triggering is defined. Eventual results of a dedicated acquisition strategy combined with image processing: PCATMIP-low b-values DWI, show significant improvements towards the application of cardiac DWI. Preliminary in vivo results encourage further clinical investigations and scientific developments.

JURY COMPOSITION:

Referees:	*David FIRMIN*	*PhD*
	Jacques FELBLINGER	*PhD*
	Jean-Nicolas DACHER	*MD, PhD*
Invited:	*Virginie CALLOT*	*PhD*
	Isabelle MAGNIN	*PhD*
	Yue-Min ZHU	*PhD*
Directors:	*Pierre CROISILLE*	*MD, PhD*
	Denis GRENIER	*PhD*

Table of Contents

Résumé

L'Imagerie par Résonance Magnétique pondérée en Diffusion (IRM-D) permet l'accès à l'information structurelle des tissus au travers de la lecture du mouvement brownien des molécules d'eau. Ses applications sont nombreuses en imagerie cérébrale, tant en milieu clinique qu'en recherche. Néanmoins le mouvement physiologique créé une perte de signal supplémentaire au cours de l'encodage de la diffusion. Cette perte de signal liée au mouvement limite les applications de l'IRM-D quant à l'imagerie cardiaque. L'utilisation de faibles valeurs de pondération (b) réduit cette sensibilité mais permet seulement l'imagerie du mouvement incohérent intra-voxel (IVIM) qui contient la circulation sanguine et la diffusion des molécules d'eau. L'imagerie IVIM possède pourtant de nombreuses applications en IRM de l'abdomen, depuis la caractérisation tissulaire à la quantification de la perfusion, mais reste inexplorée pour l'imagerie du cœur.

Mon travail de thèse correspond à l'évaluation des conditions d'application de l'IRM-D à faibles valeurs de b pour le cœur humain, afin de proposer des contributions méthodologiques et d'appliquer les techniques développées expérimentalement.

Nous avons identifié le mouvement cardiaque comme une des sources majeures de perte de signal. Bien que la mouvement global puisse être corrigé par un recalage non-rigide, la perte de signal induite par le mouvement perdure et empêche l'analyse précise par IRM-D du myocarde. L'étude de cette perte de signal chez un volontaire a fournit une fenêtre temporelle durable où le mouvement cardiaque est au minimum en diastole. Au sein de cette fenêtre optimale, la fluctuation de l'intensité atteste d'un mouvement variable résiduel. Une solution de répéter les acquisitions avec un déclenchement décalé dans le temps permet la capture des minimas du mouvement, c.-à-d. des maximas d'intensité en IRM-D. La projection du maximum d'intensité dans le temps (TMIP) permet ensuite de récupérer des images pondérées en diffusion avec un minimum de perte de signal lié au mouvement.

Nous avons développé et évalué différentes séquences d'acquisition combinées avec TMIP : la séquence d'imagerie écho-planaire classique par écho de spin (SE-EPI) peut être adaptée mais souffre du repliement d'image ; une séquence Carr-Purcell-Meiboom-Gill combinée avec une préparation d'encodage de diffusion est plus robuste aux distorsions spatiales mais des artefacts de bandes noires empêchent son applicabilité ; finalement une séquence double-SE-EPI compensant les courants de Foucault et pleinement optimisée produit des images IRM-D moins artefactées. Avec cette séquence,

l'IRM-D-TMIP permet la réduction significative de la perte de signal liée au mouvement pour l'imagerie cardiaque pondérée en diffusion. L'inconvénient avec TMIP vient de l'amplification du bruit positif d'intensité.

Afin de compenser cette sensibilité du TMIP, nous séparons le bruit d'intensité des fluctuations lentes liées au mouvement grâce à une nouvelle approche basée sur l'analyse en composantes principales (PCA). La décomposition préserve les détails anatomiques tout en augmentant les rapports signal et contraste-à-bruit (SNR, CNR). Avec l'IRM-D-PCATMIP, nous augmentons à la fois l'intensité finale et la qualité d'image (SNR) en théorie et expérimentalement. Les bénéfices ont été quantifiés en simulation avant d'être validés sur des volontaires. De plus la technique a montré des résultats reproductibles sur des patients post-infarctus aigue du myocarde, avec un contraste cohérent avec la position et l'étendue de la zone pathologique.

Contrairement à l'imagerie cérébrale, l'imagerie IRM-D par faibles valeurs de pondération in vivo doit être différentiée des analyses IRM-D *ex-vivo*. Ainsi l'IRM-D-PCATMIP offre une technique sans injection pour l'exploration du myocarde par imagerie IVIM. Les premiers résultats sont encourageants pour envisager l'application sur un model expérimental d'une maladie cardiovasculaire. Enfin l'accès à des valeurs plus élevées de b permettrait l'étude du modèle complet IVIM du cœur humain, afin de séparer et quantifier à la fois la perfusion et la diffusion au sein des tissus.

Abstract

Diffusion weighted magnetic resonance imaging (DW-MRI, or DWI) enables the access to the structural information of body tissues through the reading of water molecules Brownian motion. Its applications are many in brain imaging, from clinical practice to research. However physiological motion induces an additional signal-loss when diffusion encoding is applied. This motion-induced signal-loss limits greatly its applications in cardiac imaging. Using low diffusion-weighting values (*b*) DWI reduces this sensitivity but permits only the imaging of intravoxel incoherent motion (IVIM), which combines both water diffusion and perfusion. IVIM imaging has many applications in body MRI, from tissue characterization to perfusion quantification but remains unexplored for the imaging of the heart.

The purpose of this work was to evaluate the context of low *b*-values DWI imaging of the heart, propose methodological contributions and then apply the developed techniques experimentally.

We identified cardiac motion as one of the major sources of motion-induced signal loss. Although bulk motion can be corrected with a non-rigid registration algorithm, additional signal-loss remains uncorrected for and prevents accurate DWI of the myocardium. The study of diffusion-weighted signal-loss induced by cardiac motion in a volunteer provided a time-window when motion is at minimum in diastole. Within this optimal time-window, fluctuation of intensity attests of variable remaining physiological motion. A solution to repeat acquisition with shifted trigger-times ease the capture of motion amplitude minima, i.e. DWI-intensity maxima. Temporal maximum intensity projection (TMIP) finally retrieves diffusion weighted images of minimal motion-induced signal-loss.

We evaluated various attempts of sequence development with TMIP: usual spin-echo echo-planar imaging (se-EPI) sequence can be improved but suffers aliasing issues; a balanced steady-state free-precession (b-SSFP) combined with a diffusion preparation is more robust to spatial distortions but typical banding artifacts prevent its applicability; finally a state-of-the-art double-spin-echo EPI sequence produces less artifacted DWI results. With this sequence, TMIP-DWI proves to significantly reduce motion-induced signal-loss in the imaging of the myocardium. The drawback with TMIP comes from noise spikes that can easily be highlighted.

To compensate for TMIP noise sensitivity, we separated noise spikes from smooth fluctuation of intensity using a novel approach based on localized principal component analysis (PCA). The decomposition was made so as to preserve anatomical features while increasing signal and contrast to

noise ratios (SNR, CNR). With PCATMIP-DWI, both signal-intensity and SNR are increased theoretically and experimentally. Benefits were quantified in a simulation before being validated in volunteers. Additionally the technique showed reproducible results in a sample of acute myocardial infarction (AMI) patients, with a contrast matching the extent and location of the injured area.

Contrarily to brain imaging, *in vivo* low b-values DWI should be differentiated from *ex vivo* DWI pure diffusion measurements. Thus PCATMIP-DWI might provide an injection-free technique for exploring cardiac IVIM imaging. Early results encourage the exploration of PCATMIP-DWI in an experimental model of cardiac diseases. Moreover the access to higher *b* values would permit the study of the full IVIM model for the human heart that retrieves and separates both perfusion and diffusion information.

Keywords: diffusion weighted imaging (DWI); cardiac magnetic resonance (CMR); intravoxel incoherent motion (IVIM) imaging; temporal maximum intensity projection (TMIP); principal component analysis (PCA)

1. Introduction

The heart is a key organ in the human body. Cardiovascular diseases impact deeply the whole body, threatening all organs via the circulation system. Therefore cardiac imaging is a major discipline of radiology.

Magnetic resonance imaging (MRI) is a powerful mean to explore the human body non-invasively. Cardiac magnetic resonance (CMR) plays a major role in everyday patients' care by diagnosing, preventing and following cardiac diseases non-invasively and without radiations.

Diffusion weighted magnetic resonance imaging (DW-MRI, or DWI) enables the access to the structural information of body tissues through the reading of water molecules Brownian motion. Its applications are many in brain imaging, from clinical practice to research. However when physiological motion occurs during diffusion encoding, an additional signal loss appears that limits the accuracy of DWI and bias results. This motion-induced signal-loss limits greatly its applications in cardiac imaging. A solution to reduce this sensitivity is to use low diffusion-weighting values (*b*) DWI. But low *b*-values DWI permits only the imaging of intravoxel incoherent motion (IVIM), which combines both water diffusion and perfusion. IVIM imaging has many applications in body MRI, from tissue characterization to perfusion quantification but remains unexplored for the imaging of the heart.

My work has been to define the context of feasibility for low b-values cardiac DWI in order to propose methodological contributions that could improve the reliability of cardiac DWI and/or ease the application of DWI in vivo. The purpose was to work in tight collaboration with the application towards possible immediate results *in vivo*.

This dissertation presents first the basis of cardiac imaging, then focuses on MRI technique, and especially describes DW-MRI. Once theoretical knowledge is stated, the developments and achievements of my thesis are exposed with the care of concision and clarity.

1.1. Clinical cardiac imaging: today's challenges

Improving imaging of the heart is a necessity

The heart is one of the vital organs of the human body. Therefore its slightest defect might greatly impact the whole body health. Thus cardiac imaging is critical in diagnosis procedures and this topic is a subject of intense research and investments.

1.1.1. Major public health issues and common pathologies

Cardiovascular diseases are the leading cause of death worldwide, making it a major public health issue. Coronary heart disease was the world leading cause of death in 2004 with 7.2 millions of deaths, which represents 12.2% of overall deaths. Chronic cardiovascular diseases impacts particularly high-income countries. Ischemic cardiomyopathy alone, when oxygen supply to the heart is critically reduced, was responsible for 8% (~40 000 cases) of deaths in France in 2006, and all circulation diseases account for the second cause of death (28%) after tumors (30%){source: INSEE, CépiDc-Inserm }.

The increasing mortality rate related to cardiovascular death leads to growing interest and investments from governments in the topic. Major risks of cardiovascular disease come from new life style in wealthy countries and the same behavior in developing countries is becoming an important public health concern. Increased stress, too rich diet and reduced physical activity are reasons for increasing risk of heart failure and vascular pathology. Therefore investments go to both research and prevention, in order to improve health care as well as raise public awareness.

1.1.2. Cardiac imaging: purpose and techniques

Cardiac imaging stands as one of the top priorities towards improving health care, to provide **better and more accessible care to the numerous cardiovascular patients.** Cardiac imaging is required to provide accurate diagnosis as well as tools for treatments evaluation.

1.1.2.1. Diagnosis

Imaging is at the core of identification, diagnosis and follow-up for all major cardiovascular diseases today. While biomarkers enables the detection of abnormality and triggers disease suspicions, imaging

helps **pathology detection and treatment choice**. Accurate diagnosis helps to define treatments targets and guides chirurgical intervention.

Moreover imaging is a key to provide the follow-up to assess treatment efficiency. Subsequent treatment adjustments rely heavily on the radiologists' conclusion.

Finally imaging also helps in new treatments evaluation, particularly for the heart which is difficult to access and analyze *in vivo*.

1.1.2.2. Prognosis

Aging as well as long-term diseases such as diabetes and obesity can impact severely the vascular system, including the heart. The mechanisms behind the complications are not always well understood and certainly not easy to anticipate. Cardiac imaging has an important role of prognostic to play in the **detection and the prevention of such complications before trauma occurs**. Many other diseases or dangerous genetic background are potential sources of future trauma and require regular check-ups. Accurate assessment of the current state of the body health in its deep foundations, especially the heart and the circulatory system, is needed to develop an efficient prevention.

1.1.3. Techniques: advantages and limitations

Cardiac imaging is giving a lot of interests towards many different applications. However imaging the heart is difficult and encounters many limitations. Investigating the heart can be done through 4 main imaging techniques, each with its own advantages and drawbacks: **Positron emission Tomography (PET)**, very specific but suffers low resolution and exposes patients to radiations; **Ultrasounds**, easily accessible and non-invasive, but can image only a limited depth and with relative quality; **Cone-beam X-ray tomography (CT)**, which has a very good resolution but is difficulty specific and exposes patients to small radiations; **Magnetic Resonance Imaging (MRI)** which offers a good resolution and specificity totally non-invasively but suffers a limited accessibility, related to its important cost.

Magnetic resonance imaging (MRI) has several advantages such as being harmless and non-invasive and providing a wide range of information that enables the differentiations of many cardiac diseases. However MRI has the drawback of being expensive and is also one of the most complex medical imaging techniques actually used. Nuclear spins manipulation and subsequent signal detection works in the frequency space and a Fourier transform is needed to retrieve images spatial features. Therefore MRI development requires specific techniques implying combined state-of-the art mathematics and physics.

Although the first MR images were acquired 40 years ago, the complexity of an MR imaging acquisition process qualify it as a new imaging modality with a vast evolution potential and new breakthroughs are observed every year. The resolution and image quality is satisfactory although not as good as CT image quality. Finally MRI allows a wide variety of image contrasts that characterize tissues on variable basis so that many diagnosis can be performed (protons density, nuclear spins properties, etc) from a single MRI examination, with no harm for the patient. This access to different contrasts makes MR Imaging a technique of great potential in diagnosis for the cardiac muscle. Several contrast agents can also be employed in MRI: coated gadolinium (Gd) is the common one used to perform perfusion imaging but also ultra-small super-paramagnetic iron oxide (USPIO) are used as contrast agent in MRI. Gadolinium is coated because of its high toxicity if injected as is. Cardiac imaging benefits greatly from this contrast-enhanced imaging as it can determine the precise 3D localization and extent of an injury subsequent to a heart attack. Moreover MRI can access information from several nuclei. Common MRI is based on 1H resonance (water and organic tissues possess many ^{1}H), but ^{31}P MR spectroscopy (MRS) or ^{17}O MRI are also interesting nuclei since ^{31}P-MRS can measure myocardial adenosine triphosphate (ATP) and phosphocreatine (PCr) (Bottomley et Weiss 1998) and ^{17}O MRI might able the quantification of oxygen consumption (McCommis et al. 2010). Thus MRI might enable to quantify the physiological tissues cells activity.

Among all imaging techniques, the choice to use one over the others is made depending on their diagnosis potential regarding suspected pathology but advantages and drawbacks like cost and accessibility are also taken in consideration and sometimes prevent any choice at all. This work focuses on cardiac MRI since many techniques are being developed in this field and benefit each other from their innovations (Lustig, Donoho, et Pauly 2007). Cardiac MRI is indeed a hot topic that currently motivates researchers worldwide.

1.2. Heart physiology

1.2.1. Introduction

To better understand the problematic of this thesis work, some basic knowledge of the cardiac physiology might be useful. This part is designed only for the basic understanding of the cardiac structure and function and focuses on their implication in the application of diffusion weighted magnetic resonance imaging to study the cardiac muscle.

1.2.2. Role of the heart

It might be obvious to some, but the heart plays a major role in the body system by circulating the blood from the lungs to the organs and backwards. The function of the heart acts as a double pump, propelling the deoxygenated blood to the lungs, where it is re-oxygenated, and then propelling the oxygenated blood towards all organs and tissues in the body (including the heart itself).

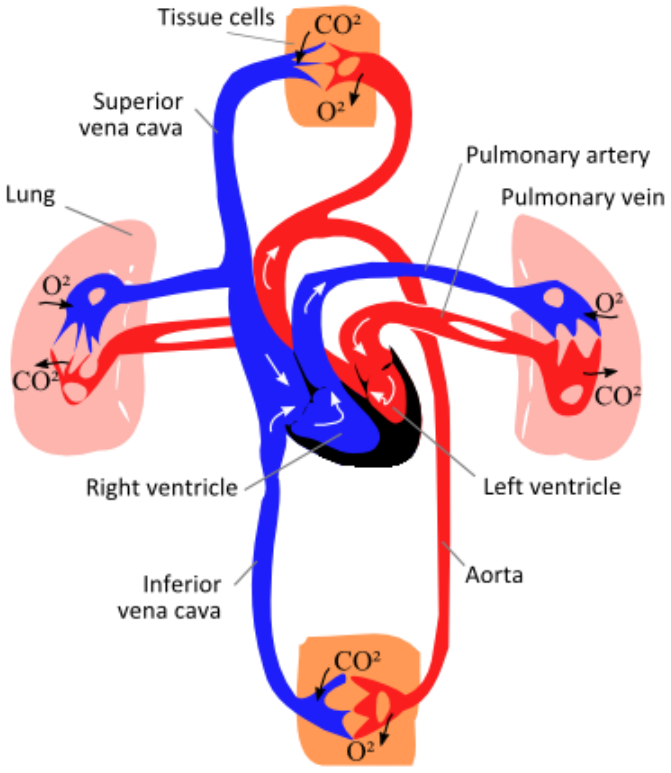

Figure 1: Blood circulatory system. The blood transports oxygen (in red) from the lungs, through the heart and to the body cells. Then the deoxygenated blood (blue) brings back carbon dioxide through the heart to the lungs to be expelled. Adapted from www.biosbcc.net .

1.2.3. Macroscopic heart anatomy

The human heart is about the size of a big fist and weights normally 250 to 350g. The heart functions as a double pump, decomposed in 4 cavities, with 4 valves separating each compartment:

- The atria: the right atria and the left atria, pre-chambers where flow is gathered
- The ventricles: the right ventricle and the left ventricle, where flow is propelled.

The two ventricles are separated by the septum wall. On each side, the valves function by pairs to open and close the entry and exit points of blood flow. When a chamber is full, the entry valve closes and the exit valve opens. When the chamber needs refill, the exit valve closes and the entry valve opens. The valves are controlled by the ventricles contraction through chordae tendineae (orange) taking roots in papillary muscles (small muscles in grey).

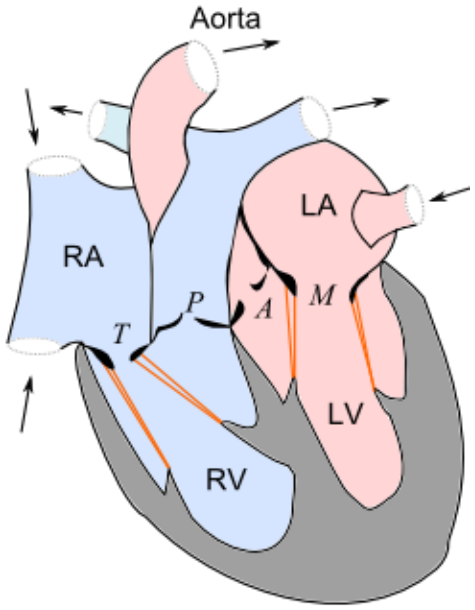

Figure 2: Heart anatomy focus. Abbreviations are: RA, right atria; LA, left atria; RV, right ventricle; LV left ventricle; T, tricuspid valve; P, pulmonic valve; A, aortic valve; M, mitral valve.

The two sides are very different as the right ventricle propels the deoxygenated blood to the lungs, very close to the heart and easy to access, while the left ventricle propels the oxygenated blood to all the organs, requiring a lot of strength. Therefore the left ventricle muscle is usually thicker than the right ventricle.

The heart muscle consists of a continuum (Streeter et al. 1970) that can be described with three adjacent layers: the epicardium, the thin outer layer (<1mm), the myocardium, the middle layer (~7-9mm) and the endocardium, the thin inner layer (<1mm).

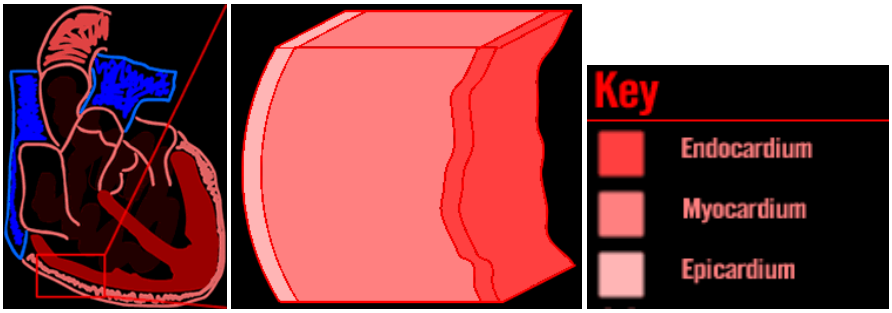

Figure 3: Heart wall muscles: from the exterior (epicardium) to the interior wall (endocardium). http://library.thinkquest.org/C003758/Structure/walls.htm

1.2.4. The cardiac cycle

The cardiac cycle can be decomposed in 4 steps. The focus is usually brought on the left ventricle, more critical than the right ventricle since it expels blood to the body, feeding the organs with oxygenated blood. But the two sides, the two ventricles function simultaneously.

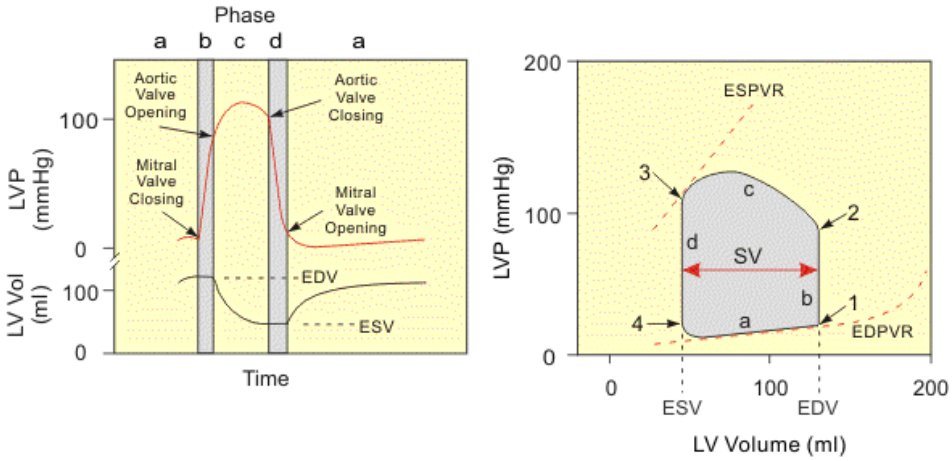

Figure 4: Cardiac cycle description. Reproduced from www.cvphysiology.com

The four basic cardiac phases are:

a. Ventricular filling. The mitral valve is open. The ventricle dilates to fill blood in. (diastole)
b. Isovolumetric contraction. The mitral valve closes, the aortic valve remains closed. The ventricle contracts to increase the pressure in the ventricle.

c. Ejection. The aortic valve opens. The blood is ejected through the aorta to the body organs.
d. Isovolumetric relaxation. The aortic valve closes. The myocardium relaxes the pressure in the ventricle.

The cardiac cycle is usually simplified in two parts: the systole, active part of the cycle, includes phases *b* to *d*, and the diastole, passive part, the phase *a* where the blood filling dilates the relaxed myocardium. The cycle is accessible through its electrical activity that surface electrodes can capture. The reference being the strong R-wave corresponding to the trigger of the myocardium contraction (phase *b*). Most cardiac studies use the R-wave as the reference of time.

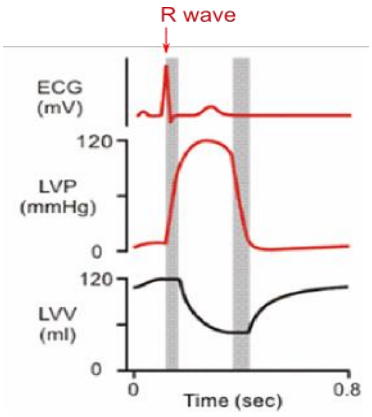

Figure 5: Electrocardiogram (ECG) and corresponding left ventricular pressure (LVP) and volume (LVV). Reproduced from www.cvphysiology.com

1.2.5. The myocardium microstructure

The cardiac muscle, the myocardium, is a very particular muscle in the human body that is a striated muscle as skeletal muscles, but involuntarily (contractile) as smooth muscles (e.g. autonomic nervous system of the eye).

There are three major types of cardiac cells (www.brown.edu):

- ***Cardiomyocytes*** - These are the cells that make up the *contractile* cardiac muscle. The cardiomyocytes are multinuclear such as cells in skeletal muscles (and contrarily to smooth muscles).
- *Vascular* ***endothelial*** *cells* - These cells are located in the inner lining of the heart blood vessels. They reduce turbulence of the flow of blood allowing the fluid to be pumped farther. They

regulate blood flow through vasoconstriction and vasodilation. They also act as a selective barrier that controls molecules transit through capillary membranes.

- ***Smooth muscle*** *cells* - These are located in the wall of the heart's blood vessels. They control the volume of blood vessels and the local blood pressure.

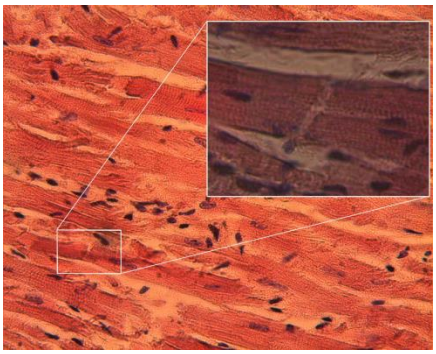

Figure 6: Histological section taken along the myocytes length. The fibrous arrays of myocytes with their multi-nucleus (dark spots) are seen. Reproduced from Wikipedia.org

The myocardium is composed of almost 80% of water, distributed among 3 main fluids compartments of interest appear (Bassingthwaighte, Yipintsoi, et Harvey 1974):

- **Intracellular** space, dense with cell activity, is where chemical reactions occur. Intracellular fluid makes up approximately 75-78% of myocardium water (Friedrich 2010) in healthy state. Intracellular water is tightly bound inside cells to proteins, ribonucleic acids and other molecules (see below for details).
- **Interstitial** space, part of ***extracellular*** space, is the space that carries all compounds between cells and the capillary system. Interstitial water accounts for 15-18% of myocardial water. Interstitial fluids are continually moving, being refreshed and recollected by lymphatic channels. Interstitial water moves slowly, driven by myocardial contraction and pressure gradients (mechanical pressure from intravascular space towards interstitium; osmotic pressure from K+/Na+ pump mechanisms to transit from intracellular space towards the venous system) (Mehlhorn et al. 2001).
- **Intravascular** space is the space inside the vascular circulatory system. Together with interstitial space, ***extracellular*** space makes up approximately 6-8 % of body water. Intravascular water is flowing at variable velocity (depending on the level of blood flow) and is slowly filtered through the endothelial barrier.

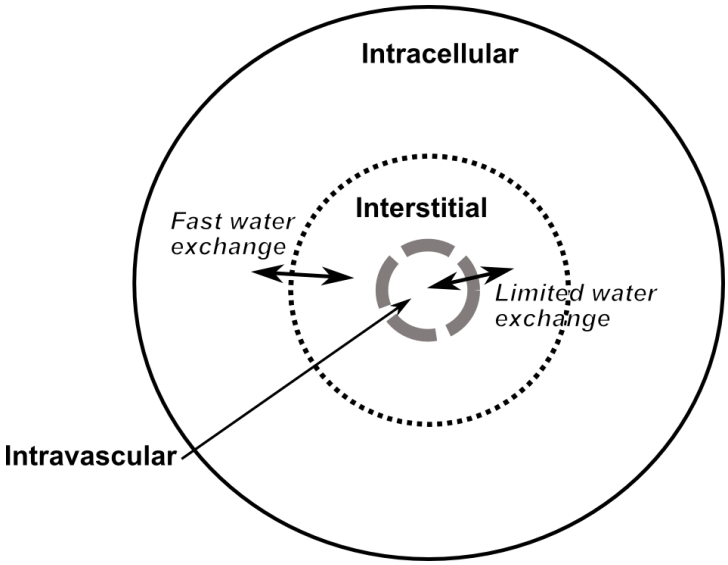

Figure 7: Model for water compartments in the myocardium. Intracellular space holds most of water in the myocardium and exchange easily water molecules with interstitial space in the healthy state. However water exchanges are limited through the endothelial barrier between interstitial space and intravascular space.(Judd, Reeder, et May-Newman 1999)

Water molecules move rapidly through myocytes membrane between interstitial space and intracellular space. Water transits through cell membrane via 3 main routes: (1) by diffusion, (2) coupled to ion-channels or substrate transporters, such as glucose, Na+, K+ and Ca+, (3) via aquaporins, proteins that enable selective rapid transit in response to osmotic gradients(Egan et al. 2006). Indeed like water, ions, proteins and molecules rapid exchanges in and out cells are required to supply metabolic mechanisms that provide for cellular function and energy (ATP). Among these mechanisms, ionic pumps (Na+, K+, Ca+ and H+) are critical to the control of metabolic regulation and osmotic gradients. As a part of this transit control, ionic pumps also regulate most of intracellular water content and water molecules displacements between intra and extracellular spaces.

Additionally intracellular water possesses a particular diffusion pattern in the myocardium since cardiomyocytes are elongated cells composed of bundled proteins filaments (Figure 8). Thus water molecules diffusion is tightly constrained spatially but in the longitudinal direction of myocytes. Additionally cardiomyocytes are well aligned to form fibers (myofibers), thus water moves preferably in one main direction that defines locally the microstructure of the myocardium.

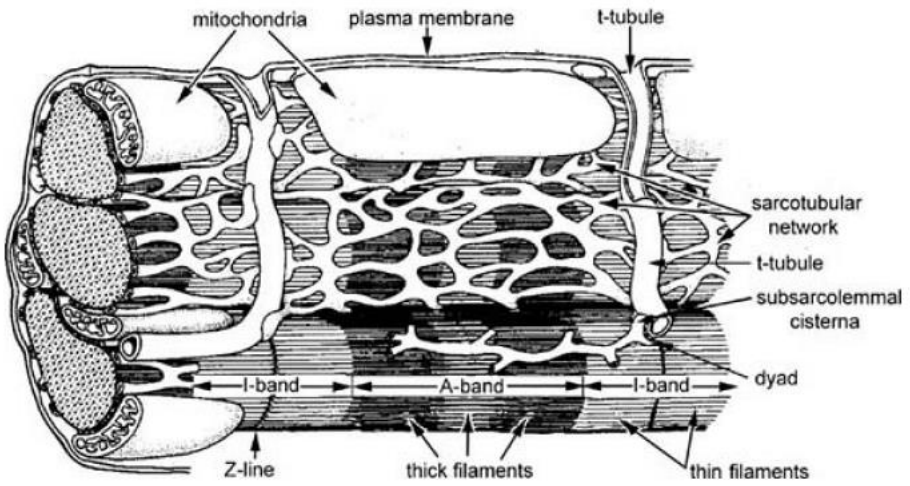

Figure 8: Ultrastructure of the working myocardial cell. Contractile proteins are arranged in a regular array of thick and thin filaments (seen in cross section at left). The A-band represents the region of the sarcomere occupied by the thick filaments, whereas the I-band is occupied only by thin filaments that extend toward the center of the sarcomere from the Z-lines, which bisect each I-band. The sarcomere, the functional unit of the contractile apparatus, is defined as the region between two Z-lines, and so contains two half I-bands and one A-band. The sarcoplasmic reticulum, an internal membrane system, consists of the sarcotubular network at the center of the sarcomere and the subsarcolemmal cisternae; the latter form composite structures with the transverse tubular system (t-tubules) and the sarcolemma called dyads. The t-tubular membrane is continuous with the sarcolemma, so that the lumen of the t-tubules carries the extracellular space toward the center of the myocardial cell. Mitochondria are shown in the central sarcomere and in cross section at the left.(Katz 2005; Topol et al. 2002)

Therefore intracellular and interstitial water molecules displacements occur locally along one main direction: the direction of myofibers. Additionally capillaries are aligned to this fibers structure, so that cardiac microcirculation follows the same direction (Callot et al. 2003). Consequently both diffusion and perfusion follows a pattern specific to the myocardium architecture (detailed further down in 1.2.7.). The displacement freedom of fluids within each compartment is a major parameter of tissue health. *Accessing the quantity of water molecules for each compartment and the microscopic motion of molecules (molecules diffusion and flow) is a critical mean to diagnosing tissues' health.*

1.2.6. The coronary flow mechanics (Rossi 2007)

The heart has a unique perfusion sequence. Because of the cardiac muscle contraction the vascular system is squeezed during systole. Thus contrarily to other organs, coronary perfusion mostly occurs during diastole.

Coronary blood flow is unique in the sense that it occurs on and into the heart which is alternately contracting and relaxing. Thus the phasic nature of blood flow into and through its muscular wall is a little different from other organs. As a consequence of that, in contrast to all other organs, coronary arterial blood flow occurs predominantly during diastole. **Coronary arterial blood flow at rest is low**

during systole, and then increases markedly in early diastole. Then it falls off in parallel with aortic pressure during mid-to-late diastole, and then falls abruptly during isometric ventricular contraction, prior to aortic valve opening. The reverse occurs with coronary venous blood flow which is high during systole and low during diastole. These cyclic changes are less marked in the right coronary arteries, supplying predominantly the right ventricle, but are very marked in the left coronary artery, which supplies the left ventricle.

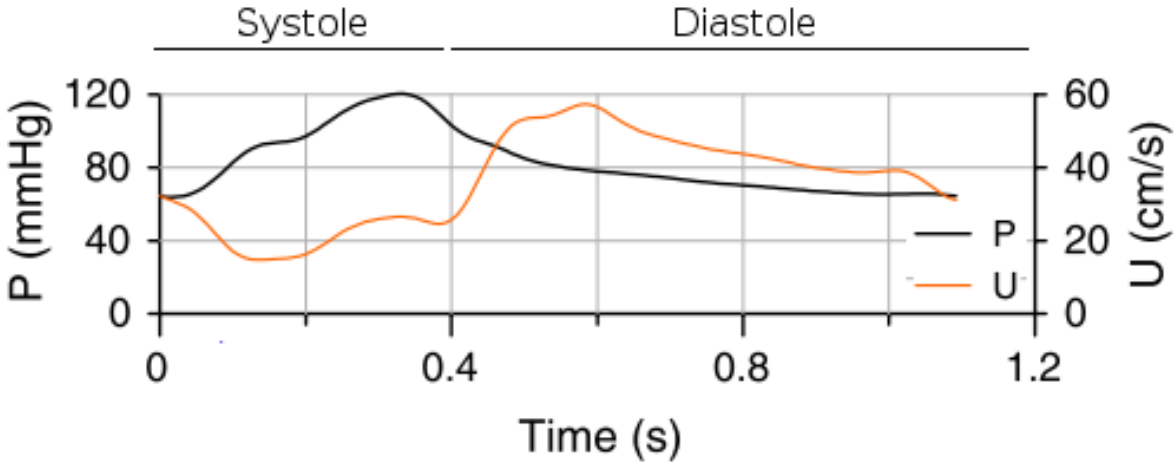

Figure 9: Left anterior descending coronary pressure (P) and blood flow velocity (U) for a healthy 62y.o. woman.(Siebes et al. 2009)

Therefore, although coronary perfusion is needed to sustain myocardial contraction, the latter seems to be an impeding factor for coronary perfusion. It is as if left ventricular contraction squeezes branches of the coronary arteries entering the myocardium so that nearly no flow can occur through these vessels during systole. The small amount of blood flowing into the left coronary artery during systole probably just dilates the epicardial branches of this artery (DOUGLAS et GREENFIELD 1970; Hoffman et Chilian 2000; F W Prinzen et al. 1985; Freeman et al. 1985). During diastole, squeezing ceases with myocardial relaxation and the coronary system of the left ventricle is perfused by the pressure gradient between origin – aorta, and exit – right atrium.

Additionally the myocardium requires a constant supply of oxygen to function. Whereas body muscles can sustain certain duration in anaerobic state, the myocardium cannot sustain local oxygen privation longer than 20-40 min without irreversible necrosis. Therefore compared to other organs, capillary density in myocardium is high (3-4 $.10^3$ capillaries per mm^2 cross section) and effective microvascular pore size is larger in myocardium (7-10 µm) (Mehlhorn et al. 2001).

1.2.7. The myocardium global architecture

As mentioned above, cardiac tissues are made of myocytes aligned into myofibers. The myofibers organize themselves into sheets. Global heart's architecture is positioned as a helix of muscle fibers that enhance the contraction mechanisms to increase the blood propeller-then-suction power. The fibers layers rotate across the myocardium wall with a progressive angle (from -90° to 90°(Wu et al. 2006)) to create the helix. In this configuration, the shortening of fibers amplifies the compression of the left ventricular cavity. This architecture is critical to the pump function of the heart. The alteration of this structure, such as in the process of remodeling after infarction (Wu et al. 2009; Streeter et al. 1970) can weaken the cardiac function.

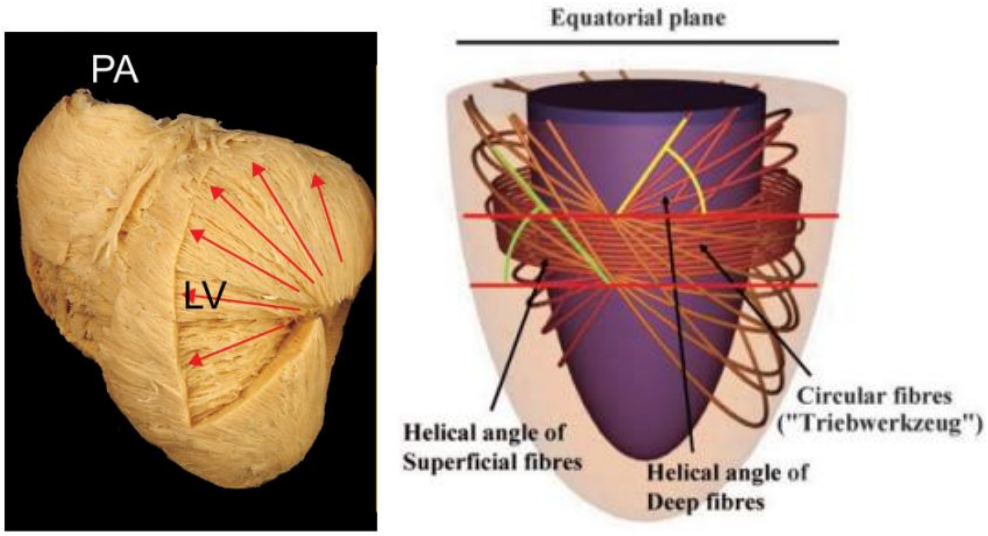

Figure 10: Fibers orientation in the heart. ***Left:*** *The myocardial "grain" as seen at various depths through the left ventricular wall of the porcine heart, visualized by peeling aggregates of myocytes stepwise in planes intruding from the epicardium to the endocardium. Note the turn of the grain upon a radial axis (red arrows). PA shows the origin of the pulmonary trunk from the right ventricle. LV, left ventricle.* ***Right:*** *the cartoon shows the variation in angle of the long axis of the myocytes aggregates when assessed relative to the ventricular equator. This is the so-called* ***helical angle****.(Anderson et al. 2006)*

Conclusion

Overall the cardiac muscle possesses a complex architecture and a unique functional behavior among body organs. The heart function is critical to other organs. Consequently cardiac diseases deeply affect their viability. The prevention as well as the diagnosis of cardiovascular pathologies is a topic of intense research, especially throughout developments of cardiac imaging.

1.3. MRI

Quantum physics - harmless body tissues exploration

Here is proposed a brief overview of nuclear magnetic resonance (NMR) with the classic model in order for the reader to reach faster the core of this thesis contribution. The author does realize the limitations of this model and is aware of risky but necessary shortcuts made in the following text, and asks talented quantum physics experts' forgiveness in order for them to focus on his accomplishments.

1.3.1. NMR principles

Nuclear Magnetic Resonance (NMR) is based on the interaction between an exterior magnetic field and particles' nuclear spins. Spin is a quantum fundamental property of particles. It can be represented as equivalent to an inner rotating magnetic momentum, and is determined by 2 parameters: its spin quantum number s (as every fundamental property, it is discrete: s=0,±1/2, ±1) and its direction described by a vector.

- Electrons, neutrons and protons (^{1}H) have a spin s=1/2
- Photons have a spin s=1

Proton NMR: basis

Let us now consider 1H atoms, with s=1/2 corresponding spin. An externally applied magnetic field **Bo** applied to a proton population will have 2 effects:

1. Their spins will start oscillating around the field axis at a pulsation proportional to the field strength: **ω**=γ**Bo**. This is the **Larmor precession**.

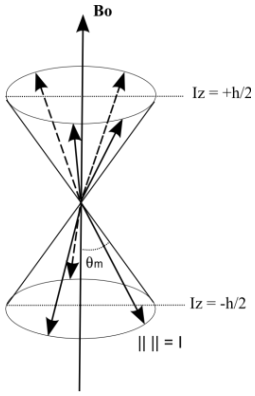

It is possible to show the rotation is limited to a cone, with a given cone angle $\theta_m \approx 54.74°$.

2. Their energy levels split. This is the Zeeman effect (Zeeman 1897).

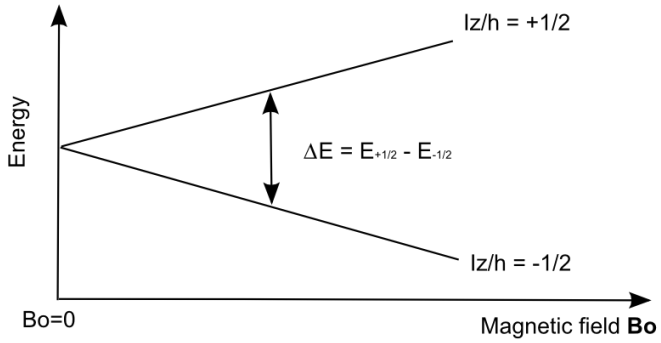

The splitting occurs because of the interaction of the magnetic moment **μ** of the atom with the magnetic field **B** slightly shifts the energy of the atomic levels by an amount:

$$\delta E = -\mu.\boldsymbol{B} \qquad \text{(I.)}$$

This energy shift depends on the relative orientation of the magnetic moment and the magnetic field{Physics 387 Home Page}. The magnetic momentum of the proton is:

$$\mu = g\frac{e.\boldsymbol{I}}{2m} = \gamma \boldsymbol{I} \qquad \text{(II.)}$$

Given the proton's charge e and its mass m. *g* is a dimensionless factor(the *g*-factor), $g_H \approx 5.586$. And γ is the gyromagnetic ratio, characteristic for each nuclide ($\gamma\!\!\!^{-}$= γ/2π=42.577 MHz/T for ^{1}H). Resulting energy shift is given as:

$$\delta E = \pm \mu_z B_o = \pm g \frac{e.\hbar}{4m}.B_o = \pm \gamma s \hbar B_o = \pm \hbar s v \quad \text{(III.)}$$

The energy gap between the two population is then ΔE=-2δE=-hɣB=-hv, with v corresponding frequency. The difference in populations between those two energy levels can be expressed with the Boltzmann statistics, with a naturally larger population for the lower energy level (thus the minus in the formula above):

$$a = \frac{N+}{N-} = e^{-\frac{\Delta E}{kT}} \quad \text{(IV.)}$$

Considering protons in a human body (T=37°C) within a clinical magnetic resonance imaging magnet of B=1.5T, we obtain v=63.87 MHz and a=1.000009882611, that is a difference of n=(a-1)/(a+1)=4.94ppm(part-per-million), which is a really small difference!

Because of this very small spins population difference, **NMR signal is usually very weak** and a strong magnetic field is required in order to capture a significant signal.

Also since the human body is composed of a lot of water, and water molecules possess two protons (H_2O), **nuclear magnetic resonance of the proton is the most effective non-invasive NMR method to study body tissues**.

Am I hearing resonance?

It is possible to make spins "hop" between populations by applying an electromagnetic radiofrequency (RF) pulse of the same energy as the gap between the two energy levels. The system will absorb the RF pulse energy, perturbing its equilibrium state, then it will return progressively to its initial state while restituting part of the given energy. This is the nuclear magnetic resonance (NMR).

In order to match corresponding energy difference, the RF pulse is calibrated on a frequency basis with the **Larmor frequency** connecting energy and frequency: $v_o = \omega_o/2\pi = -\gamma B$, as seen above.

Macroscopic magnetic momentum

The two levels of energy can be represented (quantum probabilities apart) with the spins: the lower level corresponds to spins z-components aligned parallel to the external magnetic field while the higher level corresponds to spins aligned anti-parallel to the external field.

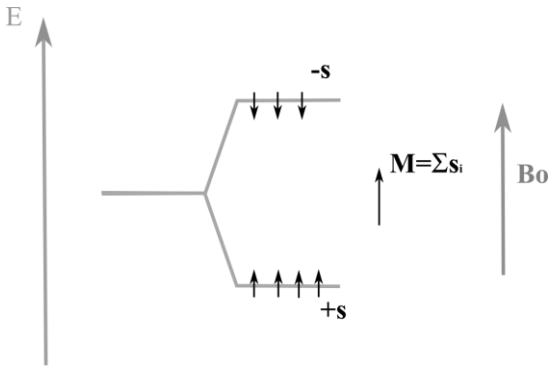

*Figure 11: The difference in spins populations creates a macroscopic magnetic momentum **M**.*

In a static external magnetic field **Bo**, a resulting magnetic moment **M** is created by the sum of unbalanced spin momentum, align parallel to the magnetic field. Applying RF pulses will enable the manipulation of this magnetic momentum **M**, from flipping it into transverse plane relative to static **Bo**, to flipping it entirely along the longitudinal axis(=**Bo** axis).

*NMR corresponds to the excitation-relaxation-reception of the magnetization **M** with varying parameters that enables the characterization of the sample.*

1.3.2. NMR experiment

As seen previously, the excitation RF pulse is a variable electromagnetic field $\mathbf{B_1}$ rotating around the **Bo** axis at the Larmor pulsation $\boldsymbol{\omega_o}$. Considering the frame turning with the spins at $\boldsymbol{\omega_o}$, the Larmor pulsation, the RF pulse can be represented as an additional fixed magnetic field $\mathbf{B_1}$ in a classic mechanic model. Applying this field in the transverse plane, here on x-axis, creates a torque **T** on **M** according to the Laplace force:

$$\boldsymbol{T} = \boldsymbol{M} \times \boldsymbol{B_1} = \frac{1}{\gamma}\frac{\mathrm{d}\boldsymbol{M}}{\mathrm{dt}} \rightarrow \frac{\mathrm{d}\boldsymbol{M}}{\mathrm{dt}} = \boldsymbol{M} \times \gamma \boldsymbol{B_1} \qquad \text{(V.)}$$

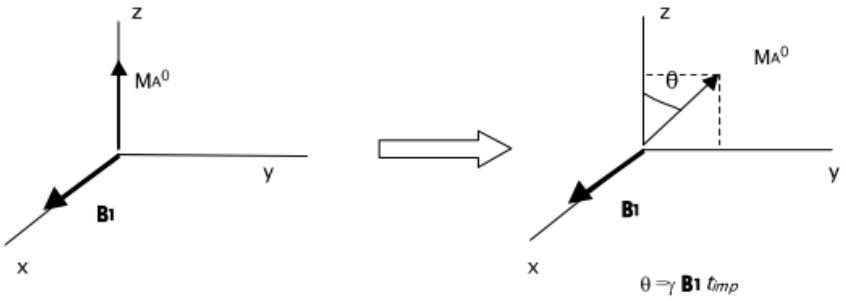

Figure 12: Rotation of macroscopic magnetization subject to a local radio-frequency variable electromagnetic field ***B₁****.*

The RF pulse leads to the rotation of the **M** vector around $\mathbf{B_1}$ axis (x-axis) with a speed equal to $\boldsymbol{\omega_1}=\gamma\mathbf{B_1}$. Eventual rotation angle is $\theta = \int^{timp} \gamma B_1(t)dt$ given t_{imp} the RF impulsion time. NMR RF pulses are usually characterized by this rotation angle θ, ranging from 0 to 180°(full flip of magnetization **M**), with common value at 90°(flip of **M** into the transverse plane,then Mz=0).

At resonance, the magnetization simply rotates around $\mathbf{B_1}$ in the rotating frame of reference, while in the laboratory frame the motion of **M** is a spiral (*nutation*) caused by the precession around the vector sum of $\mathbf{B_0}$ and $\mathbf{B_1}$(t).

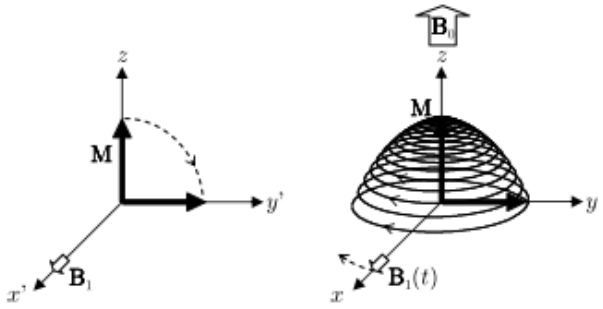

Figure 13: Excitation (left) and relaxation (Right) of the macroscopic magnetization. The relaxation occurs in a spiral trajectory that rotates (=nutation) around the intense static field ***Bo****.*

Relaxation of the magnetization (Absil 2006)

After being excited, the spins system returns to its thermal equilibrium state in the field **Bo**, this is the spin-latice relaxation (T_1). The magnetization during relaxation is ruled by the Bloch equations (Bloch 1946). The excited magnetization presents a second relaxation time, the transverse (spin-spin) relaxation time, depending on spins phasing/dephasing during the nutation:

- The longitudinal relaxation («spin-lattice» relaxation) is due to energy exchanges with the surrounding lattice. Actually, the spin system transfers the energy given by the excitation and tends to come back to the difference of energy level population at thermal equilibrium (more spins on the lowest state).

$$Mz(t) - Mo = (Mz(to) - Mo)e^{-\frac{t-to}{T1}} \quad \text{(VI.)}$$

The longitudinal relaxation is characterized by the relaxation time T_1. Any NMR experiment has to consider T_1 since it conditions the time allowed to the magnetization to recovers from previous excitation before doing the next excitation. **Therefore the repetition time (TR) choosen is related to the T1 of the sample.**

- The transverse relaxation («spin-spin» relaxation) is due to interactions between the spins themselves. These interactions progressively and irreversibly dephase the spins in the transverse plane, leading to a decay of the transverse macroscopic magnetization toward zero.

$$Mxy(t) = Mxy(to)\, e^{-\frac{t-to}{T2}} \quad \text{(VII.)}$$

The transverse relaxation is characterized by the relaxation time T_2. Note that the transverse magnetization decreases faster than the longitudinal magnetization, therefore $T_2<T_1$. In the case of short T_2, the sequence needs to be fast otherwise the signal intensity is too small to be captured. **The echo time (TE) needs to be much smaller (conventionally five time) than the T_2 of the sample (50-100ms).**

With the proton density ρ, these two relaxation times T_1 and T_2 are the most common parameters used to modulate the image contrast of a MR Imaging experiment, ,. These 3 parameters are the primary characteristics of tissues characterization in nuclear Magnetic Resonance Imaging (MRI).

1.3.2. MRI techniques: signal formation

The excitation as well as the signal detection is performed with coils based on the Faraday's law of induction. Inducing an electrical current in a transmitting coil generates a magnetic field. Reversely the variation of the magnetic flux through the coil surface generates an electrical current.

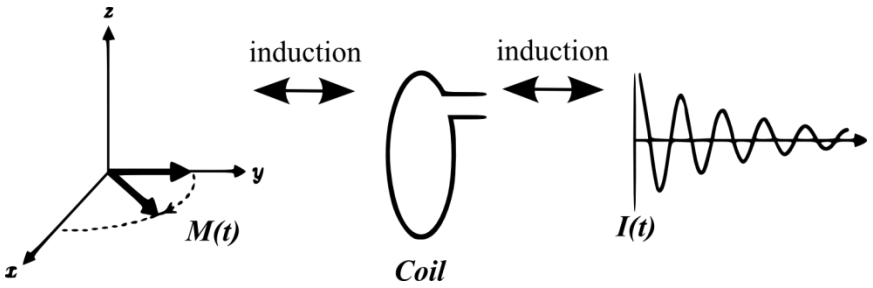

Figure 14: Basis of NMR excitation-reception. Excitation: an alternative current in the coil generates a variable magnetic field on the spin lattice. Reception: the magnetization generates a variable flux that induces electrical currents in the coil.

The electrical signal received by a receiving coil is called the Free Induction Decay (FID). This is an alternative signal oscillating around the Larmor frequency.

Spin Echo techniques

In order to "read" the magnetization, M is rotated into the transverse plane, manipulated with variable magnetic fields: magnetic gradient then brought back to its initial angle in the transverse plane. This creates an echo, appearing at a specific chosen time: the echo time TE. One the most common NMR sequence proceeds as follow:

-A 90° RF pulse along the x axis at t=0

-A 180° RF pulse along the y axis at t=TE/2

-The echo is generated at TE

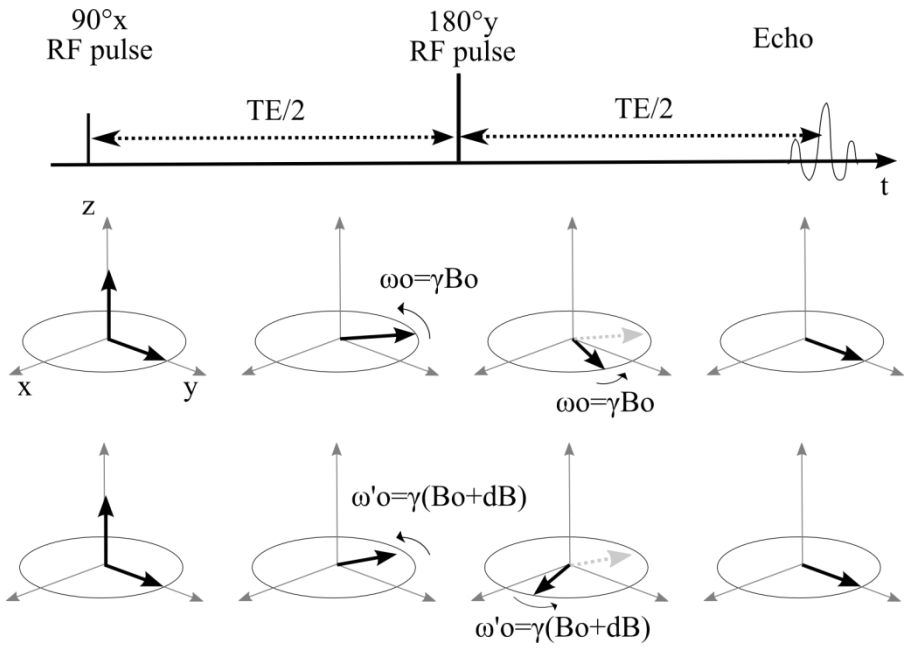

Figure 15: Spin echo principle. The spin echo enables to refocus spins even in the case of static magnetic field inhomogeneities (case at the bottom). Echo time (TE) occurs at twice the elapsed time between the excitation and the refocusing pulse (TE/2).

The advantage of such a method appears when we consider inhomogeneities in the static magnetic field **Bo**. The spins precess at different frequencies depending on their location in the inhomogeneous magnetic field. But with the spin echo scheme, they are all rephrased at the echo time. *Spin echo NMR sequences have the advantage of being able to compensate for Bo inhomogeneities.*

Spin echo sequences have:

- Less sensitivity to magnetic field inhomogeneity
- Higher SAR since at least 2 RF pulses are required one being a 180° pulse
- Longer TE, that affects motion sensitivity and T2 signal decrease

The present work in this manuscript will make use of a spin echo MRI sequence.

Gradient Echo techniques

In order to "read" the magnetization, M is rotated by only a small angle (α) from the longitudinal axis (z). Magnetic gradients rotate the magnetization back then forth to bring it back to its initial position. This creates an echo *in the rotating frame* (at $\omega = \gamma B_0$), appearing at a specific chosen time: the echo time TE. The sequence needs:

-A α° RF pulse (here along the x axis at t=0)

-A gradient lobe of intensity **-G**, along the readout direction, of duration τ

- A gradient lobe of intensity **+G**, along the readout direction, of duration 2τ

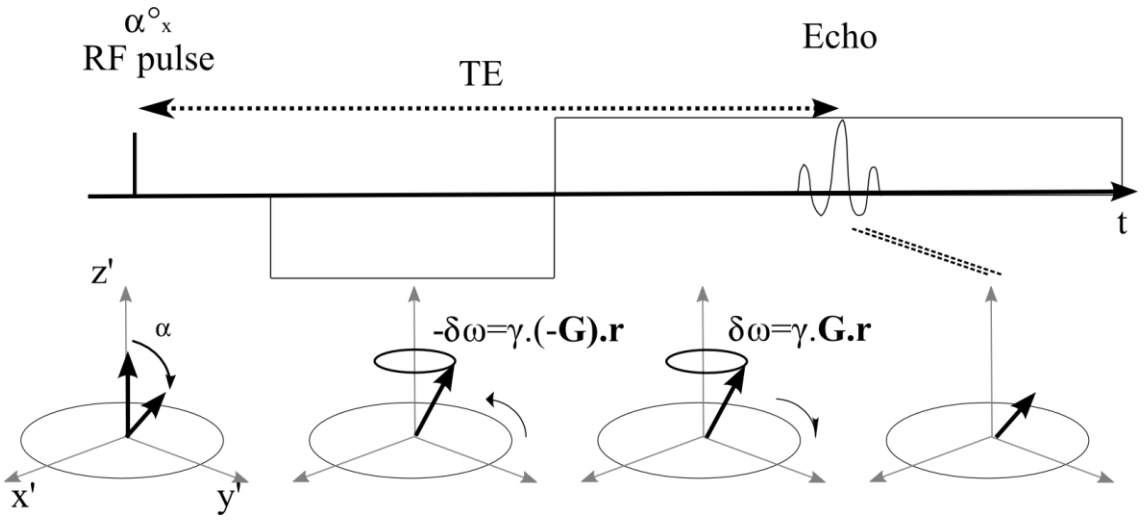

Gradient echo techniques are:

- Very fast (short TE)
- Use less RF power, thus deposit less energy in the body (low SAR).
- Are sensitive to magnetic field inhomogeneities. Spins at different magnetic field strength will not be refocused identically, thus the echo intensity will be less than for a spin echo at same TE.

The present work in this manuscript will not make use of a gradient echo MRI sequence in this form.

<u>Balanced Steady-State Free Precession (b-SSFP) techniques</u>

Balanced-SSFP mechanism was described long ago (Carr 1958), but has become of interest only through more recent developments which provide a robust T_2/T_1 contrast technique. Balanced-SSFP is based on the combination of a spin echo and a gradient echo.

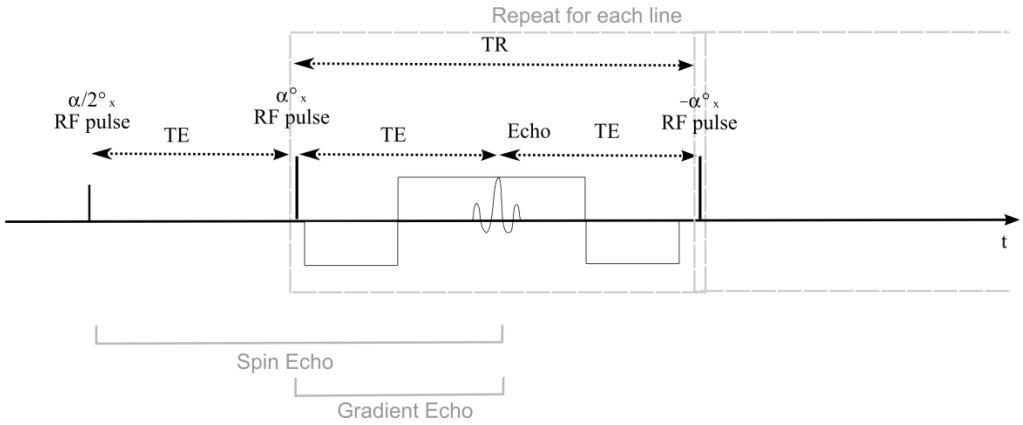

Figure 16: Schematic construction of a balanced-Steady State Free Precession (b-SSFP) MR sequence. The combination of a spin echo and a gradient echo creates a steady state after the second RF pulse ($+\alpha°_x$) that can be maintained with repeated RF pulses.

After the initial half-spin echo, the pattern in gray dashed-square is repeated for each line. At echo time (TE), both a spin echo from previous pulses and a gradient echo from present gradients are superimposed. Thus the repeat time TR=2*TE.

The technique is fast, with high echo intensity, but suffers off-resonance artifacts from its magnetic field inhomogeneity sensitivity, like gradient echo techniques. The present work in this manuscript will make use of a *b*-SSFP MRI sequence.

1.3.3. MRI: Encoding spatial information

Now that we know how to characterize tissues with NMR, it is important to be able to localize the source of the signal to differentiate tissues. All localization is based on the Larmor frequency relationship.

Basic space encoding scheme

1. The first step is to image only one slice using a space-selective excitation. The **slice selection** is performed with adding a linear gradient Gs to the static field **Bo** along its direction (z-axis) during excitation. Thus the magnetic field the spins see depends on their z position, so does their resonance frequency:

$$\omega_O(z) = \gamma(Bo + dB(z)) \qquad \text{(VIII.)}$$

By applying this gradient, it is possible to *excite only spins within a defined slice* thickness *Δz* with a corresponding selective excitation frequency bandwidth of *Δω=(γGs)*Δz*.

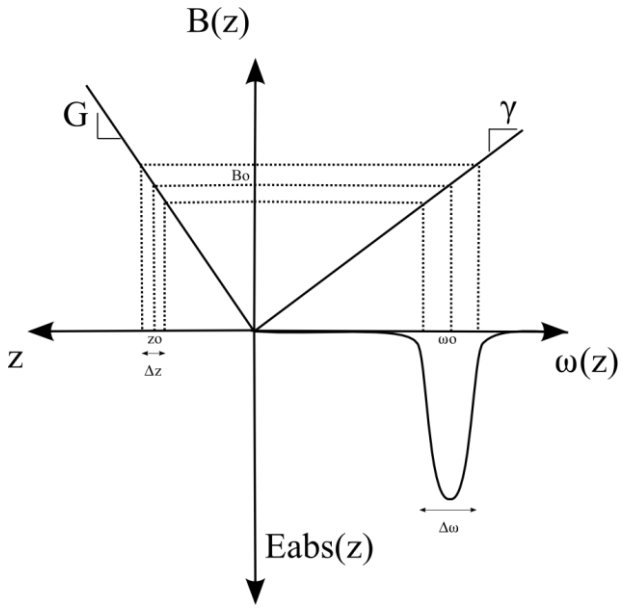

Figure 17: MRI slice selection principle. A magnetic gradient G creates a linear relationship between the magnetic field B and the spins location along the axis z: B(z). Thus spins resonance frequency depends on z according to the Larmor equation. Finally only the spins whose frequency is within range of excitation pulse frequency are excited: only a slice along axis z is excited.

2. Once a slice has been selected, the acquisition of the image remains to be done. Positional information along a first dimension is obtained by modifying magnetizations' phases along one of the inplane directions (in the example along the y-axis). This is the **phase encoding step**. By applying a linear gradient ***Gφ*** (as in step 1.) during a time ***t*** along the y-axis, the transverse magnetizations undergo different precession frequencies depending on their location along this axis. Therefore, at the end of the phase encoding step, different magnetizations along the y-axis have acquired different **phase angles *F* which are function of their y-position**. Thus lines can be resolved by reading the magnetization phase **after** application of the phase gradient.

$$y = \frac{\phi(y)}{\gamma G_\phi \tau} \qquad \text{(IX.)}$$

3. The final step is to resolve voxels within each line. As in step 1, a linear gradient ***Gω*** is used on the x direction **during** the readout of the signal. Thus spins frequency depend on their location along the x-axis. This is the **frequency encoding step**.

$$x = \frac{\omega(x)}{\gamma G_\omega} \qquad \text{(X.)}$$

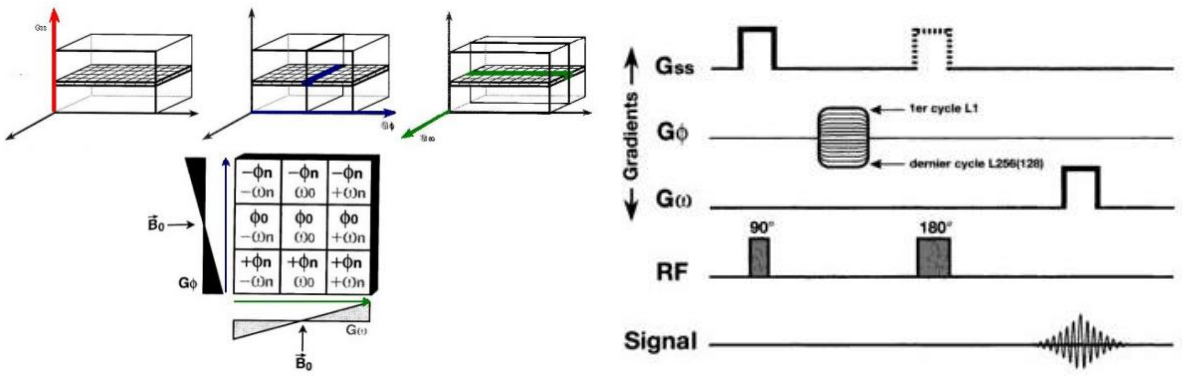

*Figure 18: MRI spatial encoding. First is the selective slice excitation with a gradient across the slice **Gss**. Then is the line encoding with a phase-gradient **Gφ**. Finally is the frequency encoding gradient **Gω** during the readout of the echo that differentiate voxels along each line. Corresponding time diagram for a spin-echo MRI experiment is illustrated on the right panel (Kastler et al. 2006).*

With this the location of each voxel is determined by its phase (=line on y-axis) and its frequency (=column on x-axis) at the time of readout. This creates the so-called *k-space* which presents 2 axis: phase and frequency axis. In order to recover the image from this k-space, a *2D Fourier transform* is applied to convert phase-frequency information into spatial x-y information.

Image reconstruction

Since MRI signal is acquired in the phase-frequency domain, a (discrete) 2D-Fourier transform (FT) is necessary to retrieve spatial information (since phase-frequency information is discrete within a pixels matrix, a discrete 2D-FT is used).

$$S(x,y,t) = \sum_{y}\sum_{x} K(x,y,t).\, e^{j(\omega(x)t+\phi(y))} \qquad \text{(XI.)}$$

Where *K(x,y,t)* represents the magnetization measured in k-space (phase-frequency space) and *S(x,y,t)* the spatial magnetization in the image space.

Low frequencies, corresponding to greatest changes in the image (contrast) are in center of k-space, while high frequencies, corresponding to small feature, details in the image, are in the outer k-space.

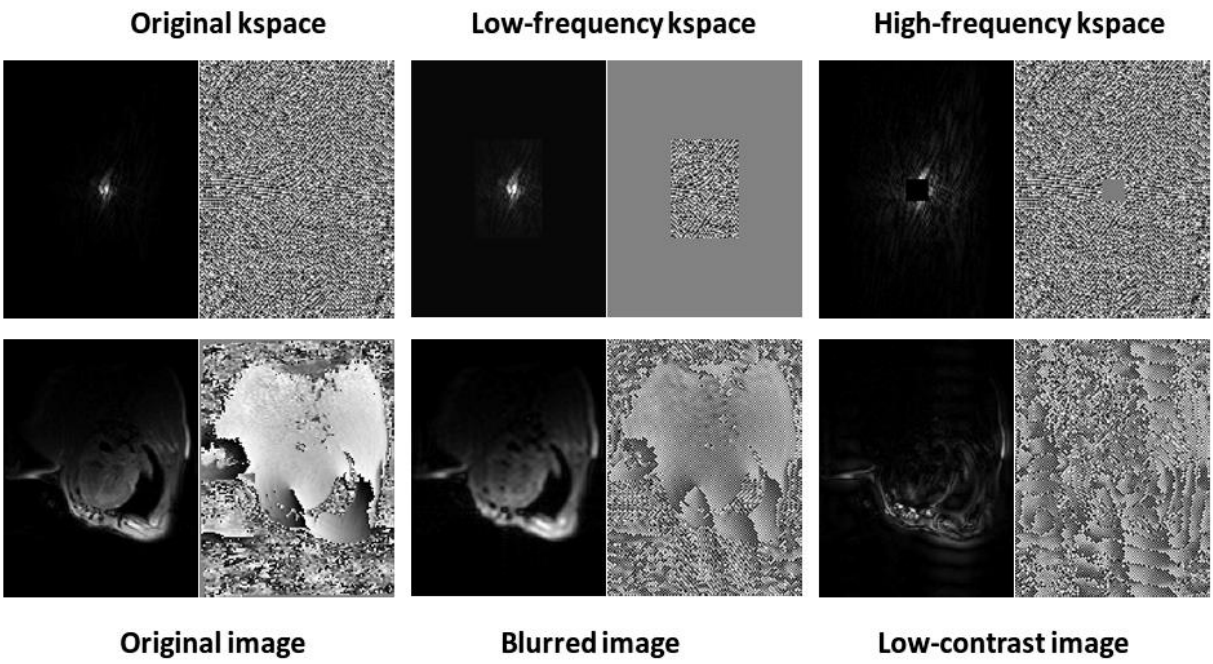

Figure 19: Image reconstruction depends on k-space content. Low-frequency k-space corresponds to contrast; High-frequency k-space corresponds to details in the image.

Echo Planar Imaging(EPI)

The basic space encoding scheme as described previously present a major flaw as it requires repeating the whole sequence for each encoded line desired. But it is possible to acquired the full k-space within one "shot" by successively dephase(change line) and read one line. This technique is called **echo planar imaging**. But since signal decays in time because of T_1 and T_2 relaxations, the EPI scheme was designed to read the whole k-space as fast as possible. Therefore gradient times are minimized by reading lines alternatively back and forth.

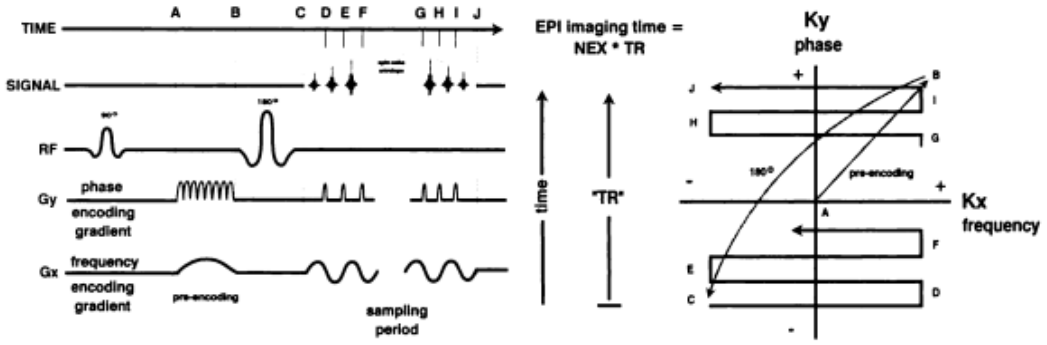

Figure 20: Time-diagram of an Echo Planar Imaging (EPI)MRI spin-echo sequence. Corresponding lines letters are reported on the read k-space on the right panel(DeLaPaz 1994).

This technique remains subject to improvements every year because of its sensibility to gradients flaws. It assumes ideal linear gradients while real gradients are subject to amplitude fluctuation and their switching time might be longer than predicted. It also remains limited in speed because of the gradients max amplitude and slew rate (see. 1.2.1. Gradients).

However the work presented in this manuscript depends only on EPI technique, with simple improvements such as partial k-space acquisition, sampling during gradients establishment (ramp-sampling, this is sampling while the practical linear gradients are not yet fully established) and post-processing distortions correction. With these improvements, EPI is a fast imaging technique that is more robust to off-resonance artifacts than some faster techniques such as spiral imaging(highly sensitive in cardiac imaging). Off-resonance artifacts come from an unexpected shift of resonance frequency. Different tissues in the body create additional gradients to the magnetic field. These static susceptibility effects cause the signal to appear at the “wrong” frequency. Other sources of off-resonance effects can be eddy currents. The effect of off-resonance with EPI is a signal loss and geometrical distortions, usually a shift in the image that does not affect the interpretation. However other fast readout techniques such as spiral are highly sensitive to off-resonance effects, which manifest as a damageable blurring. Therefore EPI remains a good compromise for fast MRI.

1.3.4. MRI hardware

Magnetic resonance imaging (MRI) implies several technological choices as well as many limitations depending on the study of interest. This part proposes a simplified overview of the main hardware elements needed to acquire an MR image:

- A strong static magnetic field usually provided by a superconducting magnet of several Teslas to create the magnetization. This magnet is coupled to a battery of “shims” (adjustable magnetic coils used to insure the best field homogeneity within the magnet.
- Radio frequency (RF) magnetic field emitting coils. These coils are needed to “create” a detectable magnetization (kW) to create the detectable signal
- RF magnetic field receiving coils. These coils are needed to acquire the macroscopic MR signal (mW) to detect the macroscopic signal.
- Spatially varying magnetic fields able to switch at audio frequency speed (gradients).
- And a computer to reconstruct images.

Each of these elements are vitals for the image MR images synthesis process and have to be dimensioned according to the MRI purpose (generic, cardiology, neurology, spectroscopy, imaging, ….)

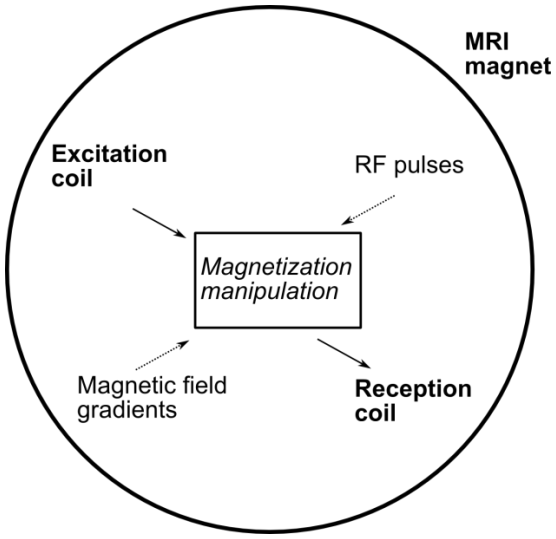

Figure 21: NMR experiment simple interactions model. The excitation creates a NMR signal, which can be influenced by magnetic field gradients and/or RF pulses. Resulting NMR signal is captured by a receiving coil. Excitation and reception coils can be differentiated or the same coil can play both roles.

Bo Magnet

Nuclear Magnetic Resonance occurs only in an intense static magnetic field. The main component of a MRI system is the magnet. The NMR signal increases with the static magnetic field strength, suggesting that higher fields are more suited for MRI (Haacke et al. 1999):

$$Signal \propto \frac{\gamma^3 Bo^3 \rho}{T} \qquad \text{(XII.)}$$

Apart from the technical difficulty of creating a stable magnet of great intensity, increasing the magnetic field presents several issues to the experimentation in vivo. **High field technical challenges include** (Snyder et al. 2009):

- field in-homogeneity
- sub-optimal ECG performance

Another immediate consequence of increasing the magnetic field strength is the increased difficulty to acquire electrophysiological activity, especially electro cardiogram (ECG) gating. The magneto-hydrodynamic effects cause the magnetic field to induce electrical currents in moving conductive fluid, modifying the magnetic field itself, but also spoiling the ECG. Synchronization is complicated at high fields (see figure below of ECG at 1.5T and 7T).

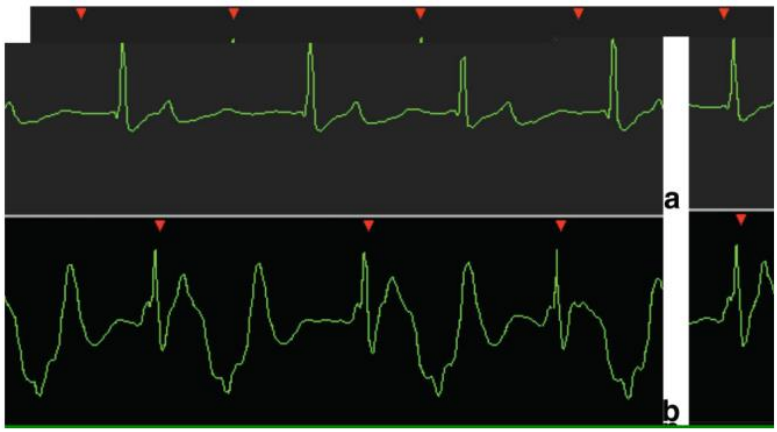

FIG. 2. **a,b:** Vector cardiogram traces of the aV_F channel acquired (a) outside (approximately 0.5T) and (b) inside the 7T whole body magnet. The red arrows show the accuracy of the gating despite the severe magneto-hydrodynamic effect.

Figure 22: Electro-cardiogram (ECG) for 0.5 and 7T. ECG distortions increase within high magnetic fields. Triggering becomes an issue for such intense fields NMR experiments on humans. (Snyder et al. 2009)

For all these reasons, clinical magnets are limited in magnetic field strength at ***1.5 and more recently 3 Tesla***.

RF pulses

A stronger static field implies the use of higher frequency RF pulses, which provides higher NMR signal but images become more sensitive to field variations. Magnetic field in-homogeneity introduces greater artifacts in the images. Motion, pulsation and susceptibility effects such as tissues interfaces (esp. air-tissues interfaces) are all sources of magnetic field inhomogeneity, creating as many sources of **artifacts**.

The main reason to limit magnetic field strength also comes from the consequently increasing radiofrequency power deposition on the patient's body that creates an important heating of the tissues. The mechanism for heating is the induction of eddy currents in the body by the time-dependent RF magnetic field in accordance with Faraday's Law, due to the finite conductivity of the body. Absorption of RF power by the tissue is described in terms of **Specific Absorption Rate (SAR)**, which is expressed in W/kg. (In the US, the recommended SAR level for head imaging is 3.2 Watts/kg.) SAR in MRI is a function of many variables including RF pulses frequency (related to field strength), pulse sequence, coil parameters and the weight of the region exposed. Because the proportion of power absorbed by the tissues is very high (70 to 90%), calibration of RF pulses is primordial.

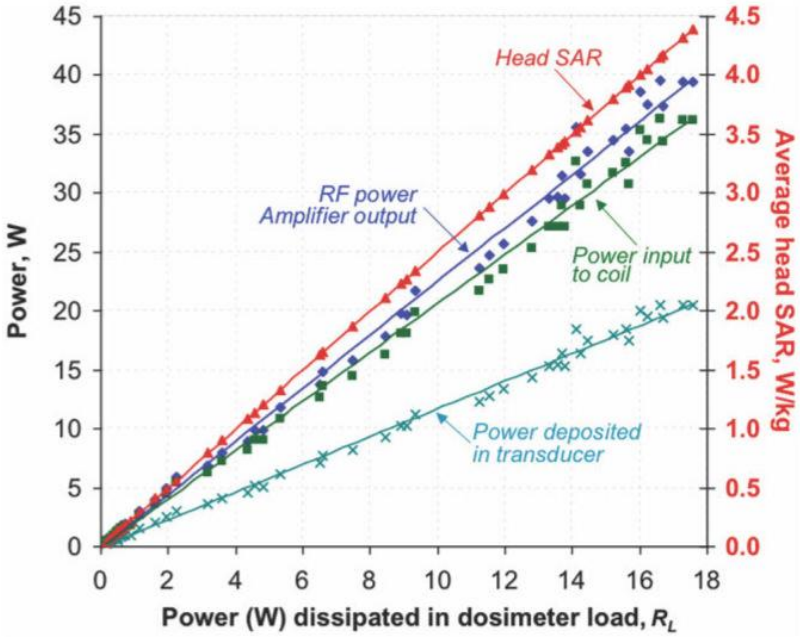

Figure 23: Power and SAR measurements from the prototype SAR dosimeter. The measured output power from the RF amplifier (blue diamonds and line of best fit), the measured input power to the birdcage coil (incident minus reflected power; green squares and line), and the total power deposited in the transducer as deduced from Eq. [1] (cyan crosses and line), all as a function of the power measured on the dosimeter load RL on the horizontal axis. The cyan curve relating actual-to-measured power in the dosimeter, is used for calibration. The red line (red triangles) plot the SAR (vertical axis at right) for the average head in W/kg, as a function of the power measured in RL on the horizontal axis. [A Prototype RF Dosimeter for Independent Measurement of the Average Specific Absorption Rate (SAR) During MRI](Stralka et Bottomley 2007)

While MRI would benefit higher resonance signal from increased excitation power, the SAR estimation and regulation provides the limits of application both in instantaneous power deposition and long-term heating during the full examination. Cardiac imaging is deeply affected by SAR limitation as the excitation needs to input a sufficient power amount into the heart muscle which in buried in the thorax, sometimes through a big wall of flesh, bones and fat. A lot of power is absorbed in the way, and the compromise between the minimum power to obtain a good enough image and the maximum power the

SAR limit can tolerate for the thorax. *The calibration of RF excitation is usually done by the scanner, which probes the "sample" before any MR exam. The MRI software estimates in real time the amount of energy deposit in the patient and prevent any armful heating by stopping the sequence acquisition or preventing it's launching if the energy deposit becomes higher than a safety threshold.*

For all these reasons, clinical magnets are commonly limited in magnetic field strength at ***1.5 and more recently 3 Tesla***.

Gradients

Spatial manipulation of the magnetization is done through the use rapidly varying magnetic field gradients. Gradients, which are switched on and off and modified during the course of the imaging experiment, have many uses, including:

- dephasing or refocusing magnetization
- Selective excitation
- Spatial encoding
- Contrast creation (such as perfusion and diffusion imaging)

Gradients are characterized by 3 parameters:

- Their amplitude
- Their duration
- Their rise time

The stronger gradients the hardware can achieve, the shorter the Echo Time and the better the spatial resolution can be. Also the shorter time the gradients are applied, the faster the images can be acquired, increasing the time resolution of examination. However the variation of the magnetic field causes the induction of electrical currents within body tissues. Thus their use has several limitations, both in speed and intensity. *Typical maximum gradient amplitude in clinical scanners reaches 40 to 80 mT/m.* The **slew rate** defines the speed rate of ascent or descent of a gradient from zero to its maximum

amplitude, either positive or negative. The slew rate is based on both the hardware limits and the limitation imposed by the induction in the body. *Typical slew rate ranges 100 - 200 mT/m/msec*.

Once all the hardware has been dimensioned, the sequence design implies different combinations of gradients and RF pulses towards the contrast desired. The more accurate and robust the contrast researched is, the more demanding on hardware the sequence will be. That is especially true in the case of diffusion weighted MRI contrast that aims at water molecule Brownian motion at a microscopic level.

1.4. Diffusion Weighted Magnetic Resonance Imaging (DW-MRI or DWI)

Non-invasive exploration of tissues structure

Basic MRI contrast characteristics were described previously: T1, T2 and proton density ρ. This paragraph will focus on another contrast, one that is of interest for this work: diffusion weighted MRI.

1.4.1. Diffusion theory

Brownian motion, or diffusion, describes the thermal random motion particles in a fluid undergo. This is a stochastic process in which particles probability density function associated to the position of the particles follows Brownian statistics. In our case, this is the random motion from water molecules in body tissues. Reading the diffusion of water molecules enables to characterize tissues as the random walk of molecules is restricted by their environment that is tissues structure. Therefore diffusion imaging has been of high interest in the past decade and remains yet a major subject of study and development.

In molecular diffusion, the moving entities are small molecules, here water molecules. They move at random because they frequently collide. Since collision times in typical solvents like water are about 0.1 nanoseconds, it is not possible to access microscopic motion with magnetic resonance imaging; however it is possible to access the macroscopic displacement of water molecules. Since diffusion is a three dimensional phenomenon, the mean displacement can be measured in every direction of space. The mean-square displacement $\langle r^2 \rangle$ depends on the time of observation t and the characteristic diffusion coefficient D (in m^2/s). D is the diffusion coefficient that, according to Fick's law,

represents the movement of molecules due to concentration gradients. However in body tissues, molecules random motion is also subject to pressure, thermal gradients etc. so that only an apparent diffusion coefficient can be expressed. In MRI, D might abusively be called diffusion coefficient but will always stand for this apparent diffusion coefficient. Einstein (A. Einstein 1905; Albert Einstein et Fürth 1956) demonstrated the relationship between D and $<r^2>$ to be:

$$< r^2 >= 2\, D\, t \tag{XIII.}$$

Since the random walk occurs in every direction, every component of diffusion influences the mean displacement over the 3 axis:

$$< r_a . r_b >= 2\, D_{ab}\, t\,, \qquad (a,b) \in (x,y,z) \tag{XIV.}$$

Thus D is a 3x3 matrix describing diffusion in every direction:

$$\boldsymbol{D} = \begin{bmatrix} D_{xx} & D_{xy} & D_{xz} \\ D_{yx} & D_{yy} & D_{yz} \\ D_{zx} & D_{zy} & D_{zz} \end{bmatrix} \tag{XV.}$$

From the definition, we have necessary $D_{ab} \geq 0$ and $D_{ab} = D_{ba}$, therefore D is a positive symmetric 3x3 matrix.

In a homogeneous medium, the diffusion is identical in every direction, thus this is an isotropic diffusion.

$$\boldsymbol{D} = \begin{bmatrix} D & 0 & 0 \\ 0 & D & 0 \\ 0 & 0 & D \end{bmatrix} \tag{XVI.}$$

Otherwise water molecules Brownian motion can behave as an anisotropic diffusion with a preferred diffusion direction (like in a tube). The diffusion will be directed along a preferred direction and reduced in other spatial directions. Mathematically this direction can be described by the eigenvector with the highest eigenvalue from the diffusion matrix *D* decomposition.

1.4.2. Diffusion encoding

MRI has the capability to read diffusion in both intensity and direction. It has been observed previously the spins precession speed depends on the field they are immerged in. Based on this observation, it is possible to render the precession speed space-related with the use of a gradient.

Let us consider a gradient **G** in one direction, spins precession speed depends on their position **r** along the direction of **G**:

$$\omega(\boldsymbol{r}) = \gamma(Bo + \boldsymbol{r}.\boldsymbol{G}) \quad \text{(XVII.)}$$

Diffusion MRI uses two opposite gradients of same direction and duration (Δ) but opposite intensity so that the additional phase accumulated during the first gradient is nullified at the time of the echo by the rewind phase during the second gradient:

$$\varphi_G(echo) = \int^{\Delta} \gamma(\boldsymbol{r}.\boldsymbol{G})dt + \int^{\Delta} \gamma(\boldsymbol{r}.(-\boldsymbol{G}))dt = 0 \quad \text{(XVIII.)}$$

But protons that change position between the two gradients will have different precession speed during the first and the second gradient, thus moving protons will have their precession speed vary and their total phase will not be null.

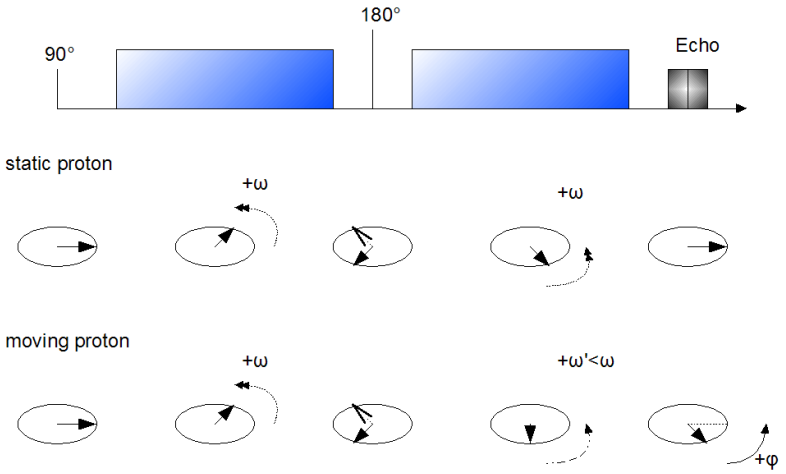

Figure 24: Diffusion weighted imaging (DWI) typical spin-echo sequence. Diffusion encoding gradients are identically split on each side of the refocusing pulse. Static protons are refocused at echo as if there were no gradients. However moving (including diffusing) protons do not fully refocus. The protons population phase shift creates an echo signal attenuation.

As the echo assumes refocused spins phases, its intensity will be decreased relatively to the number of spins with non-refocused phases. The more the protons will have diffused, the less intense the echo will be. The diffusion weighted signal depends on the *So* the signal without diffusion, and the mean phase shift squared (Bernstein, King, et Zhou 2004):

$$S = S_0 e^{-<\Phi^2>} \quad \text{(XIX.)}$$

Stejkal, Tanner and Torrey (Stejskal et Tanner 1965; Torrey 1956) have demonstrated the signal intensity depends on the diffusion coefficient:

$$S = S_0 e^{-bD} \quad \text{(XX.)}$$

b is the diffusion encoding parameter that depends on gradients intensity and duration. The b-value determines the range of diffusion coefficient perceptible with the chosen gradients. Small gradients will only be able to read high speed diffusion. Protons moving slowly will not dephase sufficiently in order to decrease the signal intensity. However protons undergoing fast diffusion will have a significantly decreased resonance signal. Basically in order to measure diffusion accurately, high b-values are required. Typical diffusion coefficient D in body tissues ranges 1-10.10^{-3} mm²/s = 1-10 µm²/ms, therefore common b-values range 100-1000 mm²/s so that the signal loss does not exceed 80% to limit DWI noise sensitivity.

1.4.3. Diffusion computation

Finally to quantify D in one direction, it is necessary to acquire at least 2 values of the signal: S and So or S with two different b-values.

$$D = -\frac{1}{b}\log\left(\frac{S}{S_0}\right) \;\; or \;\; D = -\frac{1}{b_2 - b_1}\log\left(\frac{S(b_2)}{S(b_1)}\right) \quad \text{(XXI.)}$$

Measuring only *Dxx*, *Dyy* and *Dzz* (the diagonal of ***D***) provides sufficient spatial information to characterize diffusion in space but does not enable the exact definition of main diffusion direction. This is defined as diffusion weighted imaging (DWI) and gives access to mean ADC maps (also called mean diffusivity (MD) maps, ADC_m maps) and a ratio corresponding to the anisotropy of diffusion (0 for isotropic diffusion and 1 for unidirectional diffusion), the fractional anisotropy FA :

$$ADC_m = \frac{D_{xx} + D_{yy} + D_{zz}}{3}$$

$$FA = \sqrt{\frac{3}{2}}\sqrt{\frac{(D_{xx} - MD)^2 + (D_{yy} - MD)^2 + (D_{zz} - MD)^2}{{D_{xx}}^2 + {D_{yy}}^2 + {D_{zz}}^2}} \quad \text{(XXII.)}$$

DWI requires only 3 orthogonal directions of acquisition, which accounts for a minimum of 4 acquisitions: 1 with no diffusion encoding (*So*, usually expressed as b=0) and 3 with a non-zero b-value (*S(b,Dxx)*, *S(b,Dyy)*, *S(b,Dzz)*).

But **to measure the full 3x3 matrix diffusion coefficient, it requires the acquisition along of at least 6 different directions** (D is symmetric). This is defined as diffusion tensor imaging (**DTI**). All DTI requires at least one acquisition without diffusion encoding (b=0) and 6 acquisitions with a non-zero b value in 6 equally divided in space: a minimum of 7 images acquisitions.

1.4.4. DWI contrast and applications

Initial applications

The initial development of diffusion weighted magnetic resonance imaging was first published by Le Bihan and al. in 1986 (D Le Bihan et al. 1986). The first applications were developed in brain imaging for detecting neurologic disorders. Because of hardware and MRI technical state limitations at that time, the early technique was limited to long applications and low b-values (<100mm²/s). These limitations provided a contrast that was mostly sensitive to motion and flows rather than water molecules diffusion only. Therefore it was stated more accurately as intravoxel incoherent motion (IVIM) imaging and extracted information were considered a mix of perfusion and diffusion within brain tissues.

More than twenty years from this paper, DW-MRI has made enormous progress and has propelled MRI to a whole new range of applications (Peter J Basser et Jones 2002; Denis Le Bihan 2008). Hardware improvements and new acquisitions techniques such as EPI and parallel imaging enables to reach really high b values (>1000 mm²/s) within hundreds of different spatial directions thus accessing real water diffusion measurements with a tremendous accuracy. From the principal diffusion direction is extracted the fibrous architecture of body tissues (P J Basser, Mattiello, et LeBihan 1994). The brain neural network presents a large number of investigations and remains a subject of great interest for its complexity and its alterations in the case of neural pathology.

Diffusion weighted MRI: handling ischemia

Diffusion MRI has now become a routine part of MR exams with a considerable impact for patients. DWI plays a critical part in the diagnosis of stroke patients and the subsequent treatment route.

Brain ischemia, also known as cerebral ischemia, is a condition in which there is insufficient blood flow to the brain to meet metabolic demand (Raichle 1983). Brain ischemia can lead to the death of tissues if blood flow is not restored rapidly. The main interest in diffusion MRI is its capacity to differentiate ischemic tissues within minutes to few hours following symptom onset when conventional MRI and X-ray computed tomography (CT) are unable to image changes at the time. The most probable theory is that ischemia, a perfusion deficit, induces particularly the cessation of aerobic metabolism. The major energy-yielding process in the heart goes through the metabolism of glucose and lipids by oxidative reactions. Thus a progressive lack of energy (ATP) for the cells occurs under anaerobic conditions, preventing cells regulation mechanisms (Das et al. 1987). Especially the accumulation of lactate and the alteration of ionic pumps (Na, Ca, H, K) impacts ever deeper the mitochondrial function, essential to aerobic metabolism. Because of altered ionic regulation, the electronic balance between intra and extracellular spaces becomes also affected. Because of this unbalance, osmotic gradients are modified through the cell membrane. The osmotic pressure draws water into the cell, dilutes the cellular contents, and engenders cell swelling. Cell swelling increases intracellular viscosity and prevents cell's regulation mechanisms even further. When ATP levels fall below those required to maintain critical membrane function, prolonged ischemia results in the onset of cells' death.

Before the necrosis, cells' swelling reduces extracellular space and increases intracellular viscosity without immediate modification of tissues water content (Sevick et al. 1992; Benveniste, Hedlund, et Johnson 1992). Therefore conventional imaging techniques show no change while diffusion weighted images and diffusion maps are able to show a reduction of water molecules diffusion that expresses as a hyper-signal in DW images and a hypo-signal in ADC (or mean diffusivity: MD) maps. Furthermore the ADC values decrease rapidly after the onset of ischemia but subsequently increase back within 7 to 10 days (Rajeshkannan et al. 2006). This additionally enables the differentiation of acute and chronic infarcts. Finally since the mechanism of ischemia as described above presents a delay between perfusion deficit and cells swelling, it is possible through the comparison of perfusion weighted imaging (PWI) and diffusion weighted imaging(DWI) to differentiate under-perfused tissues(dark in PWI) from tissues with reduced water diffusion(>= under-perfused area, bright in DWI). The difference between those two areas, **an image penumbra**, corresponds to tissues under-perfused yet not damaged. These are **salvageable tissues** that require immediate reperfusion (Hakim 1987).

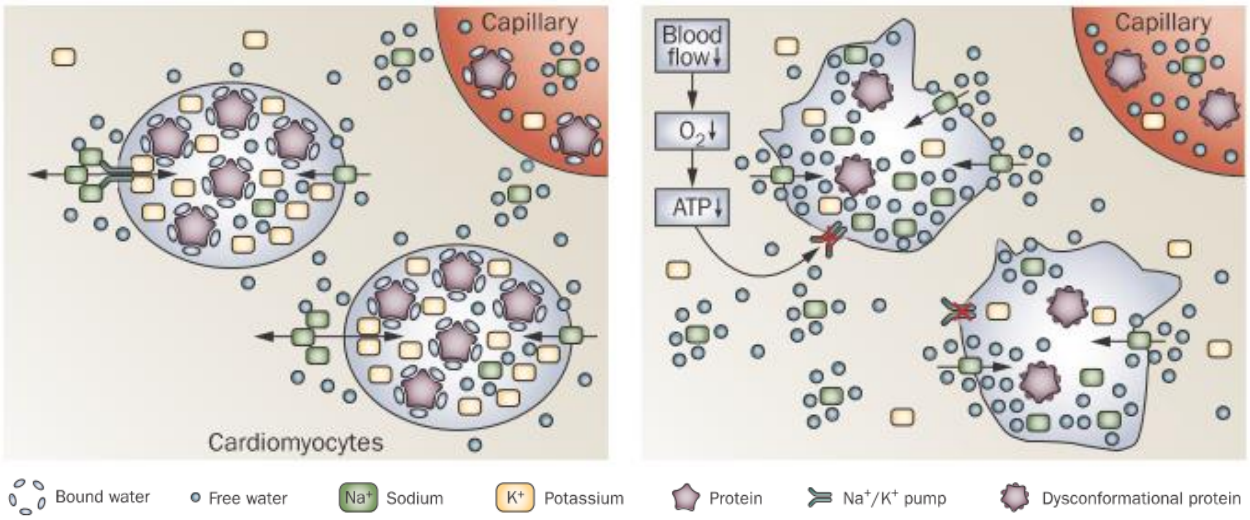

Figure 25: A simplified schematic view of edema evolution in ischemic injury to the myocardium. ***Left:*** *Normal equilibrium. Under normal physiological conditions, the intracellular-extracellular water balance is kept in equilibrium by an active, ATP-dependent Na+/K+ exchange and by the binding of water to complex molecules such as intracellular proteins.* ***Right:*** *Early phase of injury: intracellular edema. Very early after the onset of hypoxia, water is released from proteins because of lactate-induced acidosis, increasing the intracellular fraction of free (unbound) water. Furthermore, the mismatch between O_2 supply and demand causes a drop in ATP and leads to Na+/K+ pump failure. The increase in intracellular Na+ raises the intracellular osmotic pressure and pulls water from the interstitial compartment into the cells, leading to swelling and blebbing. At this stage of intracellular edema, capillary membranes are still intact because they are less sensitive to ischemia than are cardiomyocytes. Reproduced from (Friedrich 2010).*

DWI has other applications in brain imaging with smaller impact on routine clinic. As for diffusion tensor imaging, it is a topic of growing research in both technical refinements and clinical applications. DTI helps understanding the development and alterations of the neural network which proves useful in pathologies such as myelin disorder, epilepsy and neurodevelopmental disorders (Rajeshkannan et al. 2006).

Other areas of burgeoning applications for DWI are body imaging such as liver, prostate and spine cord imaging but cardiac imaging remains a challenge for DWI that prevents immediate applications of DWI as-is because of inherent limitations of DWI contrast mechanism.

1.4.5. DWI limitations

As described in 1.1.1, high b-values are required in order to measure diffusion accurately. But that would require more intense and/or longer gradients. Generating stronger gradients with good stability requires high-standard hardware and becomes very challenging when considering large imaging field such as whole body imaging. Stronger gradients raise another safety issue as magnetic gradients

create eddy currents within the body. These currents amplitude is related to the gradients strength, and one safety issue if their amplitude becomes too high is that they may trigger the nerves, which certainly needs to be avoided.

Another way of accessing high b-values is to increase gradients time, leading to longer echo time (TE). Longer TE consequently lead to greater T2-decreased echo signal. And longer TE increase also the acquisition sensitivity to motion, which in the case of diffusion weighted imaging, might lead to penalizing signal drop. According to equation (XVI), high b-values increase the signal drop. Additionally physiological motion can be of several scales' order larger than diffusion, which increases even further the signal drop. Figure below illustrate the relative signal amplitude for b=100mm²/s and b=1000mm²/s with motion ranging 1 mm²/ms (typical diffusion scale) to 10^3 mm²/ms (most important physiological motion scale, i.e. cardiac motion scale).

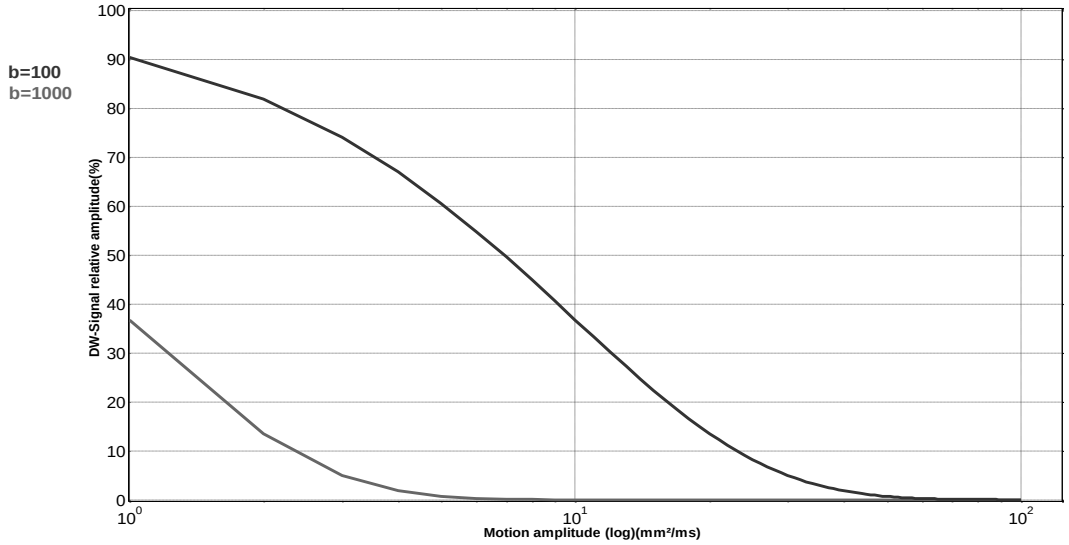

Figure 26: Signal intensity against motion amplitude. The diffusion parameter b is critical in the range of motion detected. Low b values (~100s/mm²) enable the detection of high velocity amplitude motion while high b values (~1000s/mm²) are used for accurate detection of slow motion. Slow motion, such as water molecules self-diffusion, can be detected only if they are not hidden by faster motion (e.g. blood flow) which decreases the signal more importantly. High b-values are more accurate but more sensitive at the same time.

Because of all these limitations, high b-values diffusion weighted imaging is challenging in practical set-up. Additional signal loss increases high b-values DWI noise sensitivity and prevents its application in the presence of important physiological motion.

2. In vivo cardiac DWI: feasibility and development

Magnetic resonance imaging has a lot of potential as diagnosis tool for cardiac imaging. Among the reasons for its investments and interests are it being non-invasive and its capacity to provide information of different kinds. MRI can picture body anatomy, characterize tissues, follow blood perfusion or neurons oxygen consumption and analyze mechanical contraction. Finally as described previously MRI has the unique potential of accessing tissues structure with diffusion weighted MRI. Cardiac imaging could certainly benefit from this contrast mechanism. But its application is facing several issues that prevent its use in routine as it is done for diagnosis in the brain. Only few people have tried cardiac diffusion weighted imaging so far.

2.4. In vivo C-DWI: limitations

Among DWI limitations described in 1.1.3, the main issue with cardiac DWI lies in the high motion sensibility of the technique. Because the heart is almost always in motion, acquiring motion-free images is considered impossible in routine. Physiological motion observed in cardiac imaging is the concurrent addition of: cardiac heartbeat motion, breathing motion, blood flow and any additional motion from the patient's movements. It is necessary to compare the scale of each motion to diffusion speed in order to understand their impact on diffusion weighted images. That is to understand the feasibility of cardiac DWI. The following considerations will focus on the left ventricular motion, center of interest for cardiac imaging.

First the typical velocity corresponding to water molecules diffusion is defined (with eq. X.) as:

$$V_{diff} = \frac{\sqrt{< r^2 >}}{t} = \sqrt{\frac{2D}{t}} \cong \sqrt{\frac{2 * 10^{-3} mm^2.s^{-1}}{50ms}} = 2.10^{-1} mm.s^{-1} \qquad \text{(XXIII.)}$$

While breathing motion can be suppressed with breath holds and blood flow does not significantly affect tissues, cardiac motion cannot be controlled and affects directly the signal of tissues. The heart beats regularly from 50 to 70 beats-per-minute (bpm) in a healthy adult (faster in children or patients) with a complex twist. The left ventricular (LV) motion can be decomposed in a rotation, a longitudinal contraction-elongation and a radial contraction. Left ventricular motion is irregular during the cycle (fig. below) with a major contraction during systole and a motionless phase during diastole. The first

important motion is the longitudinal shortening of the heart during ejection and subsequent dilatation of the left ventricle during the systole.

In order to quantify this motion, we acquired volunteers' (N=2) displacement encoded data (DENSE, (Aletras et al. 1999)) to access longitudinal shortening of the left ventricular and retrieve corresponding velocity. The thickening of 3 short-axis slices was measured at 3 different levels: basal, mid-ventricular and apical slice.

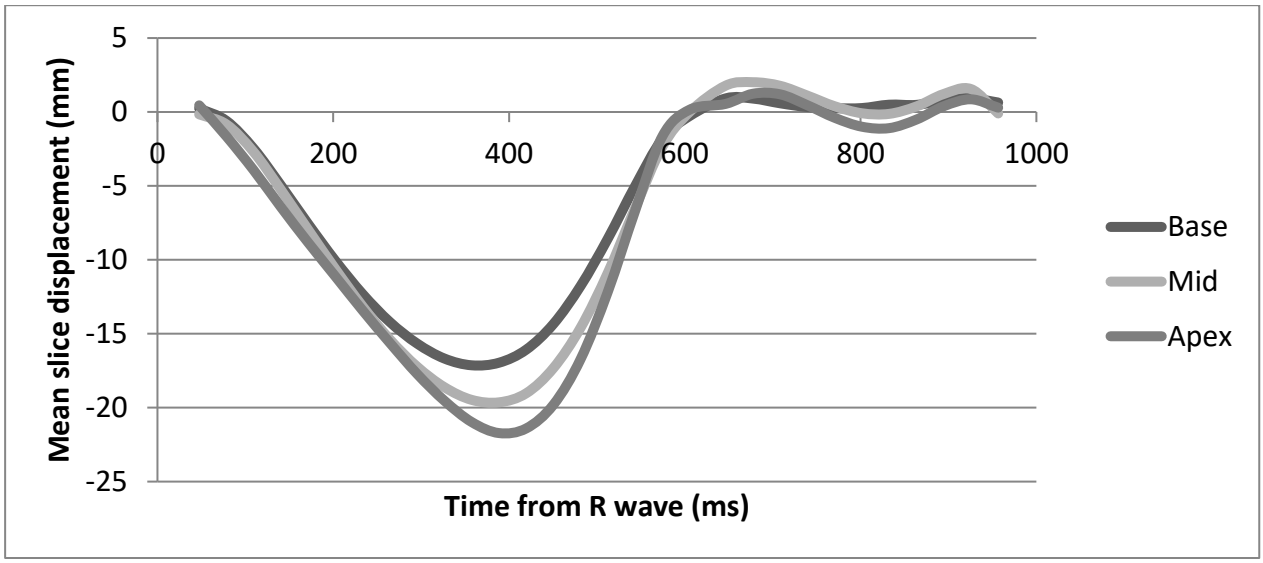

Figure 27: Mean displacement for 3 short axis slices in a volunteer during the full cardiac cycle. Data are extracted from MR-displacement encoded data.

The mid-ventricular slice is considered for further calculation of feasibility. This choice of level does not discard other levels as motion scale remains the same. This data set confirms a common knowledge that apical slices are harder to acquire than basal slices because of higher motion amplitude. Notice also that the peak systole differs a little in time: the maximum displacement is delayed from the base to the apex. Typical values of the human heart geometry are considered (10cm length, 3cm radius).

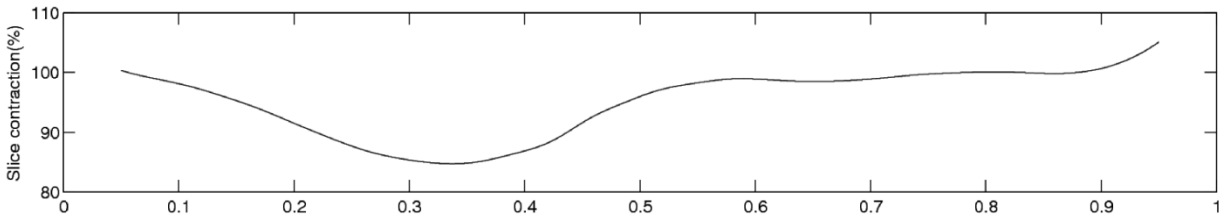

Figure 28: Mid-ventricular short-axis slice relative (%) contraction measured from motion-tracking MRI: displacement encoded (DENSE *(Aletras et al. 1999)*) data.

The shortening of the slice accounts for a longitudinal motion velocity of:

$$V_{long} = Heartlength * ContractionSpeed \cong 10cm * \frac{15}{100} * \frac{1}{200ms} \\ = 75\ mm.s^{-1} \qquad \text{(XXIV.)}$$

We also measured the rotation of the slice in the cardiac phase. Results were similar to the results from a previous study of the heart mechanics (Allouche et al. 2001).

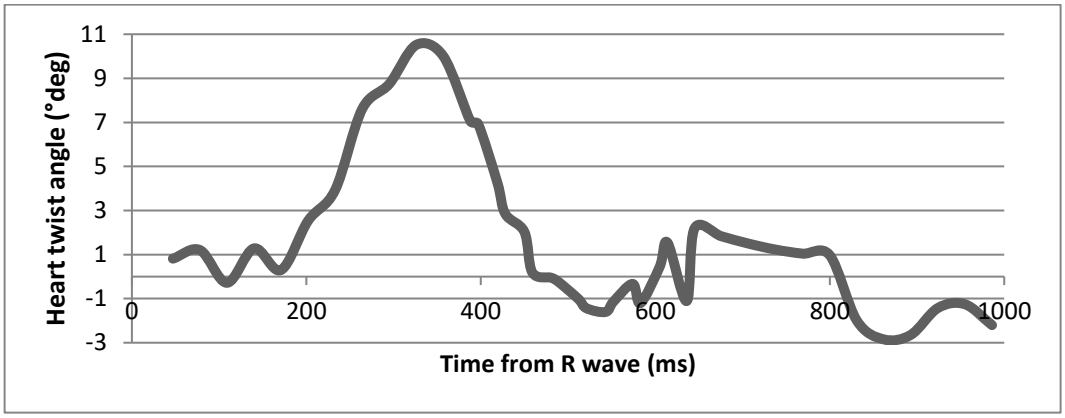

Figure 29: Experimental left ventricular rotation (°deg) extracted from motion-tracking data(DENSE (Aletras et al. 1999)) acquired in a volunteer's heart.

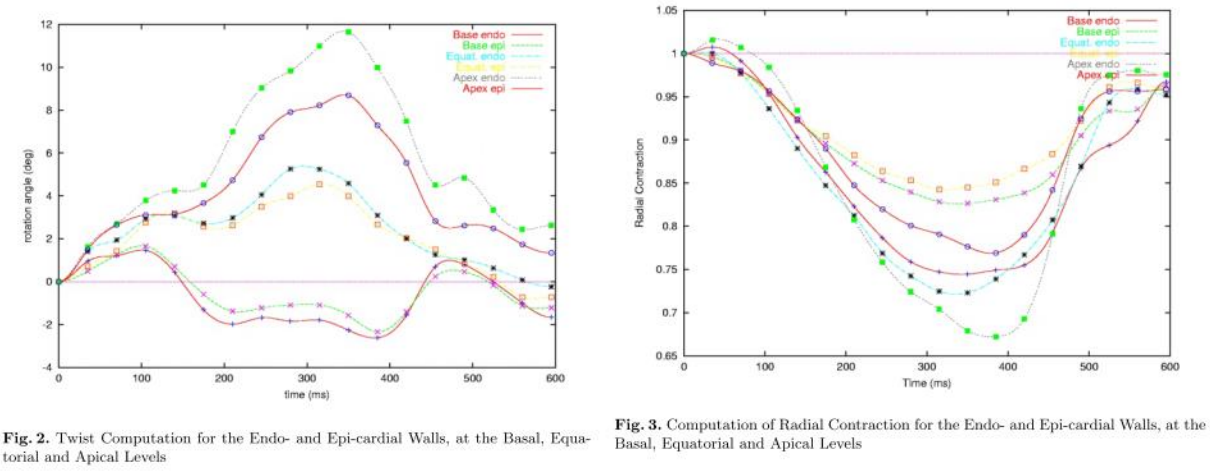

Fig. 2. Twist Computation for the Endo- and Epi-cardial Walls, at the Basal, Equatorial and Apical Levels

Fig. 3. Computation of Radial Contraction for the Endo- and Epi-cardial Walls, at the Basal, Equatorial and Apical Levels

Figure 30: Simulation data from a model of physiological cardiac motion (Allouche et al. 2001).

The rotation amplitudes range from -3° (apex) to +12° (base) angle peak. This leads to an approximate velocity for an equatorial slice during systole of:

$$V_{rot} = radius * \omega \cong 3cm * \frac{5°}{300ms} = 8.7\ mm.s^{-1} \qquad \text{(XXV.)}$$

And from the same mechanical model, the radial contraction amplitude for the same slice is:

$$V_{rad} = radius * v_{contraction} \cong 3cm * \frac{25}{100} * \frac{1}{300ms} = 25\ mm.s^{-1} \quad \text{(XXVI.)}$$

Overall **the mechanical motion velocity scales much higher than the water molecules diffusion's**, but looking at the pattern of motion, only the systole appears affected by important motion. The period of diastole offers a time-window of less motion, be it contraction or rotation. There is also a thin period at peak systole when the heart stays still after contraction (blood expulsion) and before left ventricular dilatation (filling).

However the blood flow during the diastole is increased (Klabunde 2004). And an average of the blood velocity ranges (Wieneke et al. 2000):

$$V_{blood} = 129 - 156\ mm.s^{-1} \quad \text{(XXVII.)}$$

From this analysis, **the feasibility of cardiac diffusion weighted imaging appears possible only at times of minimal physiological motion, at peak systole or during diastole, but DWI information will mostly be related to perfusion rather than diffusion**.

Diffusion weighted imaging also increases sensitivity of MR contrasts that are sensitive to the phase of spins. Therefore DWI usually suffers high sensitivity to magnetic field inhomogeneity as well as susceptibility artifacts such as from tissues interfaces. Finally it is important to note that with the limited resolution of MRI, each voxel encloses a great number of protons, thus only the average motion over the whole population of protons in the voxel can be accessed. Therefore the resolution of accurate information is limited to a macroscopic scale of intravoxel motion while the size of diffusive structures in body tissues (see chapter 1.2.5. p17) is far smaller than the size of a voxel.

2.5. In vivo C-DWI: previous achievements

Despite all these issues, few achievements of *in-vivo* cardiac diffusion weighted imaging have been published in the recent past years. Two different teams have proposed each their own approach, with their own advantages and drawbacks.

2.5.1. Stimulated-echo approach

Probably the most well-known team work on cardiac DTI comes from the Massachusetts General Hospital (MGH). The people there benefit from a 15 years-old long background in the experience of DTI motion sensibility reduction and DTI attempt on the heart (Garrido et al. 1994). They have explored many possibilities for diffusion weighted imaging in the presence of motion: twice-refocused spin-echo DWI sequence with bipolar diffusion encoding gradients (T.G. Reese et al. 2003) and stimulated-echo sequence also with unipolar and bipolar diffusion encoding gradient (Dou et al. 2002).

The results of their experience have come to the use of a stimulated echo (STEAM) diffusion weighted sequence combined with unipolar diffusion encoding gradients and EPI k-space readout (W Y Tseng et al. 1999; W Y Tseng et al. 2000). Images are always acquired at mid-systole and intermittent breath holds, with coaching of patients' breath holding at end-breathing compensate for both cardiac and breathing motion.

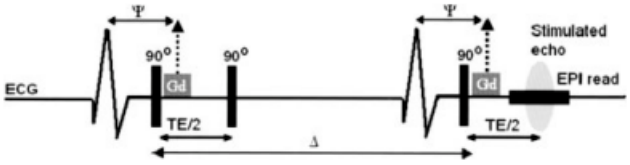

Figure 1. Pulse sequence of cardiac diffusion MRI. The sequence is a stimulated-echo single-shot echo planar imaging with 2 ECG triggers to locate the diffusion-encoding gradient pulses (Gd) at identical phase delays, Ψ, in consecutive cardiac cycles. The time between the onsets of the 2 diffusion-encoding gradients is the diffusion time, Δ, precisely equal to the R-R interval.

Figure 31: Time diagram for the stimulated echo DWI sequence used at the MGH(Boston, USA) and by their colleagues (Wu et al. 2006).

This sequence enables a short TE=42ms that provides b=300s/mm² along 6 spatially distributed directions (6 non-opposed edge centers of a cube). Averaging over 12 excitations compensates for poor signal-to-noise ratio. Overall the method proves to be efficient and provides motion-less accurate diffusion coefficient maps on different slices of the heart.

The MGH team, in collaboration with the National Taiwan University Medical College in Taipei, Taiwan, has performed few in vivo studies of the human heart. First studies were performed on healthy volunteers to refine the technique and validate the method (Dou et al. 2002; W Y Tseng et al. 1999). They notably studied the relationship between the myocardium fibers and cardiac strain maps in order to relate the myofiber shortening (W Y Tseng et al. 2000).

Finally their most advanced publications come to the analysis of hypertrophic cardiomyopathy with DTI to access the impact of the pathology on the heart architecture (Wen-Yih I. Tseng et al. 2006). The results show existent myofiber disarray in the hypertrophic hearts septum plus a reduction of fractional anisotropy (FA) in the myocardium. The paper also shows the correlation between a reduction of FA and a reduction in myocardium strain. Most of the study focuses on the helix angle of myofibers to quantify the fiber spatial organization and property. The second publication chooses to focus on the architectural impact of the heart remodeling after infarction (Wu et al. 2006). The results show a significant increase of apparent diffusion coefficient (ADC) and decrease of fractional anisotropy (FA) in the infarct zone. An important modification of tissue structure is observed in the fiber array which indicates the remodeling of the myocardium after infarction.

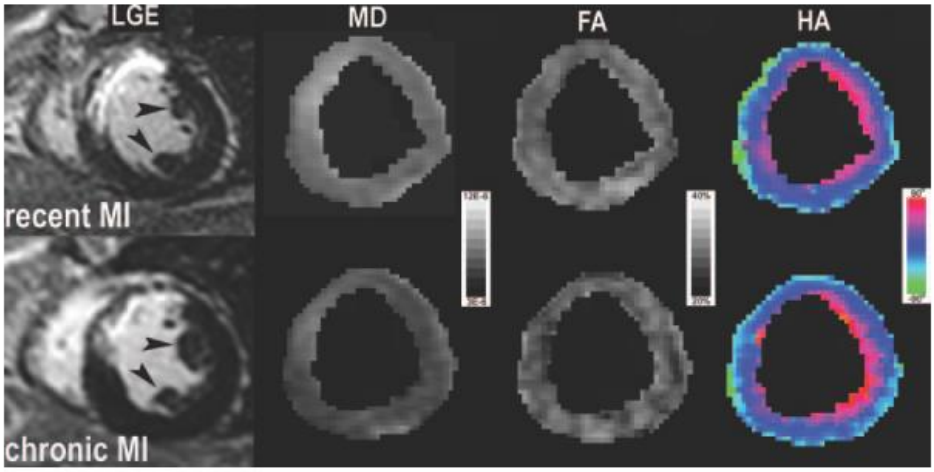

Figure 1. Macrostructure and microstructure MR in recent MI and chronic MI. Sequential MR of a 59-year-old man with MI due to left anterior descending coronary artery occlusion. Top, recent MI, taken at 14 days after infarction. Bottom, chronic MI, follow-up at 124 days after infarction. The segment of wall with hyperintensity over anterior-septal areas represented the infarct-adjacent zone. The remaining was the remote zone. HA maps showed more left-handed helical angle (increased green and decreased red pixels) in the infarct-adjacent zone. The zonal differences of microstructure could be appreciated with reference to LGE images in both recent and chronic MI. Papillary muscles, as indicated by arrowhead in LGE, were excluded for microstructure evaluation.

Figure 32: Results from the STEAM DWI approach. DWI parameters: mean diffusivity (MD), fractional anisotropy (FA) and helix angle (HA) are compared for an acute MI patient and a chronic MI patient (Wu et al. 2009).

The STEAM-DTI technique proposes a new contrast to characterize myocardium architecture and the method shows promising results in few of the most common cardiomyopathies. However the method remains difficult to set up, requiring high beat-to-beat reproducibility for exact triggering reproduction and intermittent breath holds for about than 30 minutes of acquisition for 3 slices are acquisition conditions that scarcely apply in a clinical context.

2.5.2. Spin-echo approach

The other group that has built experience in the field of in vivo cardiac DWI comes from the Eidgenössische Technische Hochschule (ETH) Zürich. Their method revolves around a spin-echo DWI sequence with bipolar diffusion encoding gradients for flow-compensation and EPI k-space readout (Gamper, Boesiger, et Kozerke 2007).

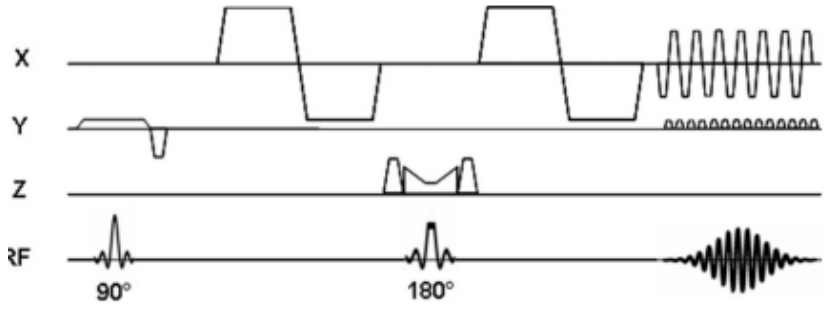

FIG. 5. Flow-compensated diffusion sequence with reduced FOV and VERSE echo pulse.

Figure 33: Time diagram for the spin-echo DWI sequence with flow compensation (Gamper, Boesiger, et Kozerke 2007).

From motion considerations, they have developed a sequence that provides motion-reduced diffusion weighted images with b=340s/mm² at echo time of 61 to 65ms along 6 directions in space. The images are acquired at mid-systole with free-breathing. Retrospective gating over 30 repetitions provided an averaging of about 15 motion-corrected images. Inner volume excitation helped accelerating the acquisition while removing EPI wrapping artifacts. Their results on healthy volunteers showed good correlation with the literature.

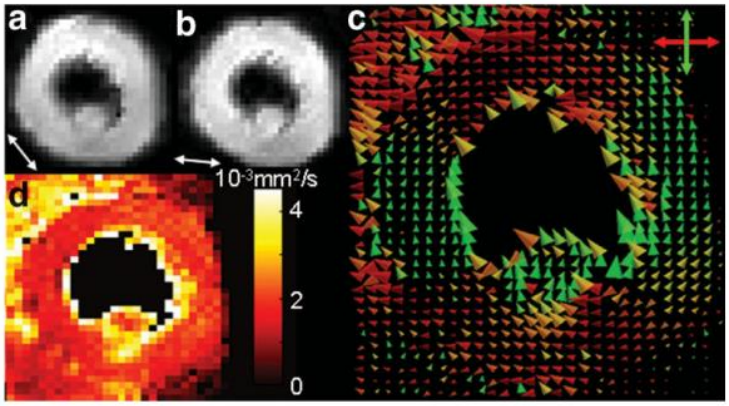

FIG. 7. In vivo results. **a** and **b:** Modulus images of a short-axis slice of the left ventricle on an equatorial level. The direction of the applied diffusion gradient is indicated by the white arrows. The (**c**) direction and (**d**) magnitude of the largest eigenvalue are shown color-coded.

Figure 34: Volunteer in vivo results from the spin-echo approach(Gamper, Boesiger, et Kozerke 2007).

Their work has lead to recent abstracts proposing 3D interpolation of the myocardium fibers network from multi-slice DTI acquisition (Toussaint, Stoeck, Kozerke, et al. 2010; Toussaint, Stoeck, Sermesant, et al. 2010).

Their results appear correlated with the ex-vivo literature but the method, with hours lasting acquisition, focuses mainly on innovative data without current interest towards clinical application. The acquisition method remains easy to transpose to harder conditions such as patients acquisitions. The acquisition for a DTI slice is very limited (7min) with accurate motion-less data.

2.6. In vivo C-DWI feasibility: analysis in a specified context

Context

The choice of methodology has immediate consequences on the range of study and applications that can be envisioned. **Towards a global and potentially clinical context**, the limitations are severe and define several starting points that cardiac DWI would be based on. Few main issues are to be considered:

- The **time limits** of a clinical examination. Research might allow hours of acquisition towards purely explorative goals. Knowledge certainly is highly valuable, especially in the domain of medical imaging, but working towards clinical applications requires very different approaches, with short delays from patients' table to clinicians.
- The **condition of patients**: spontaneous and uncontrollable physiological motion, limited (or no) breathe holds acceptance, etc.

- **Reproducibility** of the method: field inhomogeneity may be severe in some patients, also motion varies in time and from one patient to another.

Because our project of cardiac DWI has been clinically initiated, these limitations were always on our mind. Thus our technological choices were made towards a possible immediate application *in vivo*. Initial technological choices were:

- ***Single-shot (SS) spin echo (SE) sequence*** for minimum physiological motion sensitivity and high reproducibility rate.
- ***Echo Planar Imaging (EPI)*** to reduce distortions from field inhomogeneity and for the easy set up of the technique.
- ***Maximum of 10 min for a single slice acquisition***, although this upper limit was scarcely reached.

2.6.1. Tackling motion: slice thickness theoretical study

Physiological motion is the major issue to consider in the use of diffusion weighted imaging on the heart. Fischer and al.(Fischer et al. 1995) have demonstrated through plane motion is the most tackling issue in the case of phase sensitive NMR imaging. But Gamper and al.(Gamper, Boesiger, et Kozerke 2007) also considered heart rotation to be problematic for diffusion encoding. Mostly because of the heart beating, the selected slice sees its shape and position modified between the excitation pulse and the reading gradients. The myocardium contracts and twists with shortening, rotation as well as displacement of the slice. This motion induces a phase shift of the signal. This phase shift reduces the resonance signal, spoiling any phase sensitive contrast, especially diffusion imaging. In order to evaluate the influence of motion on DWI signal, we consider the signal expression, from the solution to the Bloch equations (Stejskal et Tanner 1965):

$$\frac{\partial \vec{\mathrm{m}}}{\partial \mathrm{t}} = -\mathrm{i}.\gamma\left(\vec{\mathrm{G}}.\vec{\mathrm{r}}\right)\mathrm{m} + \vec{\nabla}.\mathrm{D}\nabla\vec{\mathrm{m}} \qquad \text{(XXVIII.)}$$

Leading to the solution:

$$\mathrm{m} = \mathrm{m}_0 \mathrm{e}^{-\mathrm{i}\,\Phi}\,\mathrm{e}^{-b\,\mathrm{D}} \text{ with } \Phi = \int \gamma\left(\vec{G}.\vec{r}\right)dt \qquad \text{(XXIX.)}$$

m_0 is the maximum magnetization without diffusion and motion de-phasing. Φ is the phase shift resulting from motion of the position vector and the diffusion weighting decrease stands depends on the

apparent diffusion coefficient *D* and the sequence diffusion weighting parameter *b*. Resulting transverse magnetization is noted *m*. We then integrate the magnetization along the slice thickness *s*. The worst case scenario of a phase shift induced by a diffusion gradient perpendicular to the slice, on which direction(noted *z*) the main deformation occurs is considered :

$$\mathrm{A} = \mathrm{A}_0 \mathrm{e}^{-b\mathrm{D}} \left| \int_{\mathrm{s}} \mathrm{e}^{-\mathrm{i}\Phi(\mathrm{z})} dz \right| \qquad \text{(XXX.)}$$

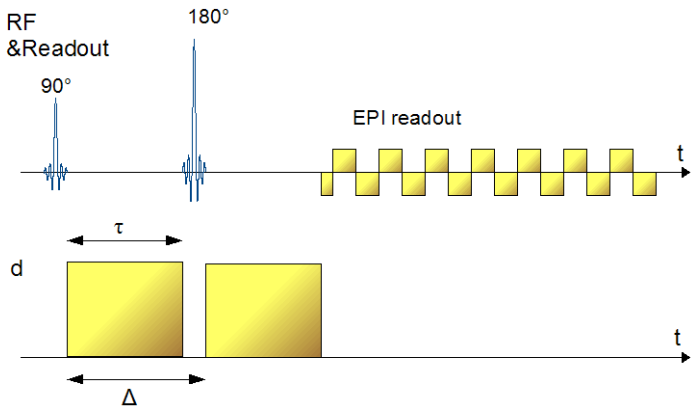

Figure 35: simplified time diagram of the basic diffusion weighting imaging (DWI) sequence. Upper line: the typical spin-echo EPI sequence. Lower line: additional symmetrical diffusion-encoding gradients in the chosen spatial direction *d*.

Initial approach used basic DWI sequence design (Stejskal et Tanner 1965). In order to reduce the sensitivity to motion artifacts, fast unipolar diffusion gradients were considered on each side of a 180° refocusing pulse. Influence of image encoding gradients and ramp times are considered negligible (figure above). Since the left ventricular (LV) remains the most tackling issue in cardiac diseases, we focus on the LV motion only. A simple model of the LV motion is the simple but reliable case of constant local contraction/relaxation acceleration. The slice thickening is decomposed in two parts (figure below):

- the systole with a ***constant accelerated slice shortening then widening***: $\frac{d^2\vec{r}}{dt^2} = a(z)\overrightarrow{e_z}$.
- the diastole with no significant slice thickness modification.

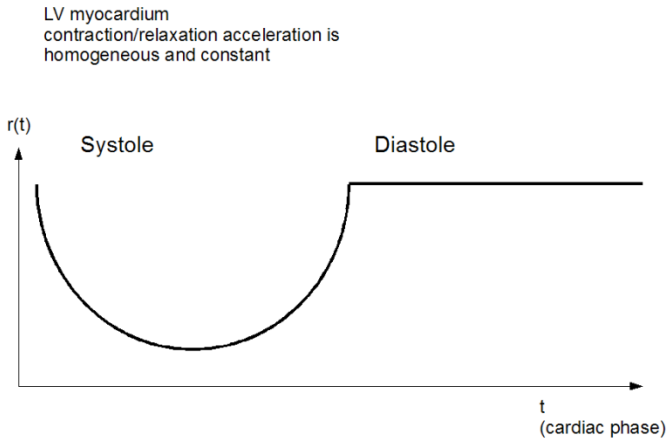

Figure 36: Simple **model** of cardiac motion. Constant accelerated transversal slice shortening during systole.

The contraction of the heart occurs in a twist that uses both rotation and wall thickening (i.e. muscle shortening=contraction, followed by a dilation of the muscle). In order to investigate the impact of slice rotation on diffusion coefficient measurement we consider the position vector to evolve with the rotation angle as (Fischer et al. 1995):

$$\vec{r}(\alpha) = z.\cos(\alpha)\,\vec{e}_z \qquad \text{(XXXI.)}$$

Rotation model was deduced from physiological observations:

$$\alpha(t) = a^2t + bt + c \qquad \text{(XXXII.)}$$

Leading with the small angle approximation to:

$$r(t) = z.\left(1 - \frac{(at^2 + bt + c)^2}{2}\right)$$
$$r(t) \approx z(\frac{(2 + c^2) + 2bct + (2ac + b^2)t^2}{2}) \qquad \text{(XXXIII.)}$$

<u>Validation of cardiac motion model with in-vivo physiological data</u>

Acquired physiological values from volunteers' *in vivo* displacement encoded (DENSE (Aletras et al. 1999)) images series provided realistic displacement for one mid-ventricular slice. Model-based relative acceleration of the LV derived from *in vivo* data ranged from 200mm/s² to 400mm/s².

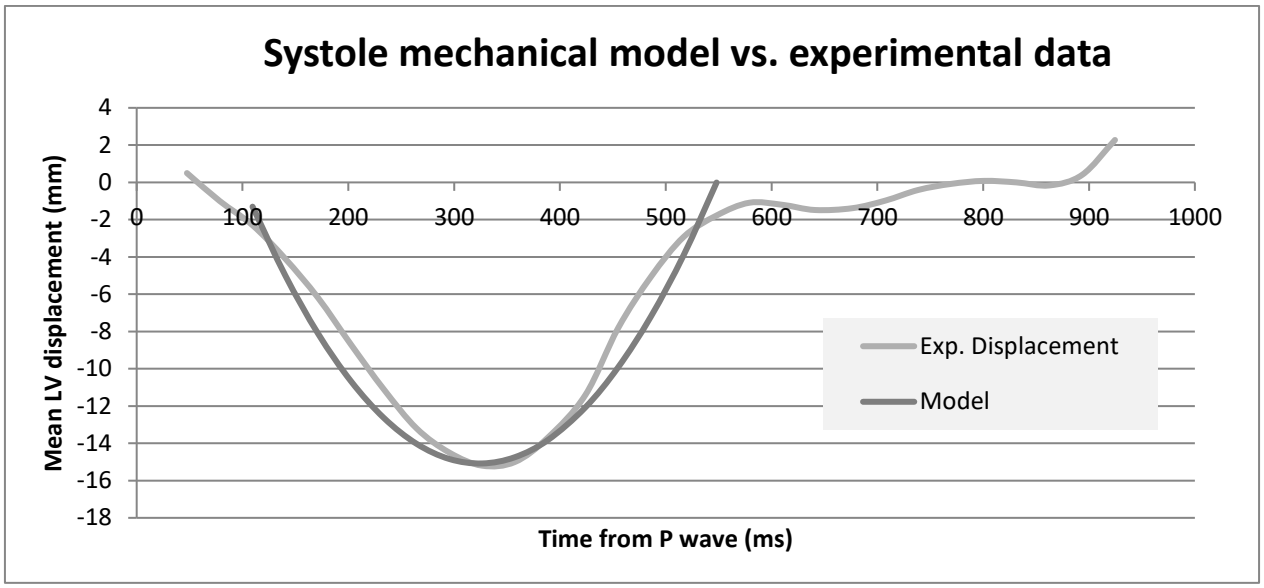

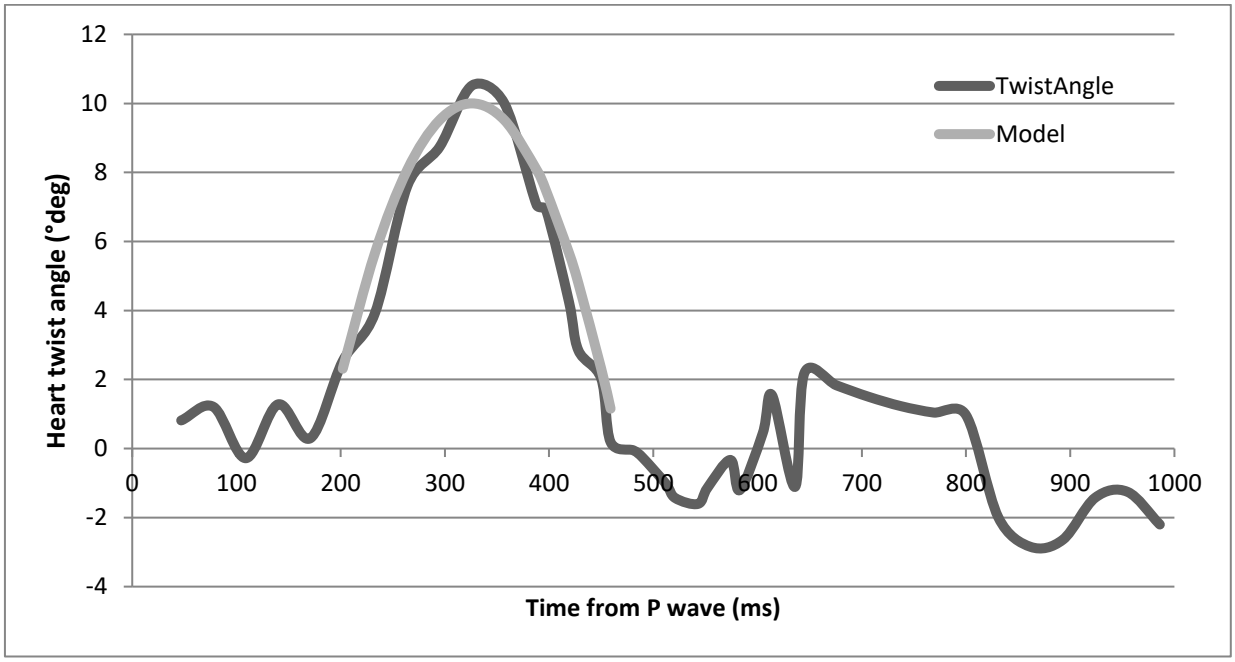

Figure 37: ***TOP****: Simple mode for systole contraction fitted on experimental data (DENSE) from a volunteer;*

BOTTOM*: heart twist includes important myocardium rotation along cardiac phase*

Volunteers' displacement encoded (DENSE (Aletras et al. 1999)) images also provided data for a significant myocardium rotation from the twist of the heart during its cycle. Particularly the sudden backward rotation at early diastole adds a sever motion in a short time-window (figure above, 100 ms).

2.6.2. Cardiac motion model: Translation Model

The phase shift induced by slice shortening becomes:

$$\Phi(z) = \int_t \gamma\left(G(t).a(z)\frac{t^2}{2}\right)dt = \gamma\tau^3 G_0 a(z) \qquad \text{(XXXIV.)}$$

To determine we assumed the apex to be fixed and the left myocardium to shorten uniformly from the base:

$$a(z=0) = 0\,; a(z=z_{max}) = a_{max}\,; a(z) = \frac{z}{z_{max}}a_{max} \qquad \text{(XXXV.)}$$

This sets the expression of the echo intensity to be:

$$I_{echo} = I_0 e^{-bD}\mathrm{sinc}\big(\Psi(s_0)\big) \text{ with } \Psi(s_0) = \frac{\gamma}{2}\tau^3 G_0 \frac{a_{max}}{z_{max}} s_0 \qquad \text{(XXXVI.)}$$

I_0 is the maximum amplitude of the echo, without diffusion or motion de-phasing. $\Psi(s_0)$ is the phase shift resulting from motion. The resulting echo intensity is noted I_{echo}.

Consequently motion decreases the intensity signal, resulting in an overestimation of apparent diffusion coefficient (ADC). Improving DWI accuracy requires the reduction of motion effect. Maximum tolerated motion effect was defined as *r=10%* increase of ADC estimation.

$$\Psi(s) = \mathrm{sinc}^{-1}(e^{-b\,r\,D}) \qquad \text{(XXXVII.)}$$

According to eq. XXIV maximum motion effect limits the slice thickness s_0 to guaranty accuracy of DWI measurements. Maximum slice thickness was computed with typical values: $z_{max} = 10cm\,; G_0 = 40\frac{mT}{m}; D = 1mm^2/s.$

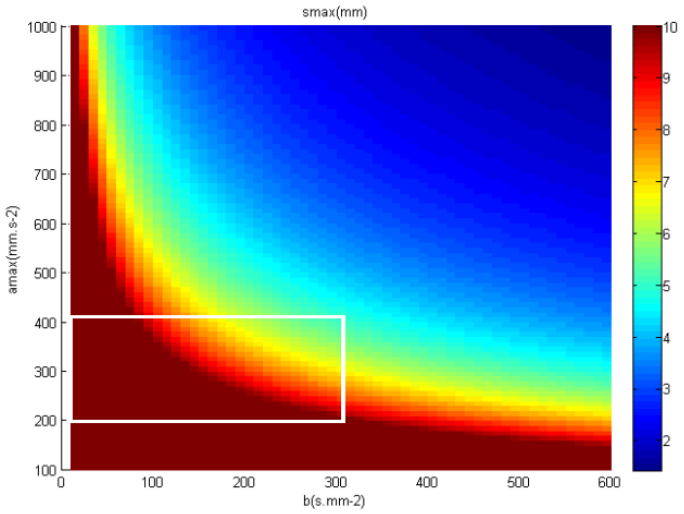

Figure 38: *maximum slice thickness for a 10% accurate diffusion measurement in the presence of constant acceleration systolic contraction*

Maximum slice thickness drops down very fast with the diffusion weighting b value increasing (figure above). As expected, high b values, increasing the motion sensitivity of the sequence, can hardly be employed for in vivo cardiac imaging.

Since *b* values over 300 s/mm² are unrealistic for cardiac DWI, a window (white box figure above) of realistic values provided with a maximum slice thickness around 6 mm.

2.6.3. Cardiac motion model: Rotation twist Model

The simplified rotation model with an equivalent rotation speed $\omega^2 = 2ac + b^2$ leads to a phase shift:

$$\Psi(s) = 2\gamma\tau^3 G_0 s_0 \omega^2 \qquad \text{(XXXVIII.)}$$

With the tolerance of 10% error of ADC estimation, a maximum slice thickness is determined depending on ω and *b* value:

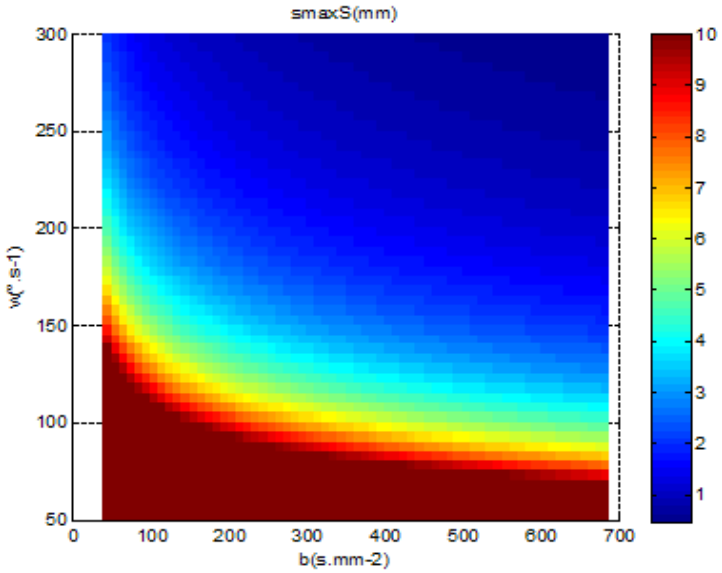

Figure 39: maximum slice thickness for a 10% accurate diffusion measurement in the presence of left ventricular rotation

Given the rotation observed in physiological data to be around $\omega \approx [50\ 100] rad.s^{-1}$, we observe the slice shortening remains the most tackling issue in cardiac DW-MRI.

2.6.4. Influence of slice thickness: experimental findings

As our models suggest, the slice thickness is a critical parameter that influences DWI sensitivity to motion. To confirm this influence, a volunteer's experiment involving repetitions of the same slice DWI acquisitions was performed. All parameters were kept identical except for the slice thickness. As triggering in systole proved results difficulty reproducible, trigger was set at a phase of less motion in diastole.

Method

Experiments were conducted on a 1.5T clinical scanner (MAGNETOM Avanto, Siemens, Erlangen, Germany) with a maximum gradient strength of 40 mT/m and maximum slew rate of 200 mT/m/s. Diffusion weighted imaging was performed with a single-shot, twice-refocused spin-echo EPI sequence available on the clinical scanner (T.G. Reese et al. 2003). Acquisition parameters were: imaging matrix of 128x160 with isotropic in-plane resolution of 2.6x2.6mm² and slice thickness ranging 2 to 8 mm, GRAPPA (Griswold et al. 2002) parallel imaging acceleration of rate 2, echo time (TE) of 51 ms, diffusion weighting b values of 0, 50 and 100 s/mm^2, and 3 orthogonal diffusion encoding directions for each non-

zero b-values. Acquisitions were ECG-triggered at every 2 heart beats to ensure that TR ≥ 2 sec. An initial dummy scan was used to reach a steady state. The slice was positioned at a mid-ventricular level.

Diffusion-weighted images were compared on their DW signal intensity (SI), images' Signal-to-Noise Ratio(SNR) and apparent diffusion coefficient (ADC) estimation. DW image SNR was evaluated as:

$$SNR(b) = \frac{< I(b) >}{Noise(b)} \qquad \text{(XXXIX.)}$$

where "< >" denotes the mean over the left ventricular wall and *Noise* was measured by the standard deviation of pixel intensities in a signal-void region of the DW image.

Results

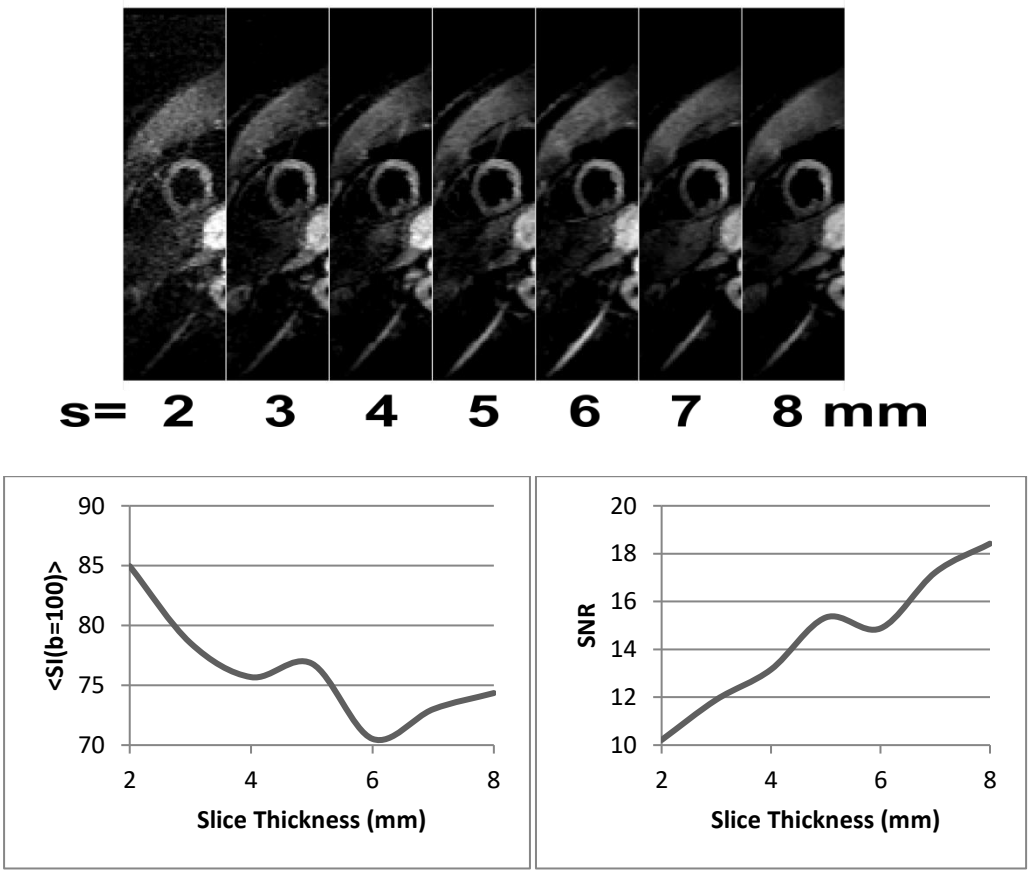

Figure 40: Influence of slice thickness on DWI signal intensity(SI) and signal-to-noise ratio(SNR).

Figure: **TOP:** Trace-diffusion weighted images(T-DWI) for b=100s/mm² of a volunteer's heart with increasing slice thickness s. All images are scaled identically. **BOTTOM:** DWI signal intensity (DW-SI) and signal-to-noise ratio (SNR) depends on the thickness of the acquired slice.

Measured mean myocardium signal intensity (<SI>) supports our theoretical study findings that signal loss increases (thus SI decreases) with slice thickness *s*, motion being a potential reason for decreasing DW-SI. Contrarily to usual signal intensity behavior in MR acquisitions where SI increases with slice thickness because of increasing number of excited protons, DW-SI drops almost linearly with increasing slice thickness (but for *s*=5mm where acquisition seems better). A plateau were the intensity does not decreases further seems to occur above 6 mm-thick slices. However the signal-to-noise ratio increases near linearly with *s*, as is common in MRI. Moreover SNR values are very low, as show the trace-DWI above. Therefore high slice thickness might be preferable for the readability of DW-images.

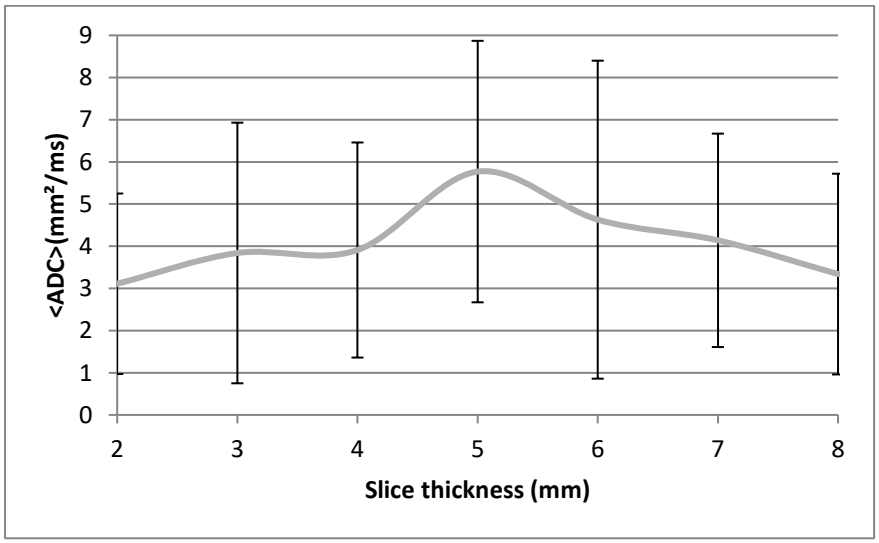

Figure 41: Influence of slice thickness on ADC measurements.

Mean ADC measurements in the myocardium reveal a fluctuation of results depending on *s*. ADC variations are of order of the measurements standard deviation represented as error bars. ADC is supposedly low in the myocardium, cardiac motion inducing a parameter over-estimation because of additional signal-loss on top of DWI encoding signal-loss.

Conclusion on appropriate slice thickness for cardiac DWI

Theoretical model of motion influence on DWI signal loss revealed the slice thickness to be a critical parameter in the output image quality. Although no ideal slice thickness can be deduced from this

short study, its implication has been clearly defined. In our present experimental context, thicker slices appear wiser as the SNR is increased while signal intensity remains sufficient. In the case of noise-less acquisition, with perhaps better coils, but also in the case of critical motion, thinner slices would reduce the impact of motion on DW-SI and improve image quality by trading a little SNR. Currently the slice thickness for further study was set at 6 mm as a reliable compromise with sufficient SI even in the case of patients or pigs with severe conditions and thus important motion.

2.6.5. Evolution of signal intensity with repetitions

One of the conditions to possibly apply DWI into a cardiac study in vivo is that the acquisition does not double the time of the study, or more. However since the T_1 of heart tissues ranges about 1s (Sparrow et al. 2006), a sufficient time for signal recovery between each acquisition shot is required.

We studied the signal intensity behavior in the hypothesis of a triggering every heart beat. One freshly excised human heart was acquired with a repetition time TR=900ms (typical RR time-interval).

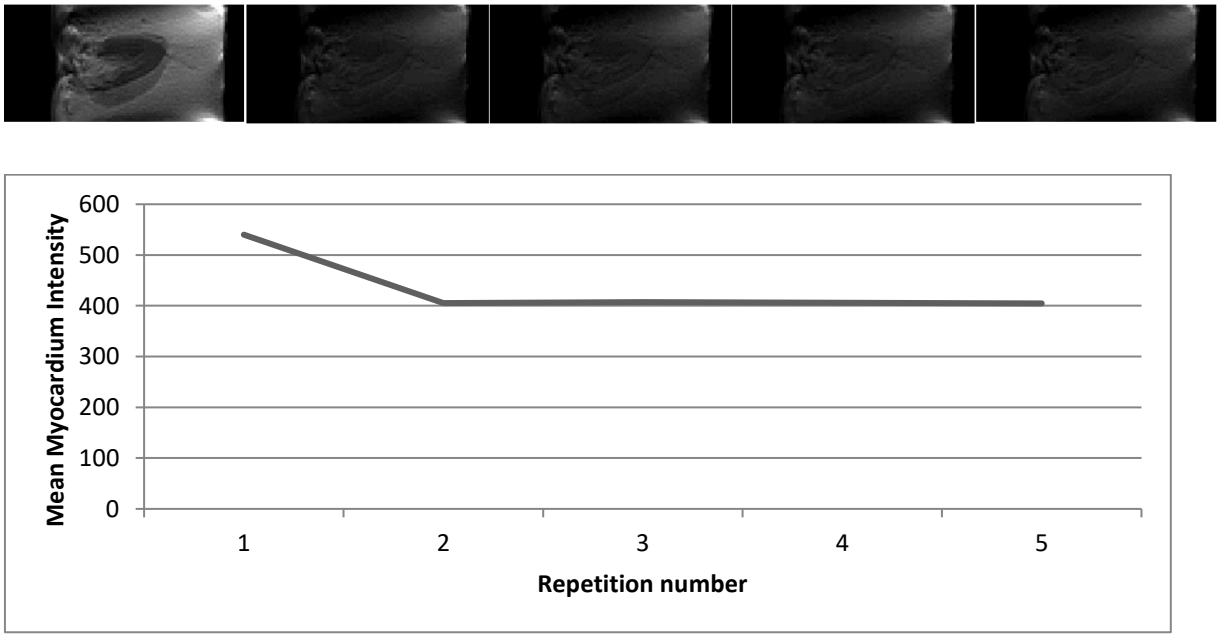

*Figure 42: Ex vivo signal variation of cardiac DWI for **TR=900ms** (typical RR interval). The human excised heart is fixed in a water-growing gel(**TOP**). Images are long-axis oriented, heart is oriented horizontally. Mean DWI intensity reaches a steady-state after the first acquisition (**BOTTOM**).*

Mean myocardium intensity proved to be stable after the first shot, thought the intensity dropped drastically after this initial acquisition. This study provided one important condition for future in vivo acquisitions: **TR >> T_1** = 1s for sufficient time to let signal recover between each acquisition shot. Or another option shown is this short study is to launch a **dummy scan** before the acquisitions series and deal with a steady-state of signal excitation-recovery at a lower mean intensity.

All of our studies were performed with both a dummy scan at the beginning of acquisition series and a repetition time set to guaranty a minimum signal-recovery time of min(TR) = 2*T_1 = 2 s (i.e. acquisitions were triggered every 2 heart beats in humans with HR ~ 60 bpm, or every 3 heart beats in the cases of HR >60bpm or observed arrhythmia).

2.6.6. Delineation of optimal time-window for cardiac DWI triggering

Cardiac longitudinal motion is one of the most important issues for MR contrasts sensitive to phase variations (T.G. Reese et al. 2003) that suffer additional signal loss and distortion from it. As motion vary significantly along the cardiac phase, the captured instant during a DWI acquisition can be reduced with appropriate triggering.

Method

To analyze the impact of cardiac beating motion along the cardiac cycle on diffusion weighted signal loss, a numerical simulation was performed using *in vivo* cardiac longitudinal motion measured with motion tracking MRI (displacement encoded with stimulated echoes (DENSE (Aletras et al. 1999))). Simulation started from homogeneous (D=5 mm²/ms) low b-values (0, 50 and 100 s/mm²) DW image intensity. The acquisition was assumed to be performed with twice-refocused spin-echo echo-planar imaging (EPI) sequence (T.G. Reese et al. 2003) with ideal gradients (no rise-time). Volunteer's DENSE displacement data $\vec{r}_m$ from a mid-ventricular slice (6mm thick), were added to diffusion displacement $\vec{d}$ and used as input for the simulation.

$$\vec{r} = \vec{r}_m + \vec{d} \qquad \text{(XL.)}$$

And phase was computed to deduce the expected signal loss (Bernstein, King, et Zhou 2004, 276):

$$\Phi = \int \gamma\left(\vec{G}.\vec{r}\right)dt \text{ and } \mathrm{S} = \mathrm{S}_0 \mathrm{e}^{-<\Phi^2>} \qquad \text{(XLI.)}$$

The intensity of highest b values achieved (b=100s/mm²) was studied against trigger time in cardiac phase. The phase of most durable maximum intensity was defined as the optimal time-window for triggering further DWI acquisitions. DWI acquisitions corresponding to simulation on the same volunteer were performed to confirm this finding.

Results

DWI intensity varies much from longitudinal cardiac motion during the cardiac cycle. Contractile motion prevents the acquisition of diffusion-weighted data in most of systole phase but at peak systole. The difficulty at acquiring cardiac DWI data is well illustrated here as motion varies from one heart-beat to the next one, in the same subject, depending on its heart rate and varies even more from one subject to the other.

Simulated motion-induced signal loss tends to be minimal in several short time-windows in end-systole and mid-diastole and in an 80 ms window in end-diastole. Experimental DWI data from the volunteer tend to confirm the existence of the short end-systolic window and the longer end-diastolic window (figure Bottom). It showed that motion related intensity drop was only tolerable in a short optimal diastolic window and a window of less than 100 ms in end-systole.

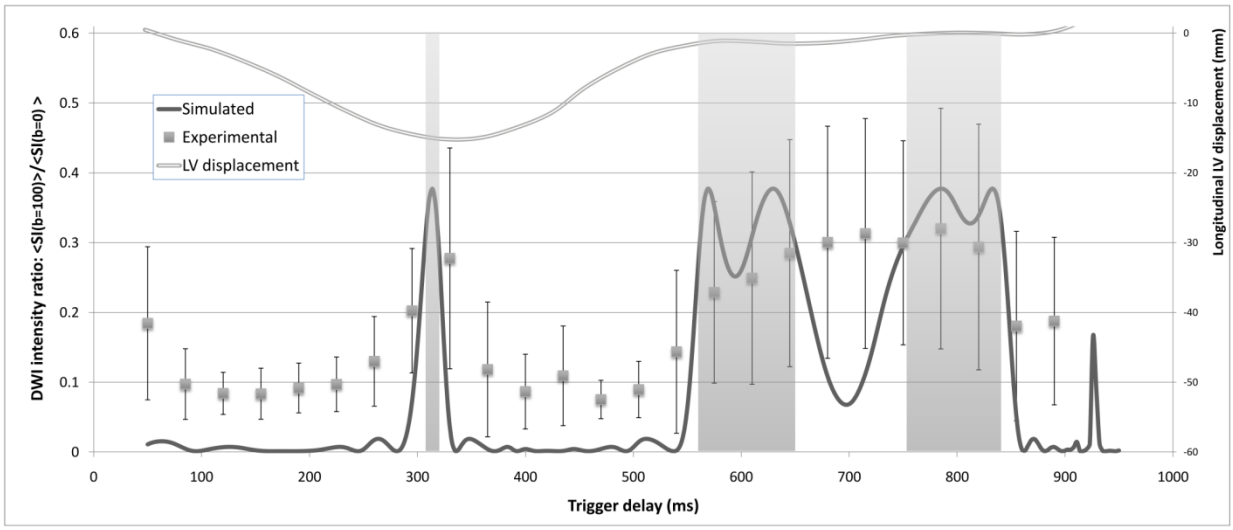

*Figure 43: Quantification of longitudinal cardiac motion and associated DWI signal loss (measured as the ratio: <SI(b=100)>/<SI(b=0)>) in a mid-LV short-axis slices of a healthy volunteer. Experimental slice contraction data over the cardiac cycle (**TOP**) were used to estimate DWI signal loss by simulation for b = 100 s/mm². Simulations were performed for the same slice thickness of 6 mm as actual DWI experiments. Panel (**BOTTOM**) shows simulated vs. measured signal level over the cardiac cycle for b = 100 s/mm². Simulation shows that signal loss is minimal only in few phases of the cycle (gray areas). The optimal time-window lays in diastole and is about 80 ms long. Experimental results support this finding but in mid-diastole where signal intensity appears more stable than predicted*

Conclusion

These results suggest that an optimal phase for triggering DWI acquisition should be set in mid-diastole. This choice also eases intra and inter-study variations: the variability of the motion during the same study as well as among different patients will be reduced if acquisitions are triggered in diastole. Ideal procedure consists in defining early to mid-diastole as the phase of less motion from CINE image series, which are common parts of CMR studies. A 100 ms time-window corresponding to early to mid-diastole can alternatively be defined based on ECG, although this procedure should not be encouraged. Then DWI acquisitions can be tested in this diastolic optimal time-window.

Discussion

While our study proposes an optimal time-window for triggering DWI acquisitions in diastole, several achievements in the past have chosen a trigger at mid-systole (W Y Tseng et al. 2000; Wu et al. 2006). Our study supports the feasibility of such acquisitions. However the time-window at peak systole is very short and physiologically depends highly on instant heart rate. Thus our experience is that such an acquisition is difficult to reproduce but provides DW-images with almost no motion indeed.

Additionally ***these two windows present very different physiologic information*** (see chapter 1.2.5. for coronary blood flow description): myocardium tissues will have ***reduced perfusion during the peak systole time-window*** while ***the microcirculation will attain its maximum amplitude during early diastole***. Therefore pure diffusion information will be difficult to differentiate during diastole but might be preponderant at systolic time. However Callot et al (Callot et al. 2003) results suggest the vascular system aligns with the tissue fibers, providing the same structural information at higher displacement amplitude. For this reason as well as for the longer duration of the diastolic time-window, we defined our optimal time-window for repeated measurements and a comparative basis lies within diastole.

Reported experience

At the early stage of this work, triggering was sought at diastole as this study recommends. However finding the exact optimal time-window was difficult from one study to another: after rough diastole observation from CINE acquisitions, several guessed attempts were made (with 5ms increment/decrements) before an optimal trigger time was reached.

2.7. TMIP-DWI: a new approach to reduce DWI physiological motion sensitivity

2.7.1. Acquisition Method

Our strategy to cope with intensity fluctuation resulting from motion, is to acquire multiple DWI images for a given slice position with incremental trigger delays as illustrated in figure 28. Our acquisition strategy of sliding acquisition windows that cover the whole optimal time-window of minimal motion is intended to capture the moment when motion-induced signal loss was at minimum, i.e when the attenuation caused by motion is minimum.

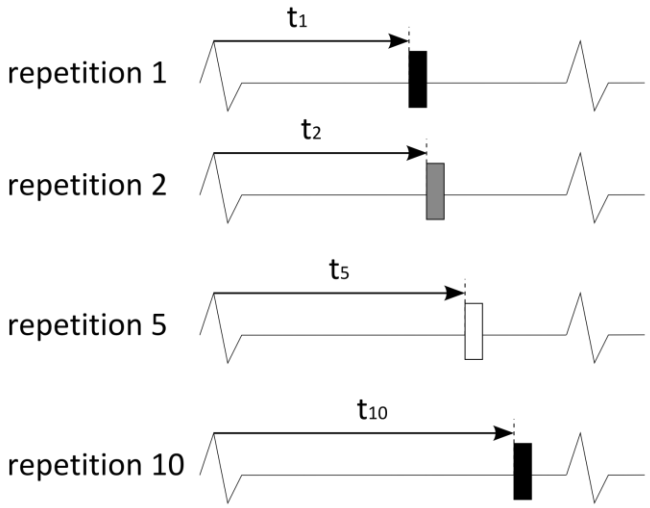

Figure 44: TMIP acquisition strategy: Temporal MIP (TMIP) acquisition strategy is designed to capture motion-related signal variations and extract an image of minimum motion-induced signal loss. Boxes represent time-shifted DWI repetitions while grayscale represents signal intensity variations due to physiological motion within the cardiac cycle. Brighter boxes correspond to minimum motion-related attenuation and dark bands to maximum attenuation.

As physiological motion impact on DW signal is an additional attenuation, while diffusion attenuation is a permanent attenuation (at our scale), the minimum captured attenuation will be the closest to the pure diffusion attenuation. Therefore the maximum intensity along time would correspond to the least motion-artifacted diffusion-weighted image.

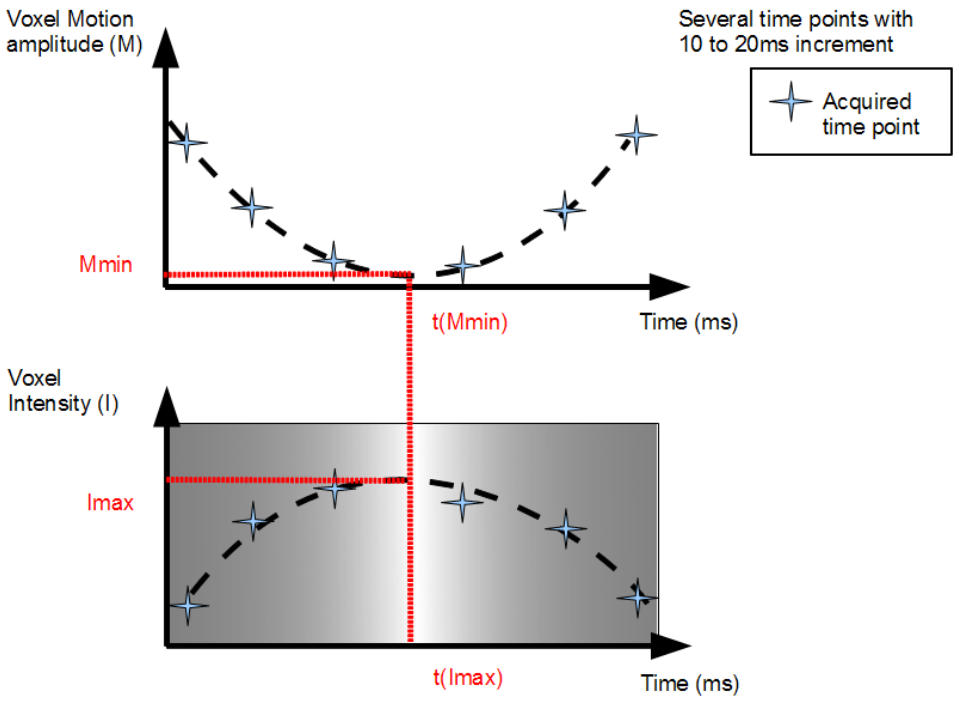

Figure 45: Time-Maximum Intensity projection (TMIP) principle to access motion-less diffusion-weighted signal intensity with trigger-shifted acquisitions

To gather sufficient amount of data sets as well as to cover the whole optimal time-window, the minimum number of time-shifted repetitions was defined as 5 and the maximum affordable number of repetitions in a reasonable context was 15, though we always focused on a maximum of 10 repetitions for potential translation to patients' examination. As our volunteer's study showed previously, the optimal time-window does last only about 100-150ms, and even less in the case of patients of severe conditions or for big animals such as pigs. Thus depending on the subject's heart rate, trigger shift should be adapted from 5 (pig) to 15ms (calm sportive volunteer). In our experience ten 10ms-incremented repetitions from initial trigger starting at mid diastole proved to increase the reproducibility of least-motion induced DW-images acquisitions without much input from the user.

2.7.2. Non-rigid Registration

However being able to retrieve the maximum intensity pixel-wise among 10 repetitions requires the images to be registered first. Indeed bulk motion varies from one heart beat to another. Bulk motion mis-registration is even greater with images acquired at different phases.

Non-rigid registration was delegated to P.Kellman and performed as rigid registration proved insufficient in compensating local myocardium wall motion such observed in the figure below. Non-rigid registration was performed using a dedicated algorithm developed for real-time cardiac imaging and matured through several years of practice (Chefd'hotel et al. 2002; Chefd'Hotel, Hermosillo, et Faugeras 2001; Kellman et al. 2008; C. Chefd'hotel et al. 2004).

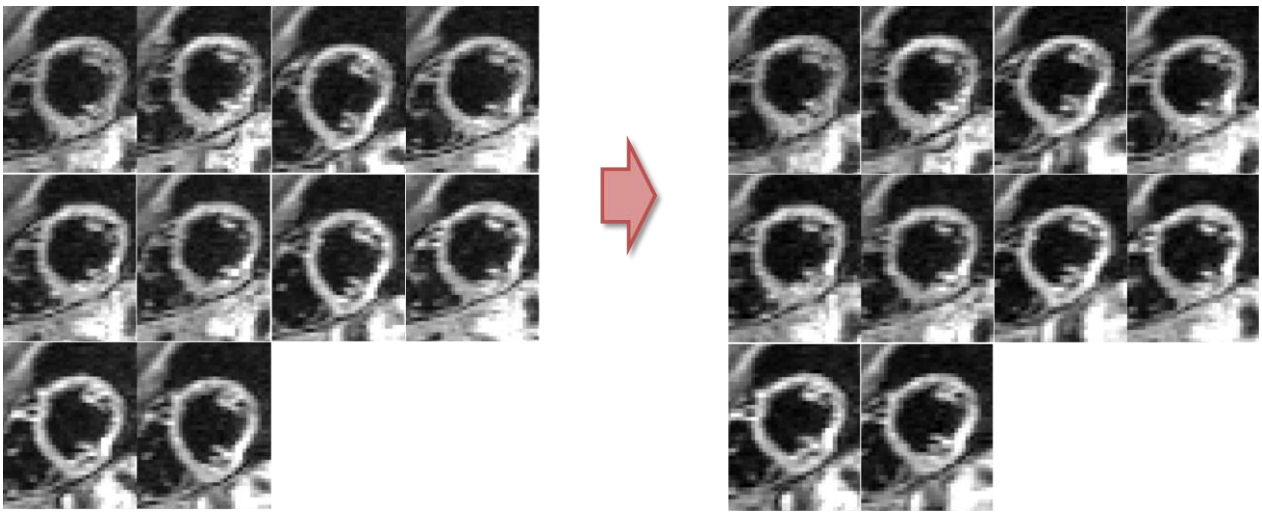

Figure 46: Non-rigid registration results (shown for b=100 s/mm² DWI images) on a volunteer's DWI data set (10 repetitions). Both bulk motion and local wall deformation are well compensated.

Since the registration results outperformed our expectations, ***our acquisitions were performed free breathing to relieve acquisition set-up*** limitations:

- to reach higher repetition numbers (10 repetitions) without the need of multiple breath holding or to teach breathing synchronization to subjects.
- to enable DWI exploration of even patients of severe conditions, not able to withstand breath holding.

Therefore further in vivo DWI data are acquired free breathing in both volunteers and patients and bulk motion is compensated with non-rigid registration.

Material

The study enrolled several volunteers (4 females/11 males, ages 27-54, heart rate (HR) 58-77 bpm) that gave informed consent to the study protocol.

Experiments were conducted on two similar 1.5T clinical scanners (MAGNETOM Avanto, Siemens, Erlangen, Germany) with a maximum gradient strength of 40 mT/m and maximum slew rate of 200 mT/m/s.

Data sets were compared in terms of mean myocardium signal intensity (<SI>) and signal-to-noise ratio (SNR) defined as:

$$SNR(b) = \frac{< SI(b) >}{Noise(b)} \qquad \text{(XLII.)}$$

where "< >" denotes the mean over the left ventricular wall and *Noise* was measured by the standard deviation of pixel intensities in a signal-void region of the DW image.

2.7.3. TMIP initial results with home-made sequences

As stated before, the first and foremost consequence from trigger-shifted acquisitions strategy and TMIP processing was a significant ease during acquisition. Trigger definition is not required as precise as a single-trigger multiple-repetitions would be in order to obtain two or more (out of 10) intense DW-images of the myocardium. And with the TMIP processing to extract the greatest intensity out of the 10 repetitions, the approach provides DWI acquisitions robust to cardiac motion.

Our first initiative was to work on a new sequence dedicated to in vivo cardiac DWI so that we could control the full acquisition process.

2.7.3.1. Spin-echo EPI sequence

A single-shot spin-echo echo-planar (EPI) DWI sequence was developed similar to Gamper et al. (Gamper, Boesiger, et Kozerke 2007). Both monopolar and bipolar gradients, enabling to compensate for first order motion and flows, were investigated. Bipolar gradients did not prove significant benefits experimentally while monopolar gradients enabled very small echo time (TE). Also to reduce TE even further and guaranty maximum signal intensity at k-space center line, an EPI centered-out readout scheme was applied to read k-space. Eddy-current distortions were compensated with a gradient lobe before excitation (Alexander, J. S. Tsuruda, et D. L. Parker 1997). Other parameters were FOV of 281.6 x 70.4 mm² with inner volume excitation, in-plane resolution of 2.2x2.2 mm², slice thickness of 3.5mm, matrix size of 32x128 and 5 time points per heartbeat. This enabled TE values to drop to small times:

Max b value (s/mm²)	Min TE (ms)

100	25.7
200	29.6

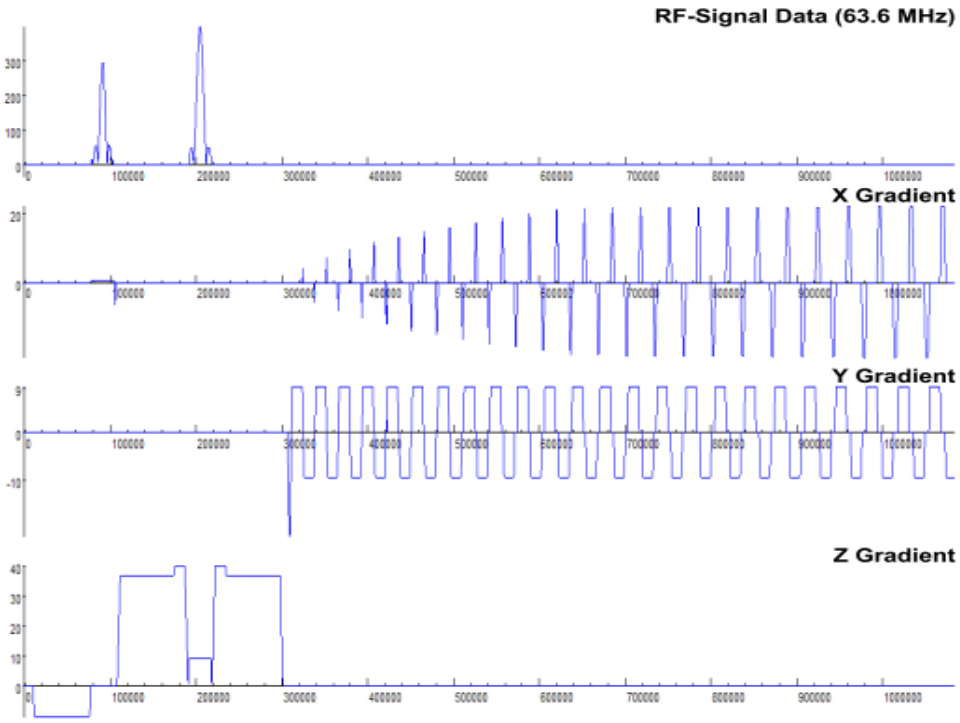

Figure 47: Time diagram for our spin-echo (SE) centered-out EPI diffusion weighted sequence. Diffusion encoding occurs in this diagram in the z direction.

Complete data set included two diffusion weightings: b = 50 and 200s/mm² (so TE=29.6 ms) over 3 diffusion encoding directions each. No b=0 reference image was acquired at that point because of registration issue between b=0 and b>0 images, which have inverted blood-myocardium contrast (blood pool is hyper-enhanced in b=0 but hypo-enhanced in b>0 because of flow-induced diffusion weighted signal-loss). TR was set to 2 heartbeats, allowing sufficient time for signal recovery. Acquisitions were triggered during diastole in the optimal time-window predefined with a cine acquisition. Five 15 ms-shifted repetitions were acquired within optimal diastolic time-window.

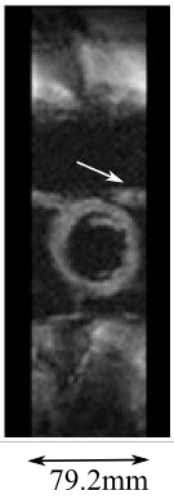

Figure 48: Spin-echo centered-out EPI DW image. FOV was increased to 36 encoding lines. Aliasing occurs (white arrow): right ventricular features appear on both sides.

Because EPI is very sensitive to off-resonance effects (Jezzard et R S Balaban 1995), Field-of-view (FOV) was highly limited in the phase-encoding direction by aliasing (Figure 48) and spatial distortions. Inner volume excitation proved insufficient to compensate for aliasing without penalizing signal intensity in the image. Left ventricular hardly fitted in the FOV (see Figure 49), requiring two data sets to cover for the whole myocardium.

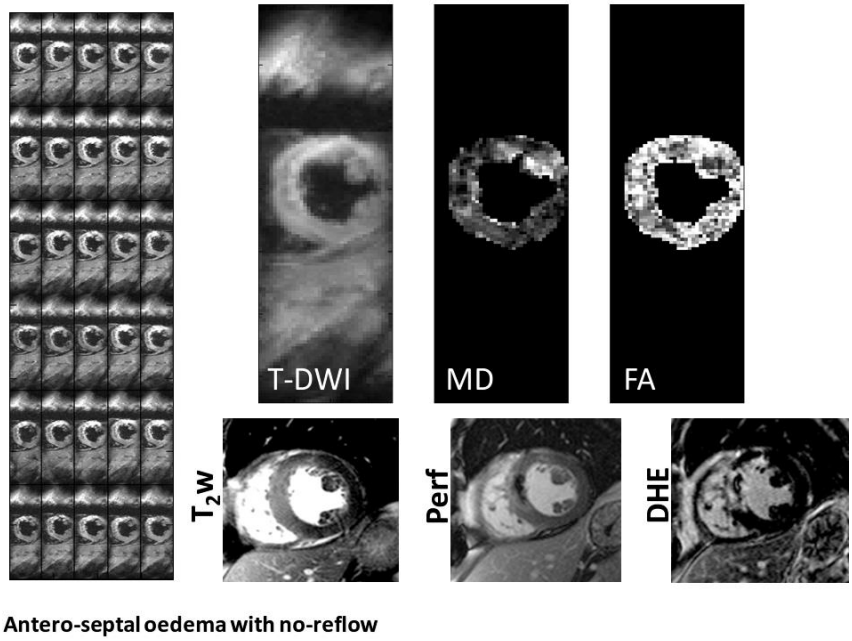

Figure 49: Patient with antero-septal post-infarct scar. TMIP results using home-made ss-DWI-EPI sequence. Left: 2 b values (5, 200 s/mm²) x 3 direction x 5 repetitions are shown. Top: TMIP trace-diffusion weighted image (b=200) (T-DWI), mean

diffusivity(MD) and fractional anisotropy(FA). Bottom: Reference CMR imaging (T2weighted-CMR, Perfusion imaging and Delayed hyper-enhancement). Field-of-view is very limited in the phase encoding direction.

This EPI-DWI sequence, although of rather interesting since attempts in patients were showing promising contrast (Figure 49), resolution and TE, was not satisfactory enough. Therefore we investigated other possible acquisition schemes.

2.7.3.2. Diffusion-preparation b-SSFP-DWI sequence

Note: This sequence was mostly developed by my colleague Vinay M. Pai. I myself tweaked few parameters with his help (diffusion encoding schemes such as tensor encoding, bipolar diffusion encoding gradients, various k-space ordering options) and mastered the concept as to optimize parameters during acquisitions but I may not claim the paternity of this development.

The idea of a diffusion preparation is an option of interest (Jeong et al. 2006; Stöcker, Kaffanke, et Shah 2009). A new sequence was developed with a diffusion preparation. As for reading k-space, we opted for an acquisition scheme more robust to spatial distortions: diffusion preparation was combined with a balanced steady-state free-precession (b-SSFP) (Carr 1958) space reading scheme.

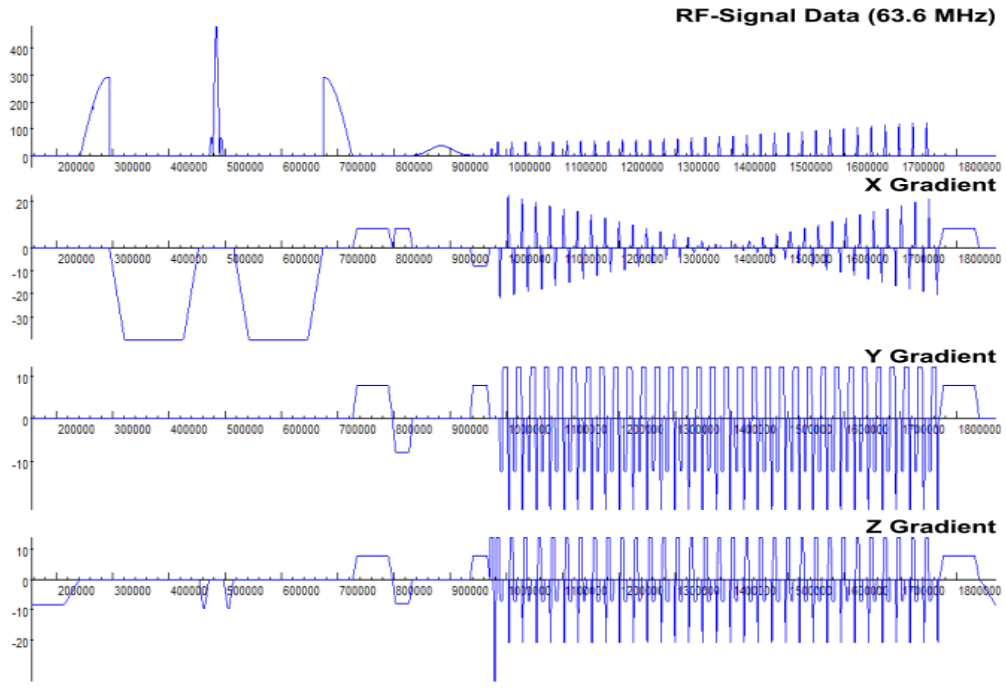

Figure 50: Time diagram for the diffusion-preparation balanced SSFP DWI sequence developed. Diffusion encoding occurs in the x axis.

Balanced-SSFP RF flip-angles were ramped-up to compensate for low magnetization induced signal loss (Le Roux 2003). Imaging parameters were TE=1.5ms, TR=2*TE=3ms, flip angles ranging 15° to 80°, matrix size of 124x164, 2.3x2.3x6mm3 voxel size. Complete data set included b=0 reference image and two diffusion weightings: b = 50 and 200s/mm² over 3 diffusion encoding directions each. Global repetition time was set to 2 heartbeats, allowing sufficient time for signal recovery. Acquisitions were triggered during diastole in the optimal time-window predefined with a cine acquisition. Five 10 to 15 ms-shifted repetitions were acquired within optimal diastolic time-window.

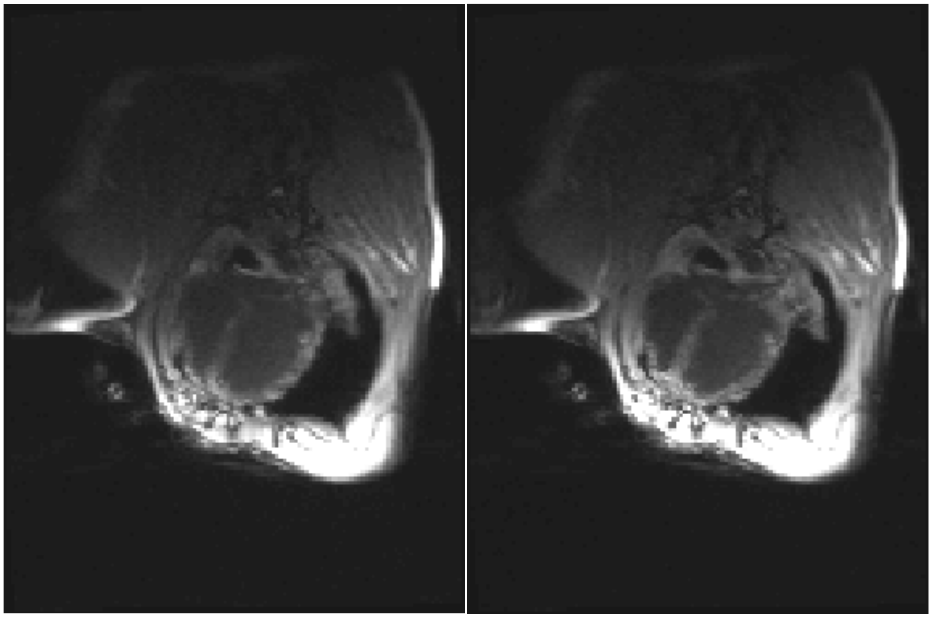

Figure 51: DWI results in a pig using our b-SSFP sequence. Trace-DWI (b=50(Left) and 100(Right) s/mm²) are completely ***aliasing free****.*

Results proved the absence of aliasing or spatial distortions. However the technique is highly sensitive to off-resonance artifacts, due to inhomogeneity in the main magnetic field related to susceptibility variation, which impacts SSFP signal with banding artifacts.

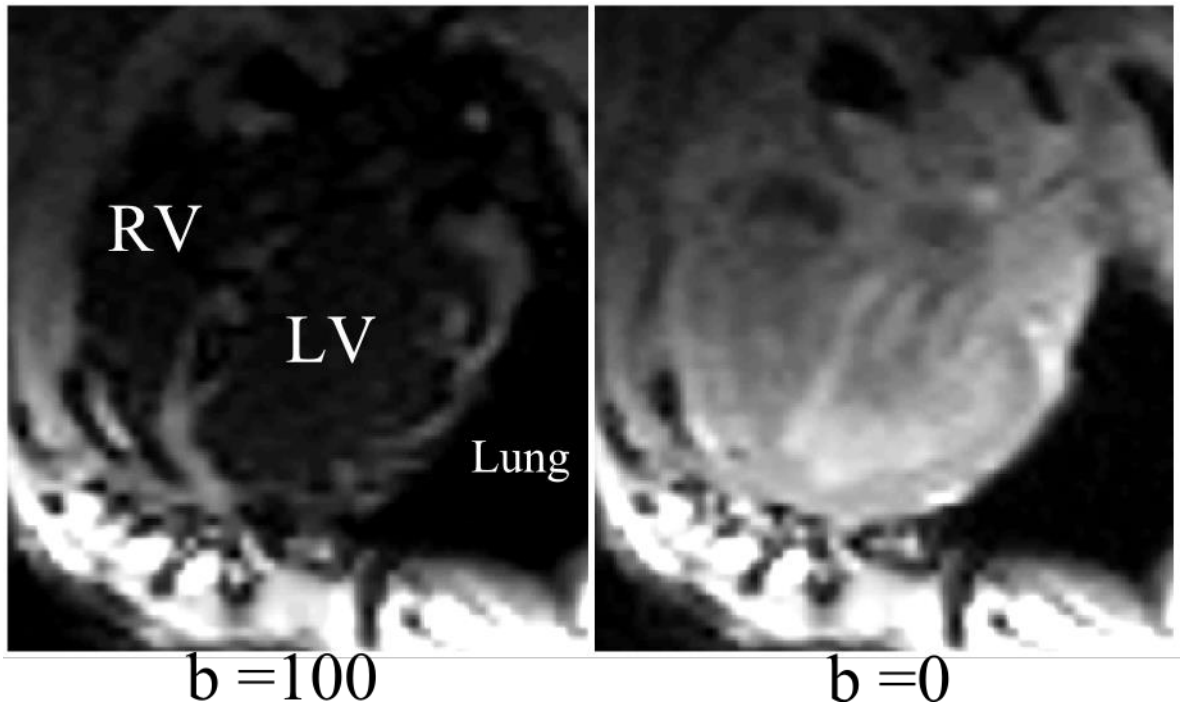

Figure 52: 4-chambers DWI results in a pig with the diffusion-preparation b-SSFP DWI sequence. ***Left****: b=100s/mm² diffusion weighted image.* ***Right****: b=0 image. Characteristic b-SSFP banding artifact is visible across the rib cage as well as across the myocardium in the DW-image (left).*

A RF phase-cycling was experimented (Elliott et al. 2007) for tip-down(+90°) and tip-up (-90°) pulses but since banding artifacts are not spatially stable in the myocardium, phase-cycling did not help remove the banding artifacts

.

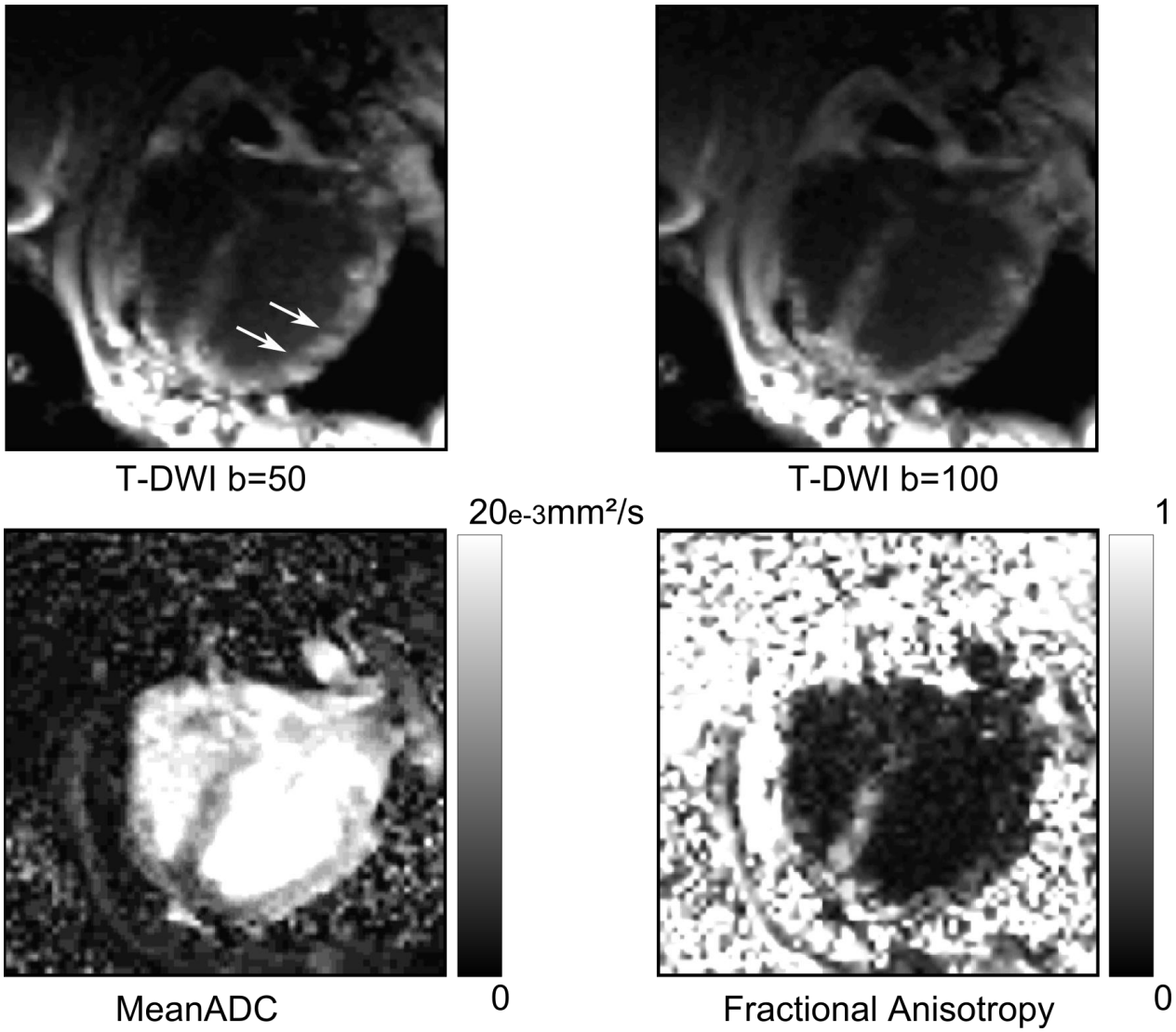

Figure 53: TMIP results with b-SSFP sequence and a diffusion preparation. Top: Trace-DWI (b=50, left, 100 s/mm², right). Bottom: mean ADC map (left) and FA map (right).Banding artifacts are still observed in the myocardium.

TMIP could have been a solution for removing dark-bands but experiences proved (

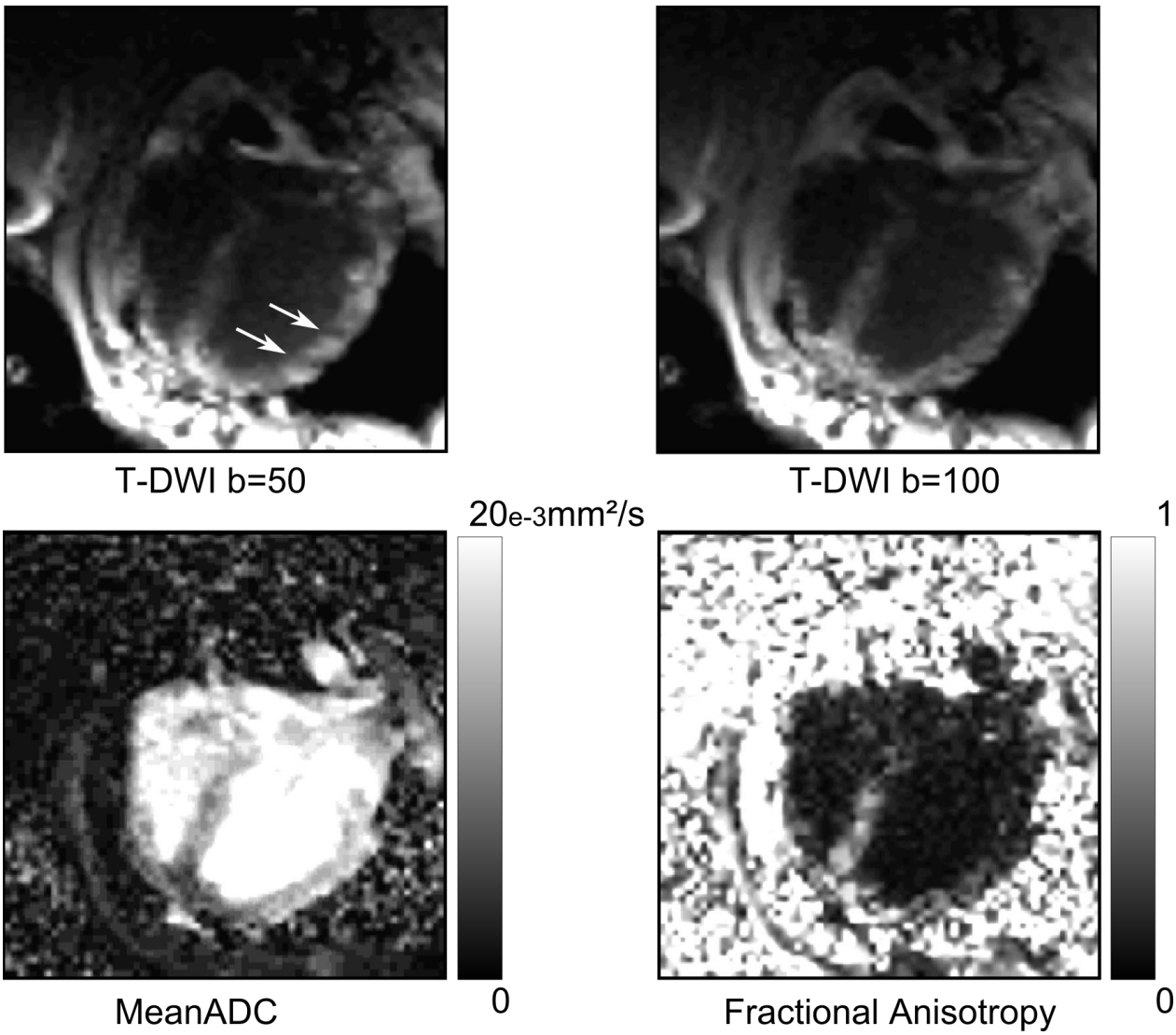

Figure 53) too many banding artifacts occurs in diffusion weighted images because of motion and diffusion encoding increasing off-resonances effects. Also the use of numerous RF pulses generates a great energy deposit for each image, thus the long-term SAR increases rapidly and repetitions number is limited since.

Thus this promising sequence proved inappropriate in this form for *in vivo* cardiac DWI.

2.7.4. TMIP initial results with product sequence

The available state-of-the-art DWI sequence available on our clinical scanner was optimized for fast single-shot cardiac imaging and appreciated relatively to previous issues from dedicated developed sequences.

Protocol parameters

Diffusion weighted imaging was performed with a single-shot, twice-refocused spin-echo EPI sequence available on the clinical scanner (T.G. Reese et al. 2003). Acquisition parameters were: imaging matrix of 128x160 with isotropic in-plane resolution of 2.6x2.6mm² and slice thickness of 6 mm, GRAPPA (Griswold et al. 2002) parallel imaging acceleration of rate 2, echo time (TE) of 51 ms, diffusion weighting b values of 0, 50 and 100 s/mm^2, and 3 orthogonal diffusion encoding directions for each non-zero b-values. Acquisitions were ECG-triggered at every 2 or 3 heart beats depending on subject heart rate to ensure that TR ≥ 2 sec. An initial dummy scan was used to reach a signal decrease-recovery steady state. Two mid-ventricular slices were acquired in each volunteer.

Results

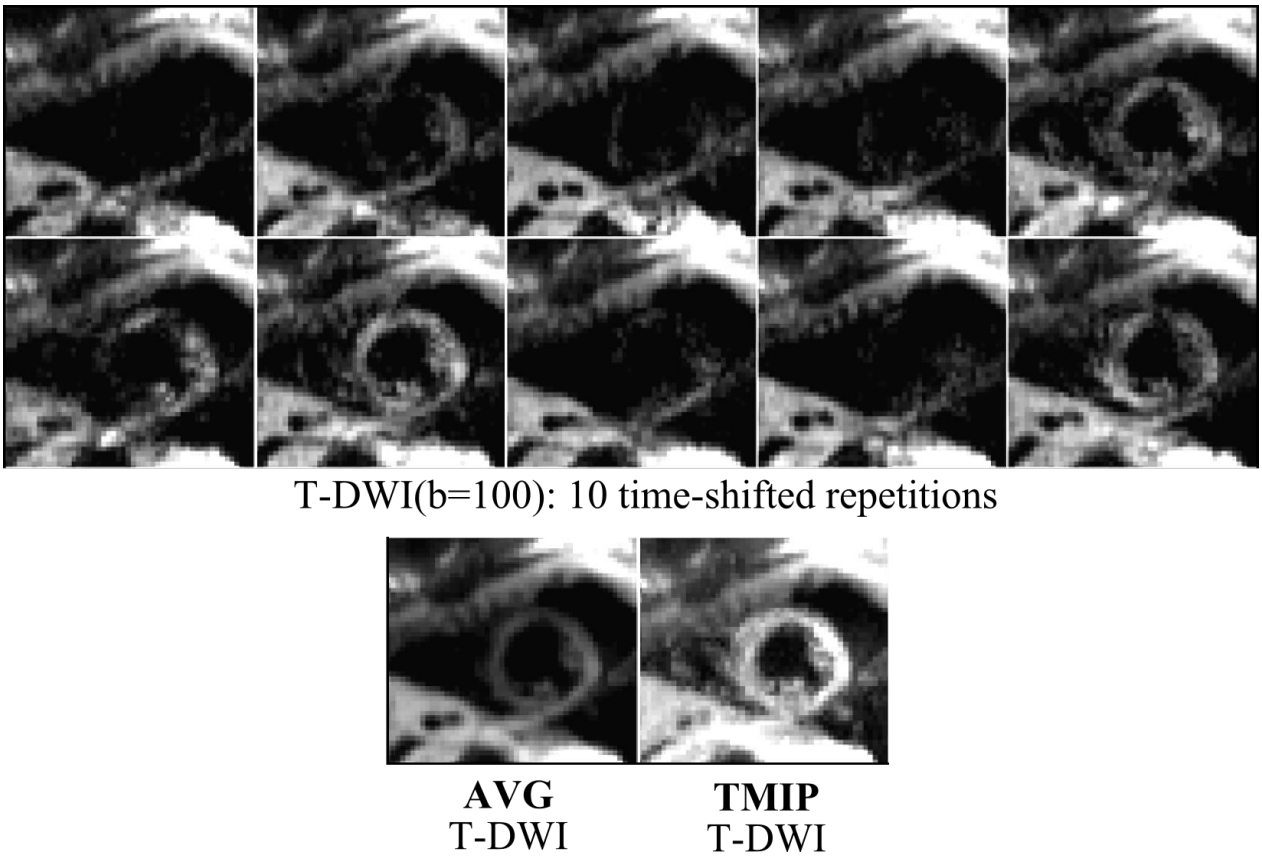

Figure 54: Trace-DWI (b=100 s/mm²) from a short axis slice of a volunteer heart. ***TOP****: 10 time-shifted (10 ms shift) repetitions.* ***BOTTOM****: Image averaging (AVG) T-DWI(Left) and TMIP T-DWI (Right). The sliding acquisition window provides at least 2intense images of the myocardium out of 10 and reveals the short span of the time-window for optimal capture of the moving heart (3 consecutive intense DW-images = between 30 to 50 ms here).*

Signal intensity (SI) loss was greatly reduced compared to usual pixel-wise images averaging (AVG). From the 10 data sets (5 volunteers x 2 slices), myocardium mean SI (<SI>) was increased by 37% for b=0, 84% for b=50 and 108% for b=100 s/mm². The SI benefits of TMIP are increasing with the b value (2-ways ANOVA: $p<0.05$).

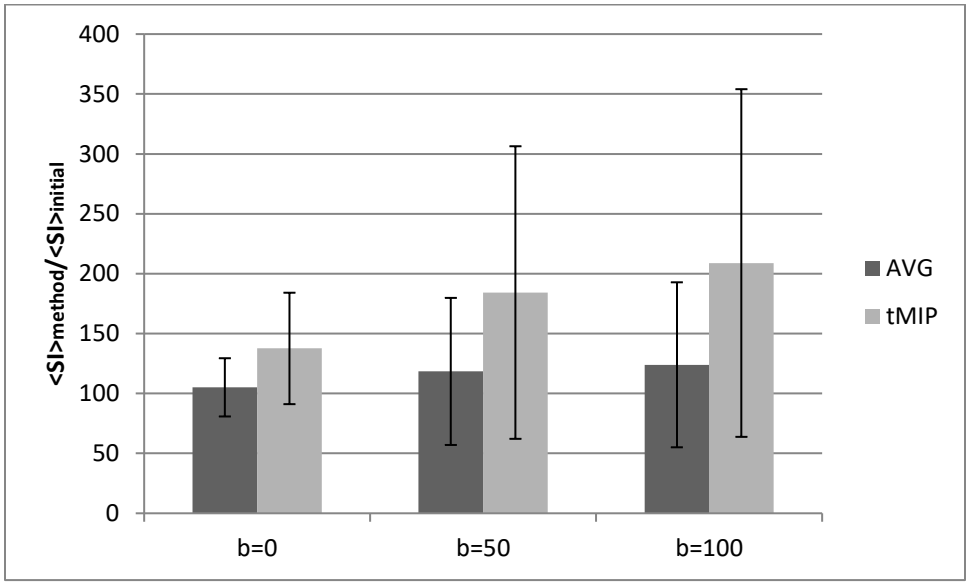

Figure 55: Image averaging (AVG) and TMIP myocardium signal intensity (SI) benefits from initial DW-images data set for each b value.

Discussion and limitations

Results confirm the recovered myocardium intensity with TMIP increases with b values. Since motion-induced signal-loss increases with b values, TMIP results suggest that the compensated signal-loss might indeed be motion-related.

However figure 31 shows how resulting TMIP DW-images remain heavily spoiled with noise. SNR measurements confirmed that TMIP suffers a high noise-level while AVG increases significantly image quality: 264%, 274% and 308% SNR increase with AVG for b values of respectively 0, 50 and 100 s/mm² against 155%, 191% and 220% SNR increase only with TMIP.

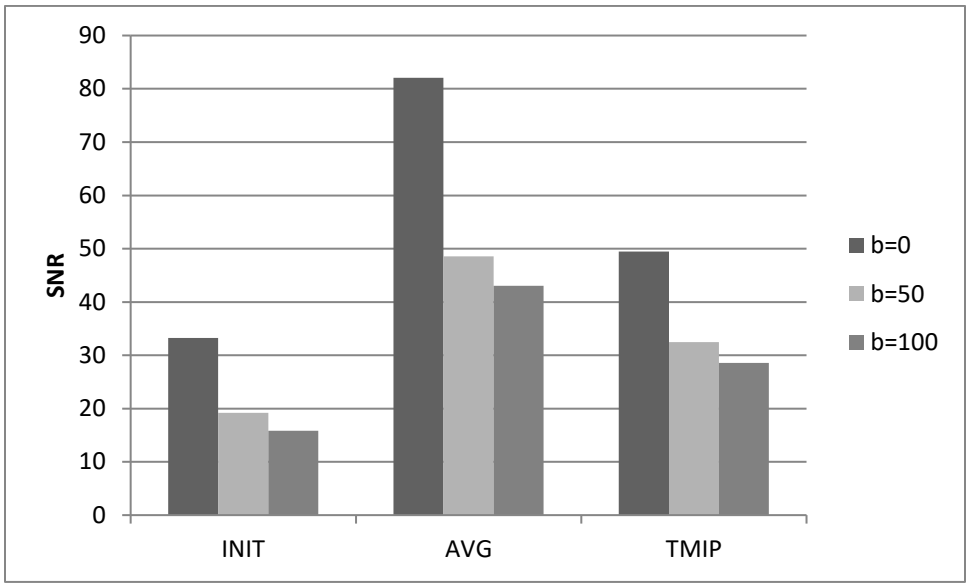

Figure 56: Signal-to-Noise Ratio (SNR) for DW-images depending on b-value and image processing method: initial data sets (INIT), image averaging (AVG) and time-MIP (TMIP).

Therefore TMIP appears to significantly reduce motion-induced signal-loss but suffers a high noise level. Moreover a validation of motion-induced signal-loss reduction by TMIP would help understanding the mechanisms of DWI for cardiac imaging.

2.8. PCA-TMIP-DWI: improving robustness and accuracy

In order to improve image quality by benefiting of all the repetitions without impacting on the motion-induced signal variations, a dedicated image filtering was proposed. Localized principal component analysis (PCA) decomposition was applied to remove background noise prior to TMIP projection.

2.8.1. PCA filtering

2.8.1.1. Image processing theory

The basic assumption behind PCATMIP is that motion-induced signal loss is spatially smooth except when crossing boundaries between anatomical compartments. Under this assumption, the temporal behavior of the image intensity in a small neighborhood can be described by one or two (as many as the number of compartments inside a sliding boxcar) leading principal components (PC) whose amplitudes

(eigenvalues) are much greater than the other components. Specifically, we denote the DW image intensity of the *i*th repetition as *I* (*i, x, y*), and for a 2D boxcar of size ***S*** *x* ***S*** centered at pixel (*p, q*) we calculate the autocorrelation matrix among the repetitions:

$$M_{ij} = \sum_{|x-p|<S/2,|y-q|<S/2} I(i,x,y)I(j,x,y) \qquad \text{(XLIII.)}$$

Then the matrix is diagonalized to obtain eigen vectors $V_n(i)$ and corresponding eigen values E_n. The n^{th} principal component is then defined for pixels in the boxcar as

$$P_n(x,y)\Big|_{|x-p|<S/2,|y-q|<S/2} = \sum_i I(i,x,y)V_n(i). \qquad \text{(XLIV.)}$$

Next we select the PCs corresponding to eigenvalues above a threshold ***Et***, and reconstruct PCA-filtered intensity values in the box using these PCs:

$$I'_{pq}(i,x,y)|_{|x-p|<\frac{S}{2},|y-q|<S/2} = \sum_{E_n>E_t} P_n(x,y)V_n(i) \qquad \text{(XLV.)}$$

This process is repeated through a sliding box process, where the center *(p, q)* of the boxcar is moved over the entire image at one pixel increments. In doing so, each pixel (*x, y*) is covered by many boxes, and each box generates a set of filtered intensities $I'_{pq}(i,x,y)$. These are combined in a weighted sum to yield the final PCA filtered image intensity for pixel (*x, y*) and the *i*th repetition:

$$I_{PCA}(i,x,y) = \sum_{p,q} w(x-p,y-q)I'_{pq}(i,x,y) \qquad \text{(XLVI.)}$$

where the weight ***w*** decreases with increasing distance between (*x, y*) and (*p, q*).

The two key parameters in the PCA process are the size of the sliding box *S*, and the eigenvalue threshold *Et*. The box size should be sufficiently small such that no more than two compartments are included, thus two PCs are needed to describe the intensity fluctuations in the box, but large enough so that the error in the PCA filtered intensity approaches the theoretical level of:

$$\text{Error in PCA filtered intensity} \approx \sqrt{\frac{\text{number of included PCs}}{\text{number of repetitions}}} * (\text{noise level in a single image}) \quad \text{(XLVII.)}$$

The eigenvalue threshold *Et* should be set high enough to reject the PCs corresponding to pixel-wise random noise, and low enough to include the PCs from global intensity fluctuations caused by motion. Both parameters were determined by numerical simulations based on the SNR level of actual DW images.

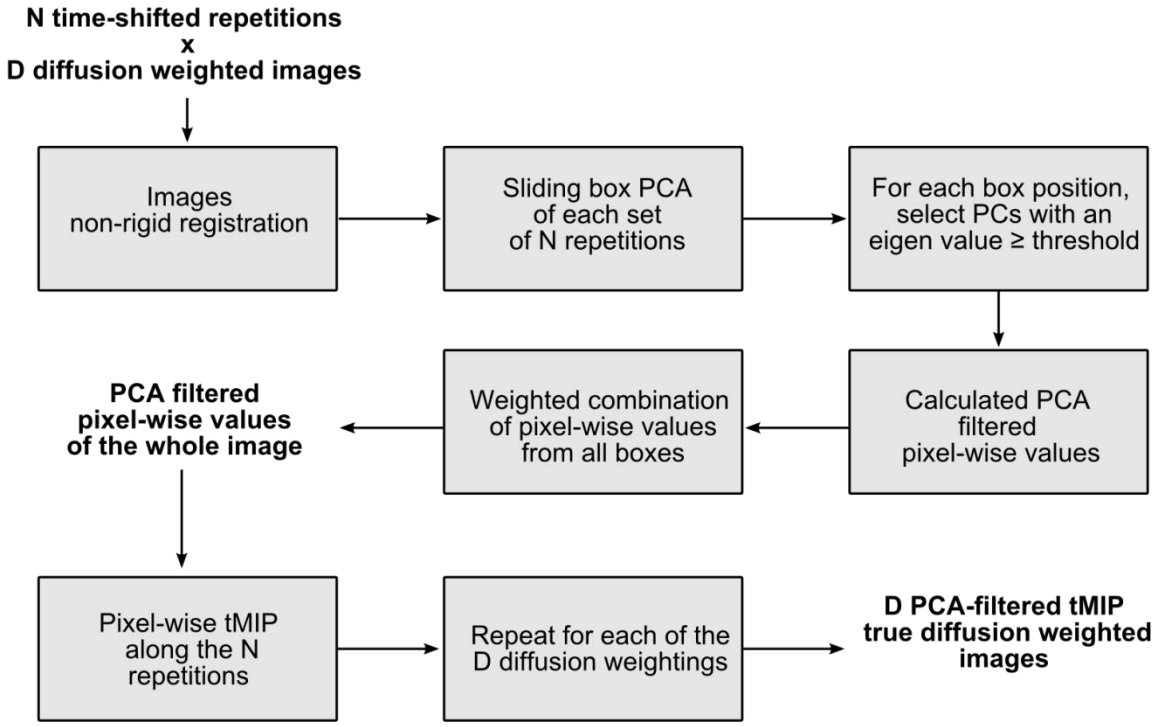

Figure 57: Block diagram of PCATMIP processing flow. Blocks represent processing steps and outputs are shown in bold. Transferred data is symbolized by arrows connecting blocks.

In the last step, the PCA-filtered images were then subject to TMIP to yield a single DW image for each diffusion weighting and gradient direction:

$$I_{PCATMIP}(x,y) = (\text{MIP along repetition i})\left[I_{PCA}(i,x,y)\right] \quad \text{(XLVIII.)}$$

Given observed SNR in our volunteers experiments, the optimal box size was 15 pixels, and the optimal threshold *Et* = 40*(average of E_3 to E_{10}).

2.8.1.2. PCA optimization

Material and method

Volunteers' data sets were processed with our dedicated PCA algorithm and SNR benefits were compared from raw initial DW-images.

Number of significant principal components (PC)

A set of 12 volunteer's DW-images was studied for illustrating the impact of the size of the sliding box *S*, and the eigenvalues threshold *Et* on reconstructed intensity-fluctuation corrected DW-images.

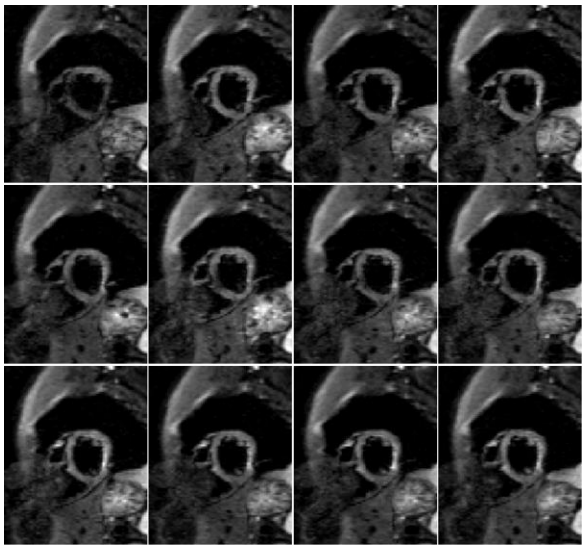

Figure 58: Original volunteer's data sets after bulk motion registration.

A sliding box of variable size (S=3, 9 and 15) was used initially to decompose the 12 images data sets into 12 principal components. The amount of information held by each component can be determined by their corresponding eigenvalue:

$$Inf(j) = 100 * \frac{E_j}{\sum_{i=1} E_i} \qquad \text{(XLIX.)}$$

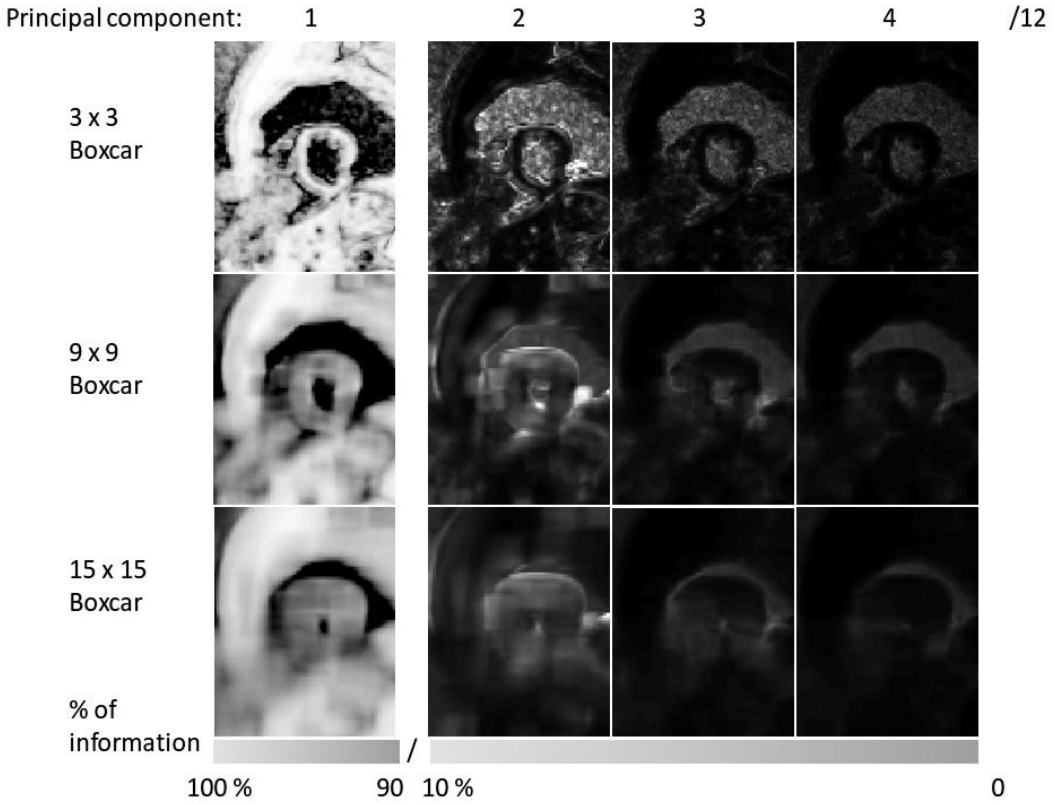

Figure 59: Information content for the 4th first principal components (PCs) of our volunteer's data set. Scales have been distinguished for the first PC and the others because of the gap of information content.

Figure 58 shows that the first component holds most of information (>90%) but in the signal void regions (lungs here). The first component overcomes the others by far, regardless of the boxcar size *S*. The second component has high eigenvalues only at tissue interfaces, where motion manifests the most, and in the background noise where pixels' signal is less correlated from one image to the other. Thus only few, from 1 to 2, components are useful for the PCA projection and the reconstruction of noise-spikes less images.

Simulations with a 3-compartments digital phantom

A 3-compartments phantom was produced for simulations of PCA processing impact in the presence of physiological motion.

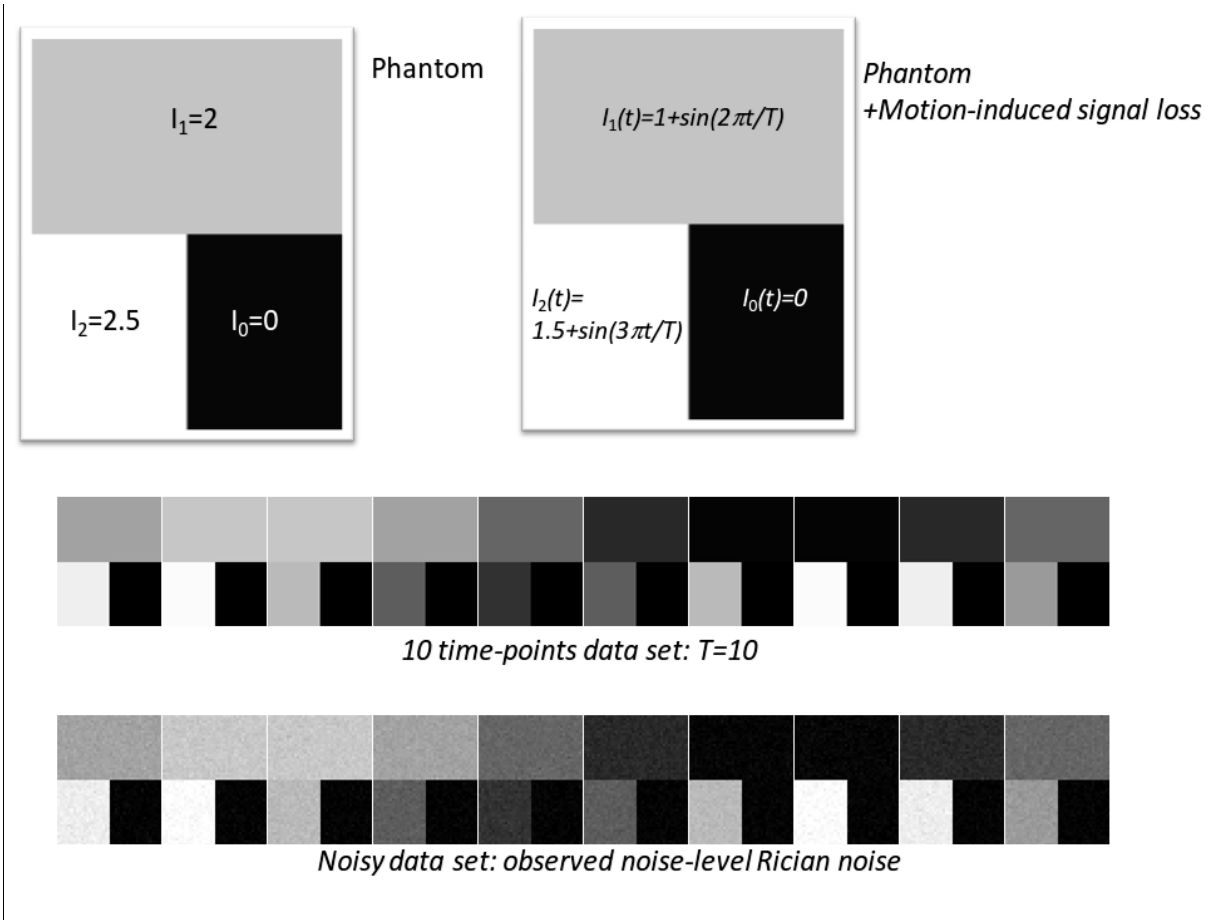

Figure 60: Simulation phantom to represent 3 compartments in the presence of motion-induced signal loss and noise. Rician noise level was lifted to observed experimental noise level.

Evaluation of boxcar size and noise threshold influence on PCA results was performed on signal-to-noise ratio (SNR) and contrast-to-noise ratio (CNR) defined as below:

$$SNR = \frac{< I_2 >}{stdev(I_O)} \quad \text{(L.)}$$

$$CNR = \frac{< I_2 > - < I_1 >}{stdev(I_0)} \quad \text{(LI.)}$$

The boxcar size proves to be a major parameter in the PCA processing. Too large boxcars include several components, thus reducing the capacity of PCA decomposition to differentiate noise from motion-induced intensity variations. But with too small boxcars, PCA does not separate correctly noise from slower intensity variations. Using an eigenvalue threshold E_t of 40, the optimal boxcar size from simulation appears to range between 5 to 15 pixels.

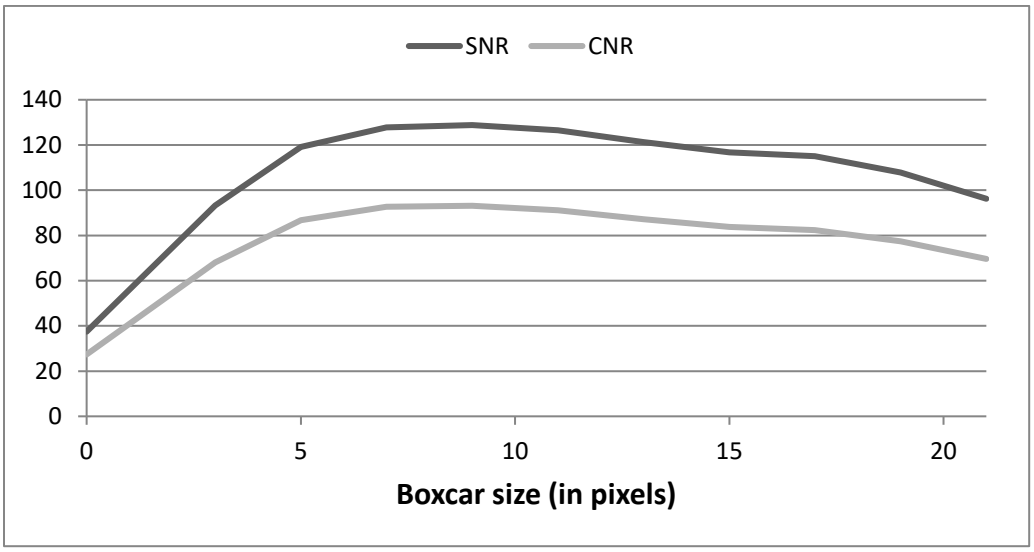

When combined with TMIP, the PCA boxcar size minimizing the error in PCA filtered images (eq. p86) was found to be 15 (Vinay's MRM paper reference when published). The boxcar size is deeply related to the pixel spacing used in imaging protocol. The boxcar should include enough pixels to separate pixel-wise intensity variations (=noise) to organ-wise intensity variations (=motion). However if too many compartments/organs are included in the boxcar, the number of significant PC will increase and some PC might be discarded as noisy variations.

The PCA noise threshold E_t stands for the threshold to separate noise from slow intensity variations related to physiological motion. If E_t is low, then the first component verifies: $E_1 > E_t * average(E_2:E_{10})$ and the next PC are discarded; however is E_t is high, then none component verify $E_n > E_t * average(E_{n+1}:E_{10})$ so that the process of including PC goes to the end (n=10) and includes all components, among which are the noisy components.

Given our phantom study with noise level equivalent to observed b=100 s/mm² SNR (~10), the investigation of noise threshold E_t impact on noise reduction (boxcar size S = 15 pixels) reveals the maximum value E_t can take before including too many principal components (that is including PC related to noise intensity variations).

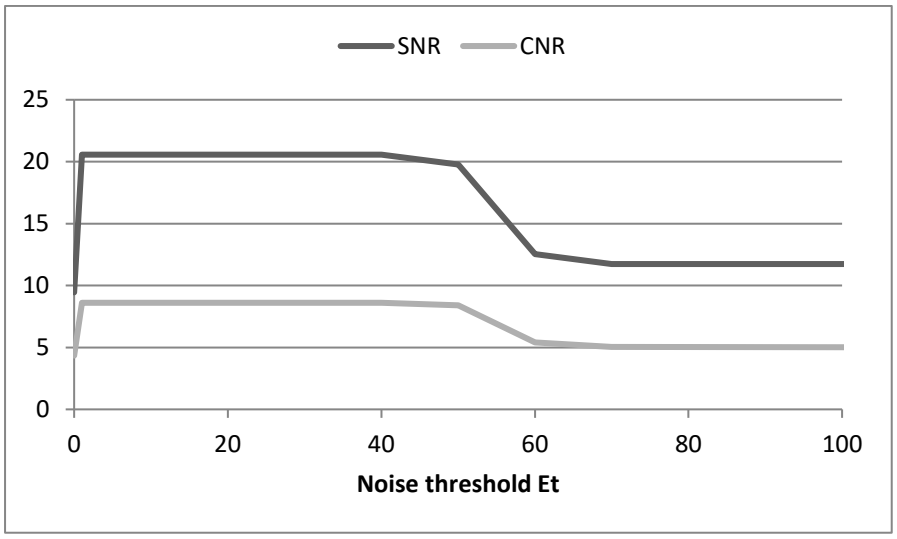

With initial SNR of ~10, if E_t >50 the PCA might reconstruct images using PC representing noise intensity variations. Also for E_t >60, almost all PCs are used, returning images with noise level equivalent to initial image series.

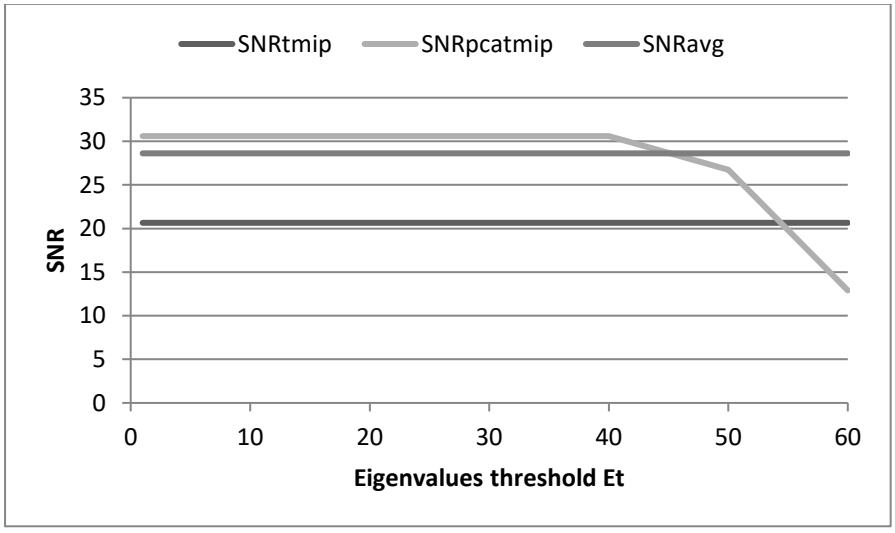

Additional simulations proved PCATMIP to be optimum with E_t=40 and a boxcar size of 15 pixels (Vinay's MRM paper reference). Theoretical results on the phantom show the error ($\epsilon = \frac{I_{method} - I_{real}}{I_{real}}$) to be clearly reduced with PCATMIP (*S=15*, E_t*=40*) when intensity undergoes slow variations.

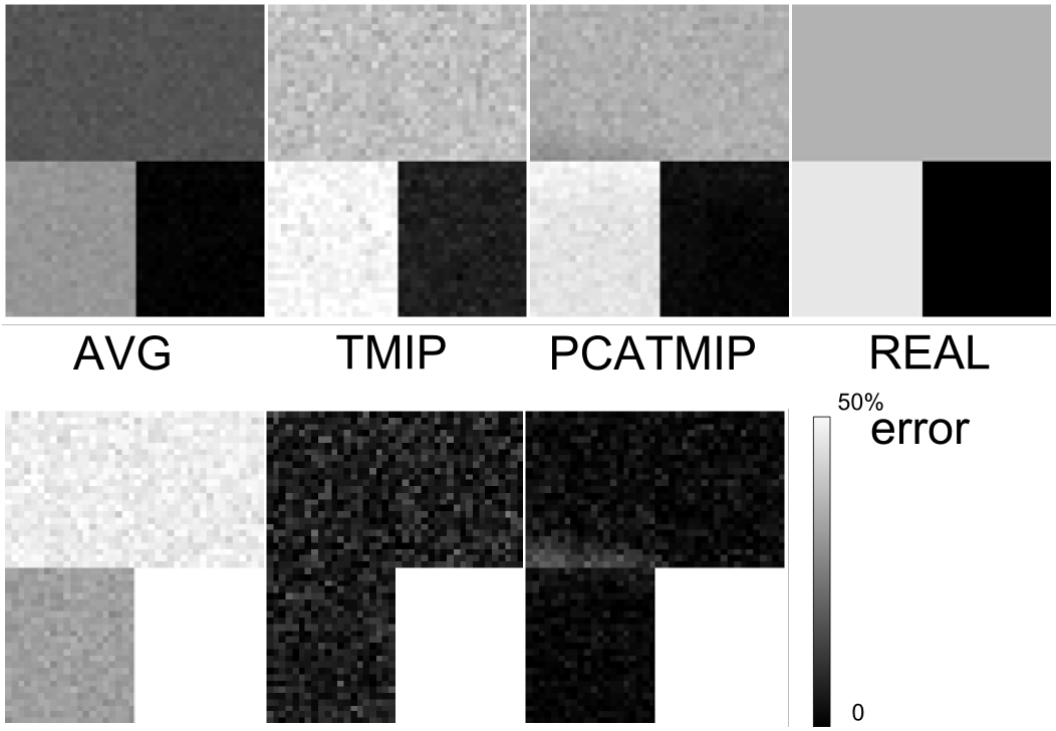

Figure 61: theoretical results of PCATMIP on a 3-compartments numerical phantom. ***TOP:*** *Results are compared to averaging (AVG), TMIP and original data (REAL).* ***BOTTOM****: relative error to the real data is presented for each method.*

The results also show no difference between the 2 filled compartments, confirming that the method will not influence anatomical MRI contrast. While the error is irrelevant in the signal-void compartment (in bright white for all method because of division by 0), the background is only highlighted a little with TMIP alone. PCATMIP preserves the background compartment. Finally PCATMIP appears to increase the 2 compartments interface, adding a small dark band in the lowest compartment. We have not defined the origin of this phenomenon, neither have we been able to reproduce this in different simulations. But this might come from the specific compartments frequency difference employed in this phantom.

2.8.1.3. PCA experimental results

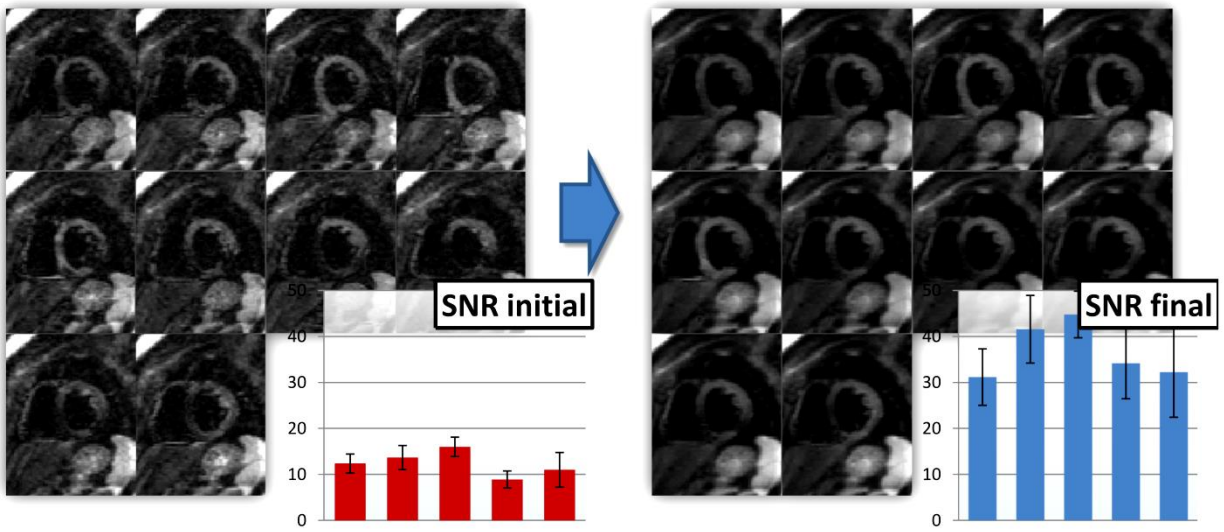

Figure 62: Dedicated PCA filtering increases raw DW-images SNR before TMIP. Results are given for b=100 s/mm² DWI for each volunteer in bar plots and 10 ms-shifted Trace-DWI are shown for one volunteer.

Dedicated PCA algorithm enables a significant increase of SNR by 257 ± 33 % for b=100 s/mm² ($p<0.01$). Moreover the filtering preserves anatomical features edges and myocardium mean intensity does not appear to suffer from the processing either.

2.8.2. PCATMIP

2.8.2.1. Theoretical study of TMIP and PCATMIP on DWI images and parameters

Method

To evaluate TMIP and PCATMIP theoretical benefits in the presence of motion, each method results were compared to pixel-wise images averaging (AVG) in a simulation. A numerical simulation was performed using *in vivo* cardiac 3D-motion measured with motion tracking MRI (displacement encoded with stimulated echoes (DENSE (Aletras et al. 1999))).

Simulation started from homogeneous (D=5 mm²/ms) low b-values (0, 50 and 100 s/mm²) DW image intensity for an eddy-currents distortions compensated twice-refocused spin-echo echo-planar imaging (EPI) sequence (T.G. Reese et al. 2003). Volunteer's DENSE data were used as cardiac motion input for the simulation.

Numerical low b-values DW images were simulated with and without motion-related signal loss using 3D displacement fields obtained from a volunteer's DENSE(Aletras et al. 1999) acquisition. Displacement fields were acquired during the optimal diastolic time-window. Motion-induced data sets were then added Rician noise equivalent to experimental observations. Eventually AVG, TMIP and PCATMIP methods were applied to simulated data sets and compared to initial data on their DW signal intensity (SI), images' SNR and ADC estimation.

DW image SNR was evaluated still as $SNR(b) = \frac{< I(b) >}{Noise(b)}$ where "< >" denotes the mean over the left ventricular wall and *Noise* was measured by the standard deviation of pixel intensities in a signal-void region of the DW image.

Trace DW image (T-DWI) intensity for a diffusion weighting *b* was defined (Chun, Uluğ, et van Zijl 1998) as the geometrical DW intensity over the 3 orthogonal directions:

$$T - DWI(b) = \sqrt[3]{DWI(b, XX) \bullet DWI(b, YY) \bullet DWI(b, ZZ)}. \qquad \text{(LII.)}$$

Mean ADC values (ADC_m) were computed and compared for each method across the whole myocardium.

Results

.

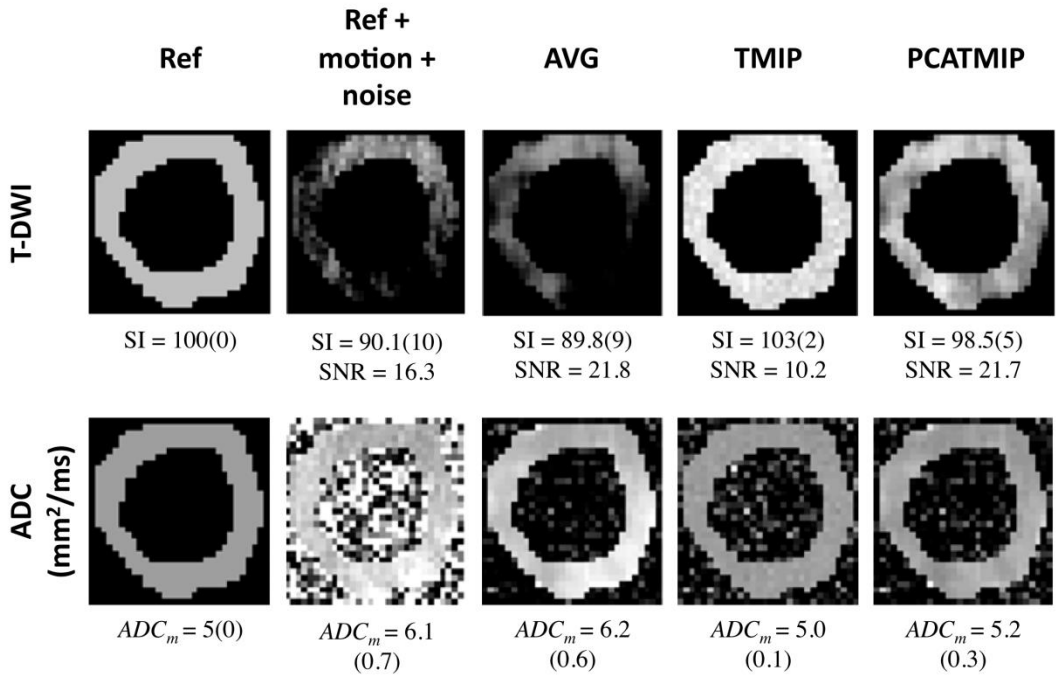

Figure 63: Theoretical impact of image processing approach on DWI simulated with volunteer's physiological motion. TOP: trace-DW images (T-DWI) (b=100 s/mm²): reference, realistic motion-induced data, images averaging (AVG), TMIP and PCATMIP results. BOTTOM: mean ADC (ADCm) estimation maps corresponding to each data set. Simulation sampling was limited by DENSE resolution (3.5x3.5mm²). Values are mean(sd).

Results from the simulation of realistic DW images (i.e. with cardiac motion measured from a DENSE acquisition) show that TMIP and PCATMIP processing can properly reduce the impact of cardiac motion (fig. 36 Top). Figure 3 reveals a heterogeneous pattern of signal loss due to motion throughout the myocardium, since motion and torsion are indeed inhomogeneously distributed. This leads to inhomegeneous ADC_m map when no adequate post-processing is performed. TMIP offers a reduction of motion-induced signal loss and minimizes ADC estimation error (0.1 mm²/ms) as does PCATMIP (0.3 mm²/ms) compared to averaging (1.1 mm²/ms). Homogeneity of ADC maps is also recovered which is critical to separate accurately compartments with pathology-related modified diffusion. PCATMIP also provides DWI images with improved SNR (21.7 compared to 10.2 for TMIP) (fig. 3). PCATMIP low *b* values DWI significantly reduces captured myocardium motion and retrieves initial ADC information with limited quantitative bias (6%).

2.8.2.2. In vivo results

A typical volunteer data set is represented below (Figure 64). The trace-DWI were computed for each 10 ms-shifted repetitions as well as for processed datasets (AVG, TMIP and PCATMIP). Both

appropriate trigger difficulty and important noise are visible here. The consequence of image processing are a penalizing signal-loss for AVG, a high-level speckle-like noise for TMIP and a relative compromise for PCATMIP that benefits both TMIP signal-loss recovery and noise reduction from PCA-based filtering. In this example, the PCATMIP method is clearly the best option.

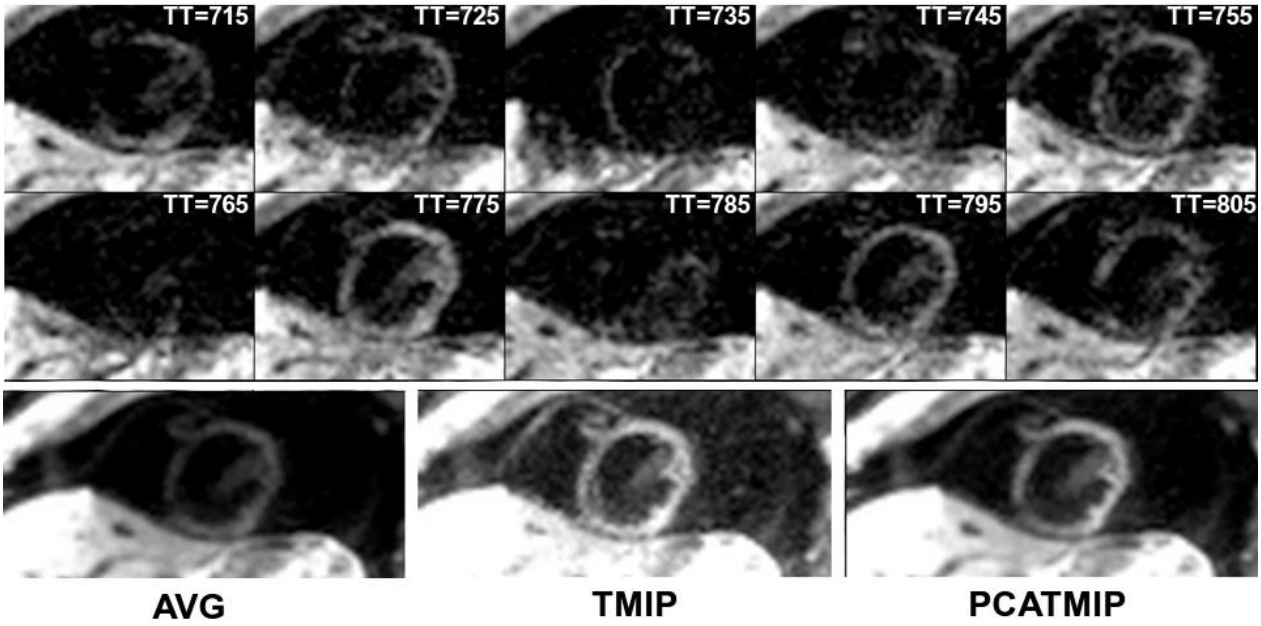

*Figure 64: **TOP**: Free-breathing trace DW-images for b = 100 s/mm² from 10 repetitions acquired at different time points (trigger time TT) within optimal diastolic window in a volunteer. The intensity fluctuation is apparent. **BOTTOM**: Processed DW-images by the three methods: averaging (AVG), direct TMIP and PCATMIP. All 3 image intensities are windowed identically.*

Figure 65 summarizes the increase of signal intensity (SI) attributed to a reduction of motion-induced signal-loss by the TMIP and PCATMIP method when compared to simple averaging (AVG). The TMIP procedure significantly increased myocardial intensity compared to AVG: 46 ± 20 % and 56 ± 30 % for b = 50 and 100 s/mm², resp. $p < 0.001$. The PCATMIP procedure also yielded 21±10% and 23±13% increase at b = 50 and 100 s/mm^2, respectively ($p < 0.001$). Benefits appear to increase for higher b-values ($p < 0.001$). Although TMIP appears to give higher signal intensities than PCATMIP ($p < 0.001$), this is associated with a high level of noise as shown in Figure 66. Figure 66 summarizes the ratio of SNR level of TMIP and PCATMIP relative to averaging (AVG). For non-zero diffusion weighting, TMIP resulted in significantly lower SNR of -34±12% and -31±18% for b = 50 and 100 s/mm², respectively ($p < 0.001$). In contrast, PCATMIP attained +7±13% and +11±17% increase of SNR for b = 50 and 100 s/mm², respectively ($p = 0.003$ and 0.001).

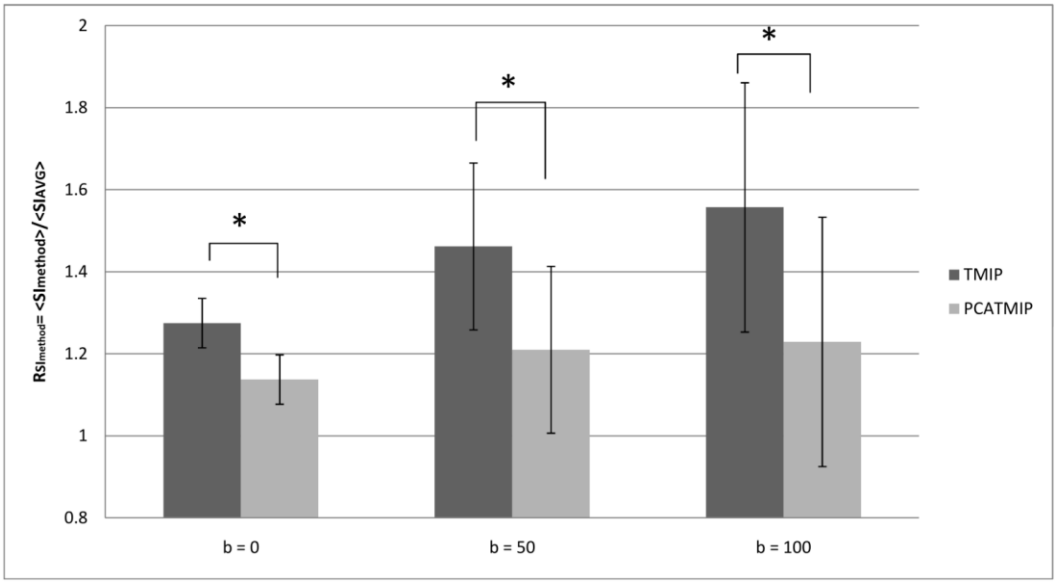

Figure 65: Signal intensity (SI) benefits of TMIP and PCATMIP relative to images averaging (AVG) in volunteers. SI benefits are defined as the ratio of mean DW-images SI values over the LV wall: $R_{SI\,method}(b) = < SI_{method}(b) > / < SI_{AVG}(b) >$. *Data are mean ± sd. *p < 0.05*

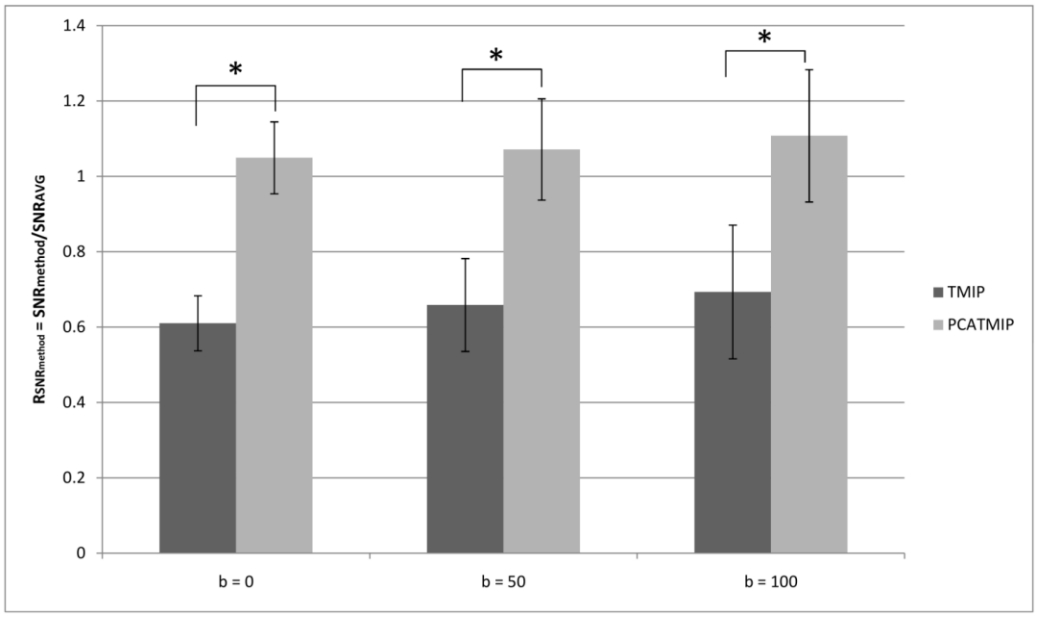

Figure 66: Signal-to-Noise Ratio (SNR) benefits of TMIP and PCATMIP relative to images averaging (AVG) in volunteers. SNR benefits are defined as the ratio of DW-images SNR values: $R_{SNR\,method}(b) = SNR_{method}(b) / SNR_{AVG}(b)$. *Data are mean ± sd. *p < 0.05*

Mean ADC values obtained by the three methods illustrate the impact of reducing motion-related signal loss (Figure 67). With averaging, the signal loss increases with diffusion weighting and results in artificially elevated ADC_m values due to motion. Both TMIP and PCATMIP yielded systematic lower mean ADC values than AVG (17% and 7%, resp.) in myocardium. The TMIP values were approximately 13.7% lower than the PCATMIP values (p=0.047). The *in vivo* results for each method are very similar to simulation results and confirm the potential of PCATMIP of reducing motion-induced DWI signal-loss *in situ*.

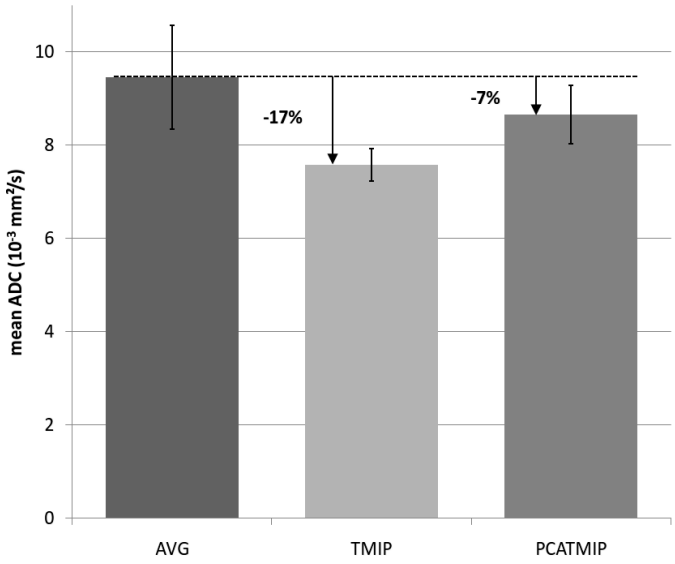

Figure 67: Mean apparent diffusion coefficient (ADCm) values by the three processing methods in the volunteers. On overall, there was no statistically significant difference among methods (p=0.29). But both TMIP and PCATMIP yielded systematic lower values than straight averaging (-17% and -7% respectively). The values from PCATMIP are higher than TMIP. The error bars represent standard deviation in data sets.

Reproducibility study

Method

To assess the reproducibility of the ADC_m results and the effect of free breathing, we repeated in one volunteer two separate free-breathing (FB) scans and a breath-hold (BH) scan for the same slice prescription (10 time-shifted repetitions each scan). The endo- and epicardial borders of the left ventricular (LV) wall were manually drawn and the LV wall was segmented into the AHA standard sectors for regional assessment.

Results

The myocardium mean ADC values from two free-breathing exams (FB) and one breath-hold (BH) exam were very stable (<ADCm(FB1)>=7.4, <ADCm(FB2)>=6.5, <ADCm(BH)>=7.1 mm^2/ms) . These were acquired from the same slice in a single volunteer and all processed with the PCATMIP procedure. Single-factor repeated measures ANOVA showed that there was no significant difference between the results of the two free-breathing scans and the breath-holding scan (p =0.36).

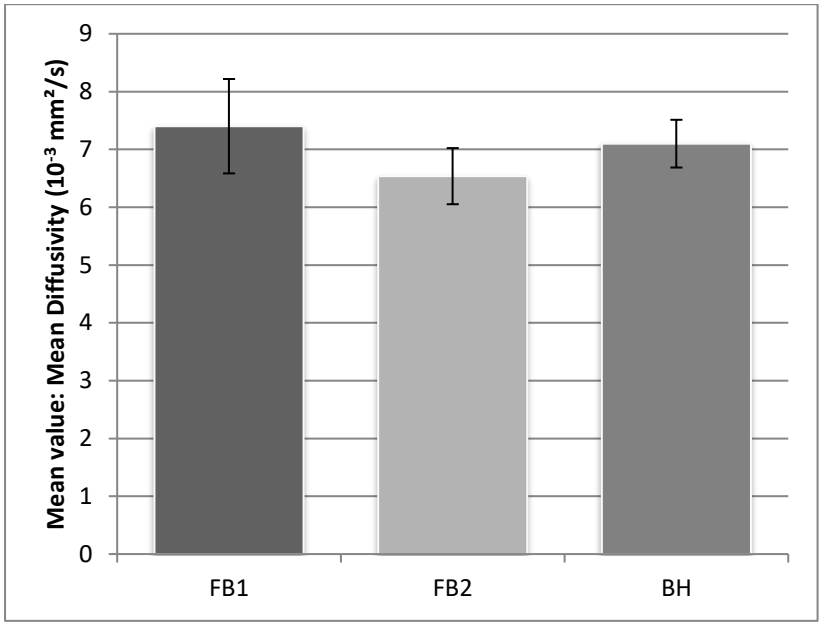

Figure 68: Mean ADC from 3 separate scans of the same slice acquired once with breathholding (BH) and twice under free-breathing (FB1, FB2). There was no statistically significant difference between the results (p = 0.36).

This study involves only one volunteer and should be extended with more acquisitions. However these preliminary results exclude the possibility of a major difference between free breathing and breath holds DWI data. This confirmed the applicability of PCATMIP-DWI while free breathing without biasing its results.

2.8.2.3. Initial patients' results

Enrollment

As a simple application study, 4 patients (2 females/2 males, ages 30-56, HR 57-71 bpm) were admitted for acute ST-elevation myocardial infarction (AMI) with total occlusion of a coronary artery. Percutaneous coronary intervention was performed to obtain a final TIMI-3 flow in the culprit artery

territory. CMR imaging was done 2 days after reperfusion. All subjects gave informed consent to the IRB-approved study protocol.

Method

Additionally to a single-slice DWI acquisition in post-acute MI patients, T2-weighted images were acquired with a short TI inversion-recovery (STIR) turbo-spin-echo dark blood sequence of TE = 47 ms, TR = 2s (~ 2 heartbeats), TI = 170 ms, resolution of 1.5x1.5x8 mm^3 and matrix of 256x208. Early and delayed hyper-enhanced (EHE, DHE) images were acquired at 3 and 10 minutes after 0.2 mmol/kg gadolinium injection (DOTAREM, Guerbet, France) using an inversion-recovery FLASH 3D segmented sequence with TE = 1.36 ms, TR = 456 ms, TI= 400ms, resolution of 1.56 x 1.56 x 5 mm^3 and matrix of 256 x 192.

Results

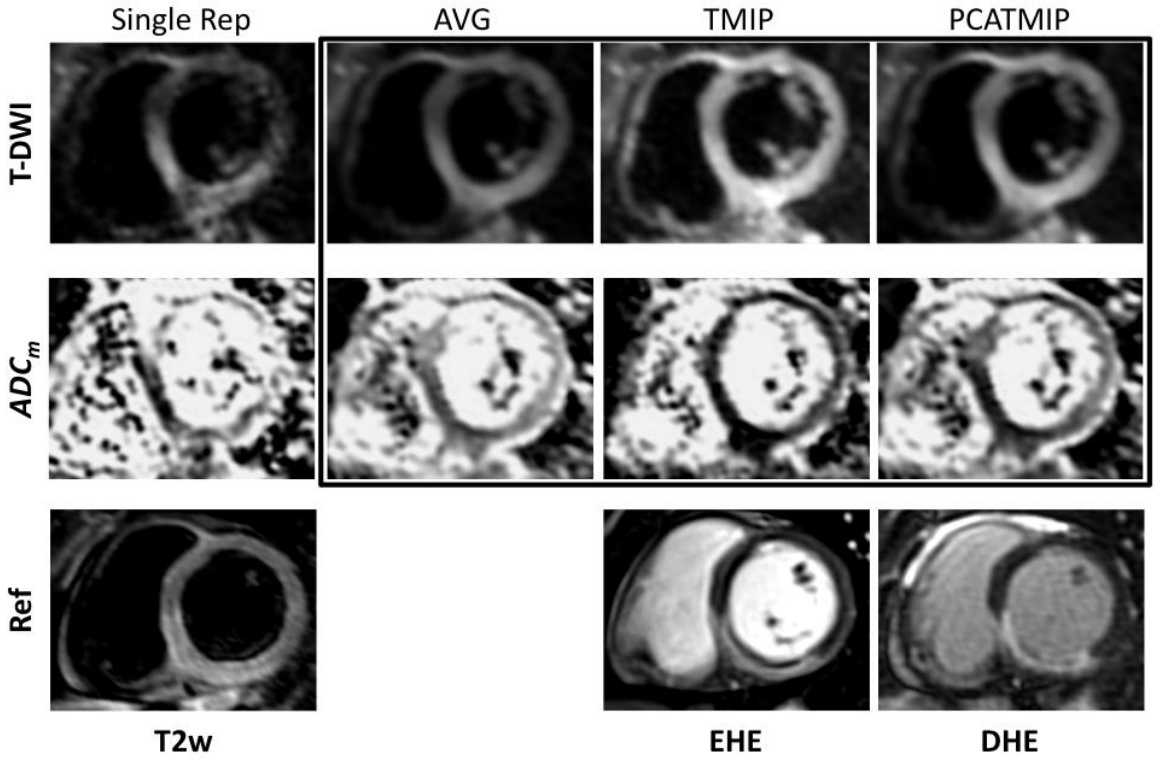

Figure 69: Short-axis images obtained in an inferior acute myocardial infarction patient with micro-vascular obstruction (MVO). TOP Trace diffusion-weighted images (T-DWI) (b = 100 s/mm2) for each processing method; MIDDLE Mean apparent diffusion coefficient (ADCm) maps. BOTTOM T2 weighted image (STIR) and post-gadolinium IR-GRE early (@3 min, EHE) and delayed (@10 min, DHE) images

Figure 69 shows DWI (T-DWI and ADC_m maps), T2w and DHE images from a mid-LV slice in one of the patients. PCATMIP provides a sharper contrast for both T-DWI and mean ADC maps compared to AVG

and TMIP. The quality of a single repetition trace DWI is clearly insufficient. T-DWI intensity is higher with PCATMIP than AVG and less noisy than TMIP only. The anatomical delineation of the myocardium features is easier within PCATMIP T-DWI than with other methods. A clear hyper-intense area can be seen in the PCATMIP Trace-DWI (Figure 69 TOP Right) in the infero-septal and inferior segments that matches the location of the injured myocardium (T2w and DHE).

The mean ADC maps concur with T-DWI observations. While AVG leads to an overestimation of ADC_m values and a less contrasted myocardium, TMIP ADC map suffers artifacts from high noise level. PCATMIP provides a better contrasted ADC map with a lesser noise level. Among all scanned patients, PCATMIP ADC map revealed significantly low ADC values in the culprit artery territory (5.8 ± 0.7 mm^2/ms) and even lower in the micro-vascular obstruction (MVO) area (3.6 ± 0.3 mm^2/ms) than in remote regions (8.3 ± 0.4 mm^2/ms, $p < 0.001$). Low ADC values regions were consistent with the location and extent of the hyper signal intensity within the myocardium in the EHE and DHE images. MVO location observed in early DHE corresponded systematically to the lowest mean ADC values (<5 mm^2/ms).

2.8.2.4. Discussion

We based our approach from the analysis of the physiological motion impact on DWI to reduce most of it. Various approaches (Wen-Yih I. Tseng et al. 2006; Gamper, Boesiger, et Kozerke 2007) have been proposed in the past to develop cardiac diffusion weighted imaging with dedicated MRI sequences that compensate for physiological motion. This work introduces an alternate approach. Our method is flexible in its implementation, supporting free-breathing acquisitions while using state-of-the-art product sequence. Although triggering at peak systole is feasible, acquisition of DWI during diastole is preferable, offering the most durable motion-reduced phase. The time-shifted, multiple repetitions approach combined with temporal-MIP (TMIP) permits to compensate for physiological motion-induced signal loss.

Additionally, ***the basis of TMIP accounts for additional asynchronous contractile motion*** as the minimum signal loss can differ in time for different cardiac segments (e.g. contraction is delayed across the myocardial wall (Buckberg et al. 2006)). However, the limitation of TMIP processing comes primarily from its pixel-wise approach that is highly sensitive to localized noise and motion-induced signal variations. ***TMIP sensitivity is balanced by applying a dedicated post-processing approach*** utilizing

principal component analysis (PCA). The potential of PCATMIP is demonstrated since it reduces the effect of physiological motion (subsequent to registration of bulk motion) to a level where the impact of myocardium infarction on ADC estimation is higher than that of bulk motion (figure 8). Patients' results were more promising than expected revealing very small inter-subjects standard deviations. PCATMIP DWI appears more suited than a conventional method for low b-values DWI dedicated to the human heart with the potential to reliably characterize myocardial tissue.

Recent data(Deux et al. 2010) obtained with state-of-the-art released commercial sequence in humans have demonstrated that DW EPI sequences, when feasible in patients, might be sensitive to increased water content and as such would be an alternative to standard STIR T2-weighted sequences for detecting myocardium high signal areas in patients with recent myocardial infarction. Our experience is that such experiments reproducibility is poor in patients and limits low b-values DWI characterization capabilities. In addition, post-ischemic irreversible (necrosis) or reversible (stunned myocardium) regional dysfunction in the culprit artery vascular bed intrinsically ease DWI by reducing signal loss from motion that may in turn be inappropriately interpreted as regions showing reduced ADC. Combining a state-of-the-art product sequence with dedicated acquisition and image processing strategies, our approach is intended to reduce the bias introduced by physiological motion or regional dysfunction on DWI in the human heart.

The mean ADC values obtained in volunteers reveal the difference between the IVIM effect at low *b* values from molecular diffusion at high *b* values, but the approach could evolve to the full IVIM model(1) with higher *b* values. Our results concur with an earlier study in canine hearts (Callot et al. 2003) and support the idea that the low *b*-values measurements are dominated by microcirculation in capillaries and give much higher ADCs than actual molecular diffusion at high *b* values (Wen-Yih I. Tseng et al. 2006; Gamper, Boesiger, et Kozerke 2007). Molecular diffusion and coronary micro-perfusion are hard to differentiate with low b-values DWI contrary to approaches used in brain imaging (Karonen et al. 1999; KO Lovblad et al. 1998; G. Schlaug et al. 1999). Unfortunately, there exists no gold standard for evaluating the information obtained through DWI in the *in-vivo* heart. But Callot et al.(Callot et al. 2003) showed structural information from low b-values IVIM imaging in the heart matched the spatial information provided by *ex-vivo* DWI. For all these reasons, cardiac low b-values IVIM imaging holds as much interest in the diagnosis of cardiac diseases as pure DWI does for brain lesion. Accessing the velocity of micro flows or their direction might help in understanding patho-physiological processes.

2.8.2.5. Limitations

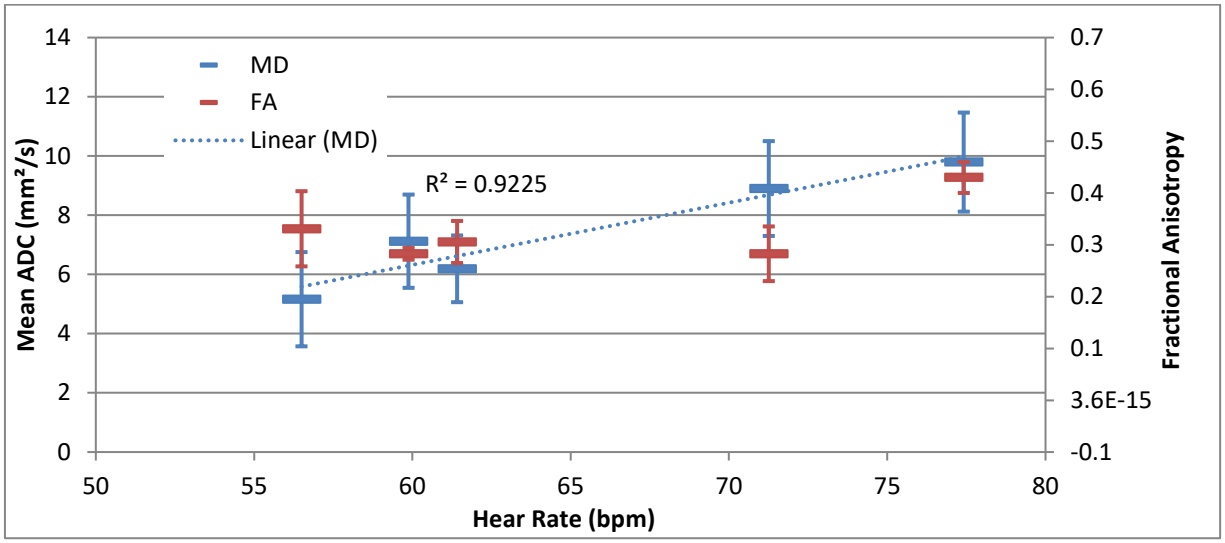

Figure 70: mean ADC (MD) and fractional anisotropy (FA) values plotted against volunteers' heart rate. A linear regression of mADC values was performe to confront the trend of mADC values with a linear dependency to heart rate.

Our PCATMIP method appears to partially remove motion-induced DWI signal-loss. However some motion seems to remain as the study of mean ADC values against volunteers' heart rate suggests (Figure 70). Mean ADC values increase linearly with the subject heart rate.

The methodology we present here is applicable to any sequence kernel. Single-shot double-refocus diffusion weighted sequence used in this study might not be optimal for low b studies but has the advantage of minimal eddy current effects. Also due to a limitation of the parallel imaging reconstruction software on the scanner, only the absolute image intensity was available without any phase information. This leads to the relatively high eigenvalue threshold *Et* value (chapter 2.8.1.1.). In comparison, additional simulations showed that with magnitude and phase data of the same noise level, the optimal threshold will be 10 times lower. This means that we can tolerate higher noise levels with complex data, and obtain better SNR in the processed results given the same input SNR. Therefore, the PCATMIP approach would benefit substantially from accessing phase data.

Finally diffusion weighting *b* parameter appears limited to low values (up to 150 s/mm²) with chosen bipolar gradients sequence. Our choice of restricting b values to 100 s/mm² has justification from our concern of proposing a method to image cardiac IVIM that can be reproduced even in the presence of large physiological motion, as for severely ill patients. However, dedicated MRI sequences for cardiac low b-values DWI, such as with k-space acquisition schemes other than EPI, might be explored towards accessing higher b values. But this could increase acquisition sensitivity to other MRI

parameters such as magnetic field inhomogeneities. Indeed, the increased distortion of cardiac MR imaging might results in additional diffusion estimation bias. Also, tissues interfaces and flows highly deform local magnetic field, especially when myocardium wall is very thin. Furthermore, DWI, like any other phase-sensitive contrast technique, is highly sensitive to motion, adding potential distortions. Therefore, distortion correction should be improved by the systematic volume shimming that was performed during the acquisitions. Finally, currently proposed single-shot DWI EPI sequence with systematic shimming has the advantage of being robust and stable between different studies.

3. Conclusions and Outlooks

3.1. Conclusions and discussions

Through this work, a better understanding of cardiac low b-values DWI is detailed. We first examined the different sources of possible signal intensity loss for cardiac DWI: physiological motion and physiological flows. This initial study confirmed the difficulty to separate motion, perfusion and diffusion with DWI. Low b-values cardiac DWI should more appropriately be interpreted as intra-voxel incoherent motion (IVIM) imaging. Our purpose being the maximum reduction of motion-related information mixed in retrieved IVIM information.

This work started with separate analysis of the impact of some critical acquisition parameters: the acquired slice thickness proves to impact both DWI signal-to-noise ratio and signal intensity through the amount of motion-induced signal loss, especially for short-axis slices. A compromise was found between SNR and signal intensity. Another point was to propose a dummy scan prior to acquisition series in order to reach a signal recovery steady-state.

We then moved to the detailed study of cardiac motion influence on low b-values DWI. Through a simulation from volunteer's displacement encoded data, we were able to define a time-window of most durable low intensity loss in diastole. This time-window, optimal for DWI triggering, was confirmed with experimental DWI results. However this study provided also the observation of remaining motion-induced intensity fluctuation both spatially and in time.

This conclusion lead us to propose an innovative acquisition strategy: low b-values DWI repetitions were shifted within the optimal time-window for capturing these intensity fluctuations. Eventually the motion-induced signal-loss was minimized, i.e. diffusion weighted intensity was maximized, through the temporal maximum intensity projection (TMIP). The TMIP approach proves to significantly reduce motion-induced signal loss as well as ease acquisition by simplifying the precise definition of the optimal time-window.

The TMIP approach was combined with several MR sequence designs. We first developed and investigated a spin-echo EPI with a centered-out k-space readout scheme. While this sequence proved to provide the lowest TE possible, it was severely limited by off-resonance artifacts in the form of aliasing. Phase-field-of-view was too short to allow proper application. A second design was developed as a

response to these limitations. A diffusion-preparation was combined with balanced-SSFP readout. The sequence was very robust to spatial distortions, but proved too affected by off-resonance b-SSFP artifacts: dark bands were covering the myocardium as soon as the diffusion encoding was on. Finally we opted for the optimization of the state-of-the art sequence available on our scanner. The double spin-echo EPI sequence minimizes eddy-currents impact on EPI, has a built-in EPI spatial distortions correction, but at the cost of longer TE. Thus choosing this sequence was a limitation in the range of *b* values accessible. However TMIP results obtained with this sequence enabled further study towards the potential application of low b-values cardiac DWI.

Then through the understanding of TMIP limitations, we worked at separating noise spikes from motion-induced smooth intensity variations. The development of a principal component analysis (PCA) based method increased significantly image quality (SNR) without altering neither anatomical features nor motion-induced intensity fluctuations. The method parameters were optimized through numerical simulations. PCA benefits were quantified on both simulated data and experimental data.

The combined PCATMIP-DWI approach stands as our solution for both reducing motion-induced signal loss and increase final image quality. PCATMIP benefits were quantified through a simulation using experimental motion data before being confirmed experimentally in a sample of volunteers. The experimental set-up proves also flexible as the acquisitions were performed free-breathing. The initial limitations we had stated to allow clinical applicability were fulfilled.

Consequently we were able to apply briefly the PCATMIP-DWI approach in a small sample of acute myocardial infarction patients. The reproducibility of the measurement was surprisingly even higher than in volunteers. The observed contrast matches the extent and position of the injury observed with other CMR methods, encouraging further investigation of the technique towards potential clinical application for cardiac imaging.

3.2. Perspectives

This thesis project has enabled my work to range from theoretical study of cardiac motion to sequence design, then image processing to end with *in vivo* applications. However this work is far from complete. While the PCATMIP-DWI stands as a mature approach for cardiac DWI, it can be combined with any DWI sequence that would improve images at the stage of acquisition. A dedicated MR sequence for cardiac low b-values DWI could provide: shorter echo times (TE), increasing either image intensity or

accessing higher b values at equivalent TE; alternative k-space readout scheme to reduce spatial distortions and/or off-resonance artifacts; segmented k-space readout to make use of multiple repetitions, towards either reducing TE and/or providing built-in image registration. Certainly a major perspective to this work is to provide a more appropriate sequence design to combine with PCATMIP approach.

One of the most interesting features is the capacity to access higher b values (>200 s/mm²). The scale of motion retrieved would get closer to diffusion than perfusion. Consequently tissue characterization would be more accurate and the contrast provided would reach interesting information similar to DWI as in the brain. Moreover the combination of low and high b-values could open cardiac DWI to the complete IVIM imaging model. That is the differentiation between blood perfusion and water molecules diffusion can be done with the use of both low and high b-values. Two very different information both critical to the understanding of cardiac diseases and their diagnosis would be accessible within the same technique.

This differentiation of diffusion and perfusion could also be investigated through the exploitation of the two optimal time-windows available within the cardiac cycle. As our feasibility shows, acquisitions could be triggered at either peak systole or in mid-diastole, with a preference for diastole to obtain reproducible results. However the systolic time-window presents the interesting feature of reduced perfusion compared to the diastolic window. This contrast might add another parameter in the application of IVIM cardiac imaging and develop further the interpretation of results depending on the chosen trigger time.

Finally even without the need of a new sequence or the access to higher b-values, the current state of low b-values DWI presents a significant contrast in the case of myocardium pathology. The study of low b-values DWI diagnosis potential certainly raises interest and hopefully will lead to experimental studies of selected cardiac diseases. An experimental model of a selected cardiac disease that would confront the results from low b-values DWI to the definition of the pathology (i.e. gold standards) could accurately define the clinical capacity of low b-values DWI. While technical developments are interesting perspectives of this work, experimental applications of the current technique stand as even more promising as it encourages future studies, uses and improvements by the cardiac MRI community.

References

Anon.sans date. WHO | The top 10 causes of death. http://www.who.int/mediacentre/factsheets/fs310/en/index.html.

Absil, Julie. 2006. Contribution to the developments of rapid acquisition schemes in Magnetic Resonance Imaging. Université libre de Bruxelles. http://theses.ulb.ac.be/ETD-db/collection/available/ULBetd-08232007-180228/.

Aletras, Anthony H., Shujun Ding, Robert S. Balaban, et Han Wen. 1999. DENSE: Displacement Encoding with Stimulated Echoes in Cardiac Functional MRI. *Journal of Magnetic Resonance* 137, n°. 1 (Mars): 247-252. doi:10.1006/jmre.1998.1676.

Alexander, A. L., J. S. Tsuruda, et D. L. Parker. 1997. Elimination of eddy current artifacts in diffusion-weighted echo-planar images: The use of bipolar gradients. *Magnetic Resonance in Medicine* 38, n°. 6: 1016-1021.

Allouche, Cyril, S. Makam, Nicholas Ayache, et Hervé Delingette. 2001. A New Kinetic Modeling Scheme for the Human Left Ventricle Wall Motion with MR-Tagging Imaging. Dans *Functional Imaging and Modeling of the Heart*, 61-68. http://dx.doi.org/10.1007/3-540-45572-8_9.

Anderson, R. H., S. Y. Ho, D. Sanchez-Quintana, K. Redmann, et P. P. Lunkenheimer. 2006. Heuristic problems in defining the three-dimensional arrangement of the ventricular myocytes. Article. Juin. http://eprints.ucl.ac.uk/74049/.

Basser, P J, J Mattiello, et D LeBihan. 1994. MR diffusion tensor spectroscopy and imaging. *Biophysical Journal* 66, n°. 1 (Janvier): 259-267. doi:10.1016/S0006-3495(94)80775-1.

Basser, Peter J, et Derek K Jones. 2002. Diffusion-tensor MRI: theory, experimental design and data analysis - a technical review. *NMR in Biomedicine* 15, n°. 7 (Décembre): 456-467. doi:10.1002/nbm.783.

Bassingthwaighte, James B., Tada Yipintsoi, et Rodney B. Harvey. 1974. Microvasculature of the dog left ventricular myocardium. *Microvascular Research* 7, n°. 2 (Mars): 229-249. doi:10.1016/0026-2862(74)90008-9.

Benveniste, H, L W Hedlund, et G A Johnson. 1992. Mechanism of detection of acute cerebral ischemia in rats by diffusion-weighted magnetic resonance microscopy. *Stroke; a Journal of Cerebral Circulation* 23, n°. 5 (Mai): 746-754.

Bernstein, Matt A., Kevin F. King, et Xiaohong Joe Zhou. 2004. *Handbook of MRI Pulse Sequences*. 1er éd. Academic Press, Septembre 21.

Bloch, F. 1946. Nuclear Induction. *Physical Review* 70, n°. 7 (Octobre 1): 460. doi:10.1103/PhysRev.70.460.

Bottomley, Paul A., et Robert G. Weiss. 1998. Human cardiac spectroscopy. *Magma: Magnetic Resonance Materials in Physics, Biology, and Medicine* 6, n°. 2 (9): 157-160. doi:10.1007/BF02660945.

Buckberg, Gerald D., Manuel Castella, Morteza Gharib, et Saleh Saleh. 2006. Active myocyte shortening during the 'isovolumetric relaxation' phase of diastole is responsible for ventricular suction; 'systolic ventricular filling'. *Eur J Cardiothorac Surg* 29, n°. 1 (Avril 1): S98-106. doi:10.1016/j.ejcts.2006.02.043.

Callot, Virginie, Eric Bennett, Ulrich K.M. Decking, Robert S. Balaban, et Han Wen. 2003. In vivo study of microcirculation in canine myocardium using the IVIM method. *Magnetic Resonance in Medicine* 50, n°. 3: 531-540. doi:10.1002/mrm.10568.

Carr, H. Y. 1958. Steady-State Free Precession in Nuclear Magnetic Resonance. *Physical Review*

112, n°. 5 (Décembre 1): 1693. doi:10.1103/PhysRev.112.1693.

Chefd'hotel, C., D. Tschumperlé, R. Deriche, et O. Faugeras. 2002. Constrained Flows of Matrix-Valued Functions: Application to Diffusion Tensor Regularization. Dans *Computer Vision — ECCV 2002*, 251-265. http://dx.doi.org/10.1007/3-540-47969-4_17.

Chefd'Hotel, C., G. Hermosillo, et O. Faugeras. 2001. A variational approach to multi-modal image matching. Dans *Variational and Level Set Methods in Computer Vision, 2001. Proceedings. IEEE Workshop on*, 21-28. doi:10.1109/VLSM.2001.938877.

Chefd'hotel, C., D. Tschumperlé, R. Deriche, et O. Faugeras. 2004. Regularizing Flows for Constrained Matrix-Valued Images. *Journal of Mathematical Imaging and Vision* 20, n°. 1 (1): 147-162. doi:10.1023/B:JMIV.0000011324.14508.fb.

Chun, Terry, Aziz M. Uluğ, et Peter C. M. van Zijl. 1998. Single-shot diffusion-weighted trace imaging on a clinical scanner. *Magnetic Resonance in Medicine* 40, n°. 4 (10): 622-628. doi:10.1002/mrm.1910400415.

Das, D K, R M Engelman, J A Rousou, et R H Breyer. 1987. Aerobic vs anaerobic metabolism during ischemia in heart muscle. *Annales Chirurgiae Et Gynaecologiae* 76, n°. 1: 68-76.

DeLaPaz, R L. 1994. Echo-planar imaging. *Radiographics* 14, n°. 5: 1045 -1058.

Deux, Jean-François, Mezri Maatouk, Alexandre Vignaud, Alain Luciani, Grégory Lenczner, Julie Mayer, Pascal Lim, Jean-Luc Dubois-Randé, Hicham Kobeiter, et Alain Rahmouni. 2010. Diffusion-weighted echo planar imaging in patients with recent myocardial infarction. *European Radiology* (8). doi:10.1007/s00330-010-1912-6. http://www.springerlink.com/content/c214g5552h8h745l/.

Dou, Jiangang, Timothy G Reese, Wen-Yih I Tseng, et Van J Wedeen. 2002. Cardiac diffusion MRI without motion effects. *Magnetic Resonance in Medicine: Official Journal of the Society of Magnetic Resonance in Medicine / Society of Magnetic Resonance in Medicine* 48, n°. 1 (Juillet): 105-114. doi:10.1002/mrm.10188.

DOUGLAS, JOHN E., et JOSEPH C. GREENFIELD. 1970. Epicardial Coronary Artery Compliance in the Dog. *Circ Res* 27, n°. 6 (Décembre 1): 921-929.

Egan, Jonathan R, Tanya L Butler, Carol G Au, Yee Mun Tan, Kathryn N North, et David S Winlaw. 2006. Myocardial water handling and the role of aquaporins. *Biochimica Et Biophysica Acta* 1758, n°. 8 (Août): 1043-1052. doi:10.1016/j.bbamem.2006.05.021.

Einstein, A. 1905. Über die von der molekularkinetischen Theorie der Wärme geforderte Bewegung von in ruhenden Flüssigkeiten suspendierten Teilchen. *Annalen der Physik* 322, n°. 8: 549-560. doi:10.1002/andp.19053220806.

Einstein, Albert, et Reinhold Fürth. 1956. *Investigations on the theory of the Brownian movement*. Courier Dover Publications.

Elliott, Andrew M., Matt A. Bernstein, Heidi A. Ward, John Lane, et Robert J. Witte. 2007. Nonlinear averaging reconstruction method for phase-cycle SSFP. *Magnetic Resonance Imaging* 25, n°. 3 (Avril): 359-364. doi:10.1016/j.mri.2006.09.013.

Fischer, Stefan E., Matthias Stuber, Markus B. Scheidegger, et Peter Boesiger. 1995. Limitations of stimulated echo acquisition mode (steam) techniques in cardiac applications. *Magnetic Resonance in Medicine* 34, n°. 1: 80-91. doi:10.1002/mrm.1910340113.

Freeman, GL, MM LeWinter, RL Engler, et JW Covell. 1985. Relationship between myocardial fiber direction and segment shortening in the midwall of the canine left ventricle. *Circ Res* 56, n°. 1 (Janvier 1): 31-39.

Friedrich, Matthias G. 2010. Myocardial edema[mdash]a new clinical entity? *Nat Rev Cardiol* 7, n°. 5 (Mai): 292-296. doi:10.1038/nrcardio.2010.28.

Gamper, Urs, Peter Boesiger, et Sebastian Kozerke. 2007. Diffusion imaging of the in vivo heart

using spin echoes-considerations on bulk motion sensitivity. *Magnetic Resonance in Medicine* 57, n°. 2: 331-337. doi:10.1002/mrm.21127.

Garrido, L, V J Wedeen, K K Kwong, U M Spencer, et H L Kantor. 1994. Anisotropy of water diffusion in the myocardium of the rat. *Circulation Research* 74, n°. 5 (Mai): 789-793.

Griswold, Mark A, Peter M Jakob, Robin M Heidemann, Mathias Nittka, Vladimir Jellus, Jianmin Wang, Berthold Kiefer, et Axel Haase. 2002. Generalized autocalibrating partially parallel acquisitions (GRAPPA). *Magnetic Resonance in Medicine: Official Journal of the Society of Magnetic Resonance in Medicine / Society of Magnetic Resonance in Medicine* 47, n°. 6 (Juin): 1202-1210. doi:10.1002/mrm.10171.

Haacke, E. Mark, Robert W. Brown, Michael R. Thompson, et Ramesh Venkatesan. 1999. *Magnetic Resonance Imaging: Physical Principles and Sequence Design*. 1er éd. Wiley-Liss, Juin 15.

Hakim, A M. 1987. The cerebral ischemic penumbra. *The Canadian Journal of Neurological Sciences. Le Journal Canadien Des Sciences Neurologiques* 14, n°. 4 (Novembre): 557-559.

Hoffman, Julien I. E., et William M. Chilian. 2000. Brief commentary on coronary wave-intensity analysis. *J Appl Physiol* 89, n°. 4 (Octobre 1): 1633-1635.

Jeong, Eun-Kee, Seong-Eun Kim, Eugene G. Kholmovski, et Dennis L. Parker. 2006. High-resolution DTI of a localized volume using 3D single-shot diffusion-weighted STimulated echo-planar imaging (3D ss-DWSTEPI). *Magnetic Resonance in Medicine* 56, n°. 6: 1173-1181. doi:10.1002/mrm.21088.

Jezzard, P, et R S Balaban. 1995. Correction for geometric distortion in echo planar images from B0 field variations. *Magnetic Resonance in Medicine: Official Journal of the Society of Magnetic Resonance in Medicine / Society of Magnetic Resonance in Medicine* 34, n°. 1 (Juillet): 65-73.

Judd, Robert M., Scott B. Reeder, et Karen May-Newman. 1999. Effects of water exchange on the measurement of myocardial perfusion using paramagnetic contrast agents. *Magnetic Resonance in Medicine* 41, n°. 2: 334-342.

Karonen, Jari O., Ritva L. Vanninen, Yawu Liu, Leif Ostergaard, Jyrki T. Kuikka, Juho Nuutinen, Esko J. Vanninen, et al. 1999. Combined Diffusion and Perfusion MRI With Correlation to Single-Photon Emission CT in Acute Ischemic Stroke : Ischemic Penumbra Predicts Infarct Growth. *Stroke* 30, n°. 8 (Août 1): 1583-1590.

Kastler, Bruno, Daniel Vetter, ZoltÂàn Patay, et Philippe Germain. 2006. *Comprendre l'IRM : Manuel d'auto-apprentissage*. 6 éd. Masson, Novembre 9.

Katz, Arnold M. 2005. *Physiology of the Heart*. Fourth. Lippincott Williams & Wilkins, Novembre 3.

Kellman, Peter, Christophe Chefd'hotel, Christine H. Lorenz, Christine Mancini, Andrew E. Arai, et Elliot R. McVeigh. 2008. Fully automatic, retrospective enhancement of real-time acquired cardiac cine MR images using image-based navigators and respiratory motion-corrected averaging. *Magnetic Resonance in Medicine* 59, n°. 4: 771-778. doi:10.1002/mrm.21509.

Klabunde, Richard E. 2004. *Cardiovascular Physiology Concepts*. Lippincott Williams & Wilkins, Juillet 1.

Le Bihan, D, E Breton, D Lallemand, P Grenier, E Cabanis, et M Laval-Jeantet. 1986. MR imaging of intravoxel incoherent motions: application to diffusion and perfusion in neurologic disorders. *Radiology* 161, n°. 2 (Novembre): 401-407.

Le Bihan, Denis. 2008. Intravoxel Incoherent Motion Perfusion MR Imaging: A Wake-Up Call1.

Radiology 249, n°. 3: 748-752. doi:10.1148/radiol.2493081301.

Le Roux, Patrick. 2003. Simplified model and stabilization of SSFP sequences. *Journal of Magnetic Resonance* 163, n°. 1 (Juillet): 23-37. doi:10.1016/S1090-7807(03)00115-0.

Lovblad, KO, HJ Laubach, AE Baird, F Curtin, G Schlaug, RR Edelman, et S Warach. 1998. Clinical experience with diffusion-weighted MR in patients with acute stroke. *AJNR Am J Neuroradiol* 19, n°. 6 (Juin 1): 1061-1066.

Lustig, Michael, David Donoho, et John M Pauly. 2007. Sparse MRI: The application of compressed sensing for rapid MR imaging. *Magnetic Resonance in Medicine: Official Journal of the Society of Magnetic Resonance in Medicine / Society of Magnetic Resonance in Medicine* 58, n°. 6 (Décembre): 1182-1195. doi:10.1002/mrm.21391.

McCommis, Kyle S, Xiang He, Dana R Abendschein, Pradeep M Gupte, Robert J Gropler, et Jie Zheng. 2010. Cardiac 17O MRI: toward direct quantification of myocardial oxygen consumption. *Magnetic Resonance in Medicine: Official Journal of the Society of Magnetic Resonance in Medicine / Society of Magnetic Resonance in Medicine* 63, n°. 6 (Juin): 1442-1447. doi:10.1002/mrm.22382.

Mehlhorn, Uwe, Hans J. Geissler, Glen A. Laine, et Steven J. Allen. 2001. Myocardial fluid balance. *Eur J Cardiothorac Surg* 20, n°. 6 (Décembre 1): 1220-1230.

Prinzen, F W, T Arts, T T Prinzen, et R S Reneman. 1985. Comments on "Relationship between myocardial fiber direction and segment shortening in the midwall of the canine left ventricle". *Circulation Research* 57, n°. 6 (Décembre): 909-911.

Raichle, M E. 1983. The pathophysiology of brain ischemia. *Annals of Neurology* 13, n°. 1 (Janvier): 2-10. doi:10.1002/ana.410130103.

Rajeshkannan, R, S Moorthy, Kp Sreekumar, R Rupa, et Nk Prabhu. 2006. Clinical applications of diffusion weighted MR imaging: A review. *Indian Journal of Radiology and Imaging* 16, n°. 4: 705. doi:10.4103/0971-3026.32328.

Reese, T.G., O. Heid, R.M. Weisskoff, et V.J. Wedeen. 2003. Reduction of eddy-current-induced distortion in diffusion MRI using a twice-refocused spin echo. *Magnetic Resonance in Medicine* 49, n°. 1: 177-182. doi:10.1002/mrm.10308.

Rossi, G. 2007. Numerical simulation of perfusion in the beating heart. Milano, IT: Politecnico di Milano, Décembre 20.

Schlaug, G., A. Benfield, A. E. Baird, B. Siewert, K. O. Lovblad, R. A. Parker, R. R. Edelman, et S. Warach. 1999. The ischemic penumbra: Operationally defined by diffusion and perfusion MRI. *Neurology* 53, n°. 7 (Octobre 22): 1528.

Sevick, R J, F Kanda, J Mintorovitch, A I Arieff, J Kucharczyk, J S Tsuruda, D Norman, et M E Moseley. 1992. Cytotoxic brain edema: assessment with diffusion-weighted MR imaging. *Radiology* 185, n°. 3 (Décembre): 687-690.

Siebes, Maria, Christina Kolyva, Bart-Jan Verhoeff, Jan J. Piek, et Jos A. Spaan. 2009. Potential and limitations of wave intensity analysis in coronary arteries. *Medical & Biological Engineering & Computing* 47, n°. 2 (2): 233-239. doi:10.1007/s11517-009-0448-x.

Snyder, C.J., L. DelaBarre, G.J. Metzger, P.-F. van de Moortele, C. Akgun, K. Ugurbil, et J.T. Vaughan. 2009. Initial results of cardiac imaging at 7 tesla. *Magnetic Resonance in Medicine* 61, n°. 3: 517-524. doi:10.1002/mrm.21895.

Sparrow, Patrick, Daniel R. Messroghli, Scott Reid, John P. Ridgway, Gavin Bainbridge, et Mohan U. Sivananthan. 2006. Myocardial T1 Mapping for Detection of Left Ventricular Myocardial Fibrosis in Chronic Aortic Regurgitation: Pilot Study. *Am. J. Roentgenol.* 187, n°. 6 (Décembre 1): W630-635. doi:10.2214/AJR.05.1264.

Stejskal, E. O., et J. E. Tanner. 1965. Spin Diffusion Measurements: Spin Echoes in the Presence

of a Time-Dependent Field Gradient. *The Journal of Chemical Physics* 42, n°. 1 (Janvier 1): 288-292.

Stöcker, Tony, Joachim Kaffanke, et N Jon Shah. 2009. Whole-brain single-shot STEAM DTI at 4 Tesla utilizing transverse coherences for enhanced SNR. *Magnetic Resonance in Medicine: Official Journal of the Society of Magnetic Resonance in Medicine / Society of Magnetic Resonance in Medicine* 61, n°. 2 (Février): 372-380. doi:10.1002/mrm.21853.

Stralka, John P, et Paul A Bottomley. 2007. A Prototype RF Dosimeter for Independent Measurement of the Average Specific Absorption Rate (SAR) During MRI. *Journal of magnetic resonance imaging : JMRI* 26, n°. 5 (Novembre): 1296-1302. doi:10.1002/jmri.21141.

Streeter, Daniel D., Ramesh N. Vaishnav, Dali J. Patel, Henry M. Spotnitz, John Ross, et Edmund H. Sonnenblick. 1970. Stress Distribution in the Canine Left Ventricle during Diastole and Systole. *Biophysical Journal* 10, n°. 4 (Avril): 345-363.

Topol, Eric J., Robert M. Califf, Jeffrey Isner, Eric N. Prystowsky, Judith Swain, James Thomas, Paul Thompson, et James B. Young. 2002. *Textbook of Cardiovascular Medicine*. Second. Lippincott Williams & Wilkins, Février 15.

Torrey, H. C. 1956. Bloch Equations with Diffusion Terms. *Physical Review* 104, n°. 3 (Novembre 1): 563. doi:10.1103/PhysRev.104.563.

Toussaint, Nicolas, Christian T. Stoeck, Sebastian Kozerke, Maxime Sermesant, et Philip G. Batchelor. 2010. In-vivo Human 3D Cardiac Fibre Architecture: Reconstruction Using Curvilinear Interpolation of Diffusion Tensor Images. Dans *Proc. Medical Image Computing and Computer Assisted Intervention (MICCAI'10)*. LNCS. Beijing, China: Springer, Septembre.

Toussaint, Nicolas, Christian T. Stoeck, Maxime Sermesant, Sebastian Kozerke, et Philip G. Batchelor. 2010. Three-dimensional Prolate Spheroidal Extrapolation for Sparse DTI of the In-vivo Heart. Dans *Book of Abstracts, International Society in Magnetic Resonance in Medicine (ISMRM'10)*. Stockholm, Juin 2.

Tseng, W Y, T G Reese, R M Weisskoff, T J Brady, et V J Wedeen. 2000. Myocardial fiber shortening in humans: initial results of MR imaging. *Radiology* 216, n°. 1 (Juillet): 128-139.

Tseng, W Y, T G Reese, R M Weisskoff, et V J Wedeen. 1999. Cardiac diffusion tensor MRI in vivo without strain correction. *Magnetic Resonance in Medicine: Official Journal of the Society of Magnetic Resonance in Medicine / Society of Magnetic Resonance in Medicine* 42, n°. 2 (Août): 393-403.

Tseng, Wen-Yih I., Jiangang Dou, Timothy G. Reese, et Van J. Wedeen. 2006. Imaging myocardial fiber disarray and intramural strain hypokinesis in hypertrophic cardiomyopathy with MRI. *Journal of Magnetic Resonance Imaging* 23, n°. 1: 1-8. doi:10.1002/jmri.20473.

Wieneke, Heinrich, Michael Haude, Junbo Ge, Christoph Altmann, Sigrid Kaiser, Dietrich Baumgart, Clemens von Birgelen, Dirk Welge, et Raimund Erbel. 2000. Corrected coronary flow velocity reserve: a new concept for assessing coronary perfusion. *J Am Coll Cardiol* 35, n°. 7 (Juin 1): 1713-1720.

Wu, Ming-Ting, Mao-Yuan M. Su, Yi-Luan Huang, Kuan-Rau Chiou, Pinchen Yang, Huay-Ben Pan, Timothy G. Reese, Van J. Wedeen, et Wen-Yih I. Tseng. 2009. Sequential Changes of Myocardial Microstructure in Patients Postmyocardial Infarction by Diffusion-Tensor Cardiac MR: Correlation With Left Ventricular Structure and Function. *Circ Cardiovasc Imaging* 2, n°. 1 (Janvier 1): 32-40. doi:10.1161/CIRCIMAGING.108.778902.

Wu, Ming-Ting, Wen-Yih I. Tseng, Mao-Yuan M. Su, Chun-Peng Liu, Kuan-Rau Chiou, Van J. Wedeen, Timothy G. Reese, et Chien-Fang Yang. 2006. Diffusion Tensor Magnetic Resonance Imaging Mapping the Fiber Architecture Remodeling in Human Myocardium After Infarction. Correlation With Viability and Wall Motion. *Circulation* (Août 28): CIRCULATIONAHA.105.545863. doi:10.1161/CIRCULATIONAHA.105.545863.

Zeeman, P. 1897. The Effect of Magnetisation on the Nature of Light Emitted by a Substance. *Nature* 55, n°. 1424 (2): 347-347. doi:10.1038/055347a0.